COMPARISON OF TECHNIQUES TO MEASURE THE LOW WAVENUMBER WALL PRESSURE SPECTRUM OF A TURBULENT BOUNDARY LAYER

by

KYLE F. MARTINI
//

B.S.M.E., Lehigh University
(1973)

M.S.M.E., Northeastern University
(1978)

Submitted to the Department of
Mechanical Engineering
in Partial Fulfillment of the
Requirements for the
Degree of

MECHANICAL ENGINEER

at the

MASSACHUSETTS INSTITUTE OF TECHNOLOGY

May 1984

c Massachusetts Institute of Technology 1984

Signature of Author_____Signature redacted_____
Department of Mechanical Engineering
May 11, 1984

Signature redacted

Certified by_____
Thesis Supervisor

Signature redacted

Accepted by_____
Chairman, Mechanical Engineering Department Committee

COMPARISON OF TECHNIQUES TO MEASURE THE LOW
WAVENUMBER WALL PRESSURE SPECTRUM OF A
TURBULENT BOUNDARY LAYER

by

Kyle F. Martini

Submitted to the Department of Mechanical Engineering
on May 11, 1984 in partial fulfillment of the
requirements for the Engineer's Degree in
Mechanical Engineering

ABSTRACT

The agreement between low wavenumber measurements of
the turbulent wall pressure spectrum by various investigators
has not been too good. Different techniques have been used
in different facilities and have yielded data in different
nondimensional frequency and wavenumber ranges. The current
measurement program has utilized the wavenumber filtering
techniques used by three primary investigators, the Martin
Plate, the Jameson Plate, and the Farabee and Geib 6-element
microphone array in the same facility. The agreement between
the three techniques in the M.I.T. facility is generally
good, however, there was significant scatter in the data for
each technique. The cause of the scatter is believed to be
due to the variation of each filter's wavenumber response,
away from the main acceptance lobe, where the filter is
responding to acoustic and convective contamination and also
the variation of the contamination with flow speed. In
addition, the difference of results between facilities has
been reduced by displaying the data in a non-dimensional form
that does not include the effect of boundary layer thickness.

Thesis Supervisor: Prof. Patrick Leehey

            Title: Professor of Mechanical & Ocean
                    Engineering

ACKNOWLEDGEMENTS

There are many individuals who have made significant contributions to this thesis effort and deserve a special word of appreciation. I would like to thank Professor Patrick Leehey for his guidance and support during the course of this work.

I would also like to thank Professor Stephen Crandall, Dr. Mark Moeller, Dr. Charles Gedney and Dr. Nathan Martin for their helpful discussions during this research program, and Margaret Cahoon for efficient typing of this thesis.

Mostly, I would like to thank my wife, Joyce, for being supportive and understanding during this undertaking.

TABLE OF CONTENTS

LIST OF TABLES

LIST OF FIGURES

LIST OF SYMBOLS

$|A(\underline{k})|^2$ Point array wavenumber response

$|A_m(k_1)|^2$ Plate longitudinal shape factor

$|A_n(k_3)|^2$ Plate lateral shape factor

c_o Velocity of sound in air

D Flexual rigidity

$f_{mn}(x,z)$ Two-dimensional normal mode shape (m,n) mode

f_{mn} Natural frequency of (m,n) mode

$|F_{mn}(k_1 k_3)|^2$ Two-dimensional wavenumber filter shape function

$g_m(x)$ Longitudinal mode shape

$h_n(z)$ Lateral mode shape

H Boundary layer shape factor, $H = \delta^*/\theta$

$|H_{mn}(\omega)|^2$ Modal frequency response at resonance

k Wavenumber: k_1 = longitudinal; k_3 = lateral

k_A Acoustic wavenumber $k_A = \omega/c_o$

k_C convective wavenumber, $k_C = \omega/U_C$

L Structural dimension: L_1 = longitudinal; L_3 = lateral

LIST OF SYMBOLS (Continued)--

L_p Level in dB

$p(\underline{x},t)$ Instantaneous wall pressure fluctuation at position $\underline{x}$ and time t

$P_m(t)$ Measured area-averaged instantaneous pressure

$P_{mn}(\omega)$ Modal pressure, (m,n) mode

$P(k_1,k_3,\omega)$ Measured wavenumber-frequency spectral density of wall pressure

q Free stream dynamic head, $q = \frac{1}{2}\rho U_{c_o}^2$

$R(\underline{x},t)$ Cross-correlation of the wall pressure

$S_w(x,z,\omega)$ Theoretical displacement spectral density

$S_a(x,z,\omega)$ Theoretical acceleration spectral density

$S(\underline{x})$ Microphone facial sensitivity distribution

S Strouhal number

U_c Convective velocity

U_∞ Free stream velocity

V_* Friction velocity

$W(x,z,t)$ Instantaneous displacement at position (x,z)

LIST OF SYMBOLS (continued)--

$\|W(\underline{k})\|^2$	Microphone array wavenumber response
x	Longitudinal distance variable
z	Lateral distance variable
β	Damping force per unit mass
δ^*	Boundary layer displacement thickness
η	Damping loss factor
θ	Boundary layer thickness
ρ	Fluid density
σ	Structural surface density
$\Phi(k,\omega)$	Wavenumber-frequency spectrum of the wall pressure
$\Phi(\underline{k},\omega)_L$	Low wavenumber frequency spectrum of the wall pressure
$\Phi(\omega)$	Frequency spectrum of the wall pressure
ν	Kinematic viscosity
ω	Radian frequency
ω_{mn}	Resonant frequency at (m,n) mode
ω^*	Non-dimensional frequency $\omega^* = \dfrac{\omega\delta^*}{U_\infty}$

COMPARISON OF TECHNIQUES TO MEASURE THE LOW
WAVENUMBER SPECTRUM OF A TURBULENT
BOUNDARY LAYER

I. INTRODUCTION

The turbulent boundary layer that grows on vehicles
moving through a viscous fluid causes pressure fluctuations
on the surface of the vehicle. These pressure fluctuations
can be an important source of structural vibration and
contribute to the internal vehicle noise. These problems
are encountered in many marine applications and in high
speed aircraft.

The pressure field beneath a thick turbulent boundary
layer has been investigated in the past. Single flush
mounted transducers have been used to measure the root
mean square wall pressure levels and the single point wall
pressure spectra. Pairs of flush mounted transducers have
been used to measure the two point wall pressure statistics
of a turbulent boundary layer. These two point statistics
describe the convective ridge, i.e., the part of the wall
pressure spectrum associated with eddies convecting down-
stream at a major fraction of the freestream velocity.

In many marine applications the convective ridge is
inefficient at producing structural vibration due to the
low freestream velocities and the high frequencies of
interest. Sources of excitation better coupled to the
structural modes are the low wavenumber (long wavelength)
components of the turbulent boundary layer. These low

wavenumber components do not contribute significantly to
the single point wall pressure spectrum and so it is necessary
to construct spatial filters in order to measure them.

There are two methods of constructing spatial filters
for the measurement of the low wavenumber levels. Maidanik
and Jorgensen [1] have shown that an array of flush mounted
transducers can be used as a spatial filter. Blake and
Chase [2], Jameson [7] and Farabee and Geib [3] used this
technique. Aupperle and Lambert [4] showed how beams act
as wavenumber filters. Martin [5], Jameson [8], and
Moeller et al. [8] used the spatial filtering of clamped
plates to make low wavenumber measurements. To date the two
techniques have not been used in the same facility and have
tended to yield data in different nondimensional frequency
and wavenumber ranges. The agreement between the various
investigators has not been too good. There has been alot
of scatter in the reported data.

The current measurement program has been to utilize
both wavenumber filtering techniques in the same facility.
The Martin [5] clamped plate, the Jameson [8] clamped plate,
and the Farabee and Geib [3] 6-element microphone array
wavenumber filters were used to perform the low wavenumber
measurements. This will allow for a direct comparison of
the techniques used by the three primary investigators.

II. RESPONSE OF WAVENUMBER FILTERS TO TURBULENT BOUNDARY LAYER WALL PRESSURE FIELDS

2.1 Properties of Wall Pressure Spectra

The wall pressure field beneath a turbulent boundary layer is very complicated. The pressure fluctuations exerted on the wall are varied in both space and time. Statistical properties such as the root mean square wall pressure, the cross correlation, the spectral density, and cross spectral density, etc. are used to describe the pressure field.

The wall pressure beneath a turbulent boundary layer is denoted by $p(\underline{x},t)$, where $\underline{x}=(x_1,x_3)$ is the distance vector in the plane of the wall, x_1 is the streamwise direction and x_3 is the cross-stream direction. The component x_2 is normal to the wall. Assuming the wall pressure field is homogeneous and stationary, the cross-correlation of the pressure at two points on the boundary is

$$R(\underline{x},t) = < p(\underline{x}',t')p(\underline{x}'+\underline{x},t'+t) > \qquad (2.1)$$

where the brackets $< >$ represent a time average, $\underline{x}$ is the separation distance between the two points, and t is a time delay. The wavenumber-frequency spectrum is obtained from $R(\underline{x},t)$ by taking the Fourier transform over space and time,

$$\Phi(\underline{k},\omega) = \frac{1}{(2\pi)^3} \int \int \int R(\underline{x},t)\exp[-i(\underline{k}\cdot\underline{x}-\omega t)]dx\,dt \qquad (2.2)$$

where $i=\sqrt{-1}$, $\underline{k}$ is the vector wavenumber, ω is the radian frequency, and the integration limits are from $-\infty$ to $+\infty$.

$\Phi(\underline{k}, \omega)$ describes the distribution of energy in the pressure field in terms of frequency and wavenumber. The behavior of the wavenumber-frequency spectrum is determined by the decay and convection of eddies in the turbulent boundary layer field. The convection of eddies lead to a high value of wavenumber-frequency spectrum along a convective ridge defined by $k_c = \omega/u_c(\omega)$, where $u_c(\omega)$ is the convective velocity. A schematic of the distribution of energy at a fixed frequency is given in Figure 2.1. This shows the strong convective ridge centered at $k_c = \omega'/u_c$. It also shows that the acoustic energy is restricted to the region of wavenumber space $0 < k < \omega'/c_o$, where c_o is the speed of sound in the field.

The region of interest is the low wavenumber region $\omega'/c_o < k_L < \omega'/u_c$. To make a measurement in this region it is necessary to reject both the acoustic contamination and the convective contamination. Section 2.2 describes how a microphone array acts as a wavenumber filter and Section 2.3 describes how the response of a plate can be used as a wavenumber filter.

2.2 Microphone Array Wavenumber Filter

2.2.1--Single Microphone Response. The frequency spectral density of wall-pressure fluctuation at a point is

$$\Phi(\omega) = \frac{1}{2\pi} \int R(0, t\, e^{i\omega t}\, dt = \int \int \Phi(k, \omega)\, d\underline{k} \qquad (2.3)$$

The measurement of the frequency spectral density using a

single flush-mounted microphone involves the influence of the microphone facial sensitivity distribution $S(\underline{x})$ in averaging small-wavelength wall pressure components. When subject to a pressure field $p(\underline{x},t)$, the microphone, on assumption of instantaneous response, measures an area-averaged pressure

$$p_m(t) = \int \int S(\underline{x}) p(\underline{x},t) d\underline{x} \qquad (2.4)$$

where $\qquad \int \int S(\underline{x}) dx = 1 \qquad (2.5)$

The response function $|H(\underline{k})|^2$, expresses the facial distribution as a wavenumber filter and is defined by

$$H(\underline{k}) = \int \int S(\underline{x}) \exp[-i\underline{k} \cdot \underline{x}] d\underline{x} \qquad (2.6)$$

where $\underline{x}$ may be measured from the center of the face and $S(\underline{x})$ vanished for $\underline{x}$ outside the sensitive area. The frequency spectrum of area-averaged pressure measured by a single microphone is then given by

$$\Phi_M(\omega) = \int \int |H(\underline{k})|^2 \Phi(\underline{k},\omega) dk \qquad (2.7)$$

The frequency response of the microphone is assumed [2] to be independent of the wavenumber response and will be neglected in this discussion.

If the microphone is a circular transducer of radius R and uniform facial sensitivity, then

$$|H(\underline{k})|^2 = [2J_1(kR)/kR]^2 \qquad (2.8)$$

where $k^2 = k_1^2 + k_3^2$ and J_1 is a Bessel function of the first kind. The response $|H(\underline{k})|^2$ has an upper bound that decreases with kR and thus attenuates the high-wavenumber components of the pressure field.

The microphone actually used had a facial sensitivity significantly nonuniformed. The microphones used to perform the measurements were Bruel & Kjaer (B&K) Type 4144 Condenser Microphones with a diaphragm radius of 0.37 inches. The distribution of the facial sensitivity of a nearly identical microphone was measured by Bruel and Rasmussen [9]. This sensitivity function has negligible frequency dependence up to 2 kHz, and although the frequency filter decreases perceptibly beyond this, the spatial function S($\underline{x}$) for use in Equation (2.5) changes little up to 4 kHz.

The function S($\underline{x}$) derived from the measured sensitivity distribution with neglect of small phase differences and assumption of circular symmetry is shown in Figure 2.2. This function, which is now written S(r/R), with argument (r/R) defined as distance from the microphone center, can be closely approximated by [2]

$$\frac{S(r/R)}{S(o)} = B[1-\beta K_0(\frac{\alpha r}{R})] \qquad 0<r<R \qquad (2.9)$$

where B=0.198, α=2.96 and β=-4.06. (2.10)

as shown in Figure 2.2. Equation (2.10) permits the quadrature of Equation (2.6) to be performed to yield the

corresponding area averaging function, written as

$$|H(\underline{k})|^2 \equiv |H(kR)|^2 \quad \text{where [10]}$$

$$H(kR) = \frac{kR[1-\beta J_o(\alpha)]J_1(kR)+\alpha\beta J_1(\alpha)J_o(kR)-\alpha^2(kR)^{-1}J_1(kR)}{((kR)^2-\alpha^2)[\frac{1}{2}-(\beta/\alpha)J_1(\alpha)]} \tag{2.11}$$

Analytically, the attenuation of this function as $kR\rightarrow\infty$ can be estimated by using the approximations to Bessel functions of the large argument. In this approximation

$$|H(kR)|^2 \rightarrow 2c_o(kR)^{-5}\cos^2(kR-\pi/4) \tag{2.12}$$

where

$$c_o = \frac{4\alpha^2\beta^2 J_1^2(a)}{\pi[1-2(\beta/a)J_1(\alpha)]^2} \cong \tag{2.13}$$

for $kR \gg \alpha$ and $kR \gg 1$

Although the approximation to the measured sensitivity, given by Equations (2.9) and (2.10) is generally good, it has limited validity with regard to the small-scale variation of the true sensitivity near the element periphery. Accordingly, because of the sensitivity of H(kR) to variation at large kR, beyond some maximum kR, Equations (2.11) and (2.12) should not be used except for order-of-magnitude considerations.

The area-averaging function $|H(kR)|^2$ for the microphone, as approximated by Equations (2.10) and (2.11) is shown in Figure 2.3, along with the results of Equation (2.8) that would apply if the facial sensitivity were uniform. The difference is significant. The actual lobes were wider and

the rate of decrease from lobe to lobe is more rapid. The
actual microphone descriminates more effectively against
higher wavenumbers.

2.2.2--<u>Microphone Array Response</u>. Maidanik and Jorgensen
[1] have shown that a flush-mounted pressure transducer system
can be used to construct a wave-vector filter to study the
nature of the boundary pressure field in a turbulent boundary
layer. For a transducer system consisting of a linear array
of uniform microphones equally spaced, the wavenumber response
of wave-vector filter is

$$|W(k)|^2 = |H(\underline{k})|^2 |A(\underline{k})|^2 \qquad (2.14)$$

and the frequency spectrum measured by an array of micro-
phones is then

$$\Phi_M(\omega) = \int \int |W(\underline{k})|^2 \phi(\underline{k},\omega) d\underline{k} \qquad (2.15)$$

where $|H(k)|^2$ is the wavenumber response of a single micro-
phone as described in Equation (2.6) and $|A(k)|^2$ is the array
wavenumber response. The frequency response of the micro-
phone is assumed to be independent of the wavenumber response
in the frequency range of interest (see Section 2.2.1). For
the array of N uniform microphones equally spaced, and with
no time delays, the array response is

$$|A(\underline{k})|^2 = N^{-2} \left| \sum_{n=0}^{n-1} S_n \exp(-ink \cdot d) \right|^2 \qquad (2.16)$$

where $\underline{d}$ is the separation distance and S_n represents the magni-
tude and polarity of the sensitivity of the nth microphone.

The filtering action of the array can be modified by adjusting the magnitude and polarity of S_n for each microphone. This is called shading the array. The simplest shading is the uniform shaded or the unshaded array. For this type of shading the magnitude of each microphone is adjusted so that $|S_n|=1$. For an array of microphones aligned in the k direction, Equation (2.15) can be written

$$|A(k)|^2 = \frac{1}{N^2} \sin^2(\tfrac{1}{2}Nk_1d)/\sin^2(\tfrac{1}{2}k_1d) \quad \text{for } S_n=(-1)^{2n} \quad (2.17)$$

$$= \frac{1}{N^2} \sin^2(\tfrac{1}{2}Nk_1d)/\cos^2(\tfrac{1}{2}k_1d) \quad \text{for } S_n=(-1)^n+N \text{ even} \quad (2.18)$$

$$= \frac{1}{N^2} \cos^2(\tfrac{1}{2}Nk_1d)/\cos^2(\tfrac{1}{2}k_1d) \quad \text{for } S_n=(-1)^n+N \text{ odd} \quad (2.19)$$

Equation (2.17) is for a common phased array and is plotted in Figure 2.4 for N=6. The major characteristics of the array are shown on this figure. The main lobe occurs at $k_1d/\pi=0$, and aliasing lobes occur at $k_1d/\pi=2,4$, etc. The width of the main lobe and the aliasing lobe is $\pi/3d$.

Equations (2.18) and (2.19) are for an alternating phased array. This type of summing shifts the array response by $k_1d/\pi=1$. The characteristics are then the same as for the common phased array. The alternating phased array shifts the main lobe of the response out of the acoustic region, but does not shift it into the convective region. Thus the alternating phased array will produce the best low wavenumber results in the frequency region where the main lobe is between the

acoustic and convective region.

Equation (2.18) is plotted in Figure 2.5 for N=6. Also plotted on this figure is Equation (2.11), the response of a single B&K Microphone with d/R=1.63. The choice of d/R=1.63 is to nullify the effect of the first aliasing lobe of the array occurring at $k_1 d/\pi=3$ by the minimum in the single microphone response occurring at $k_1 R=5.8$. Nullifying the first aliasing lobe will reduce the effect of the convective ridge region as will be discussed in Section IV.

A significant amount of noise is still admitted by nearby minor lobes and more distant major lobes. The response of the actual microphone, Equation (2.10), reduces the acceptance at wavenumbers higher than that of the main lobe as was shown in Figure 2.3. In addition, suppression of the minor lobes can be accomplished by using a different type of array shading. This type of array shading is just assigning unequal weights S_n to microphone outputs in Equation (2.16).

Two different array shadings were used to suppress the minor lobes. One was Chebyshev shading [11]. This shading is an optimal method. The coefficients S_n can be chosen so as to reduce the minor lobes by any specific amount. For a given level of reduction the widening of the major lobe is minimized with respect to other shading. The other shading used was Binomial shading [12]. This method results in the total elimination of the side lobes for spacing less than one-half wavelength but greatly increases the main lobe's width. The effects of the two shadings described above will

be discussed in greater detail in Section IV.

2.2.3--<u>Array Design</u>. The microphones, preamplifiers, microphone power supplies, and mounting plate for the array were supplied by F.E. Geib, Jr. at the David Taylor Naval Ship Research and Development Center. The array is the same one tested by Farabee and Geib [3].

The microphones were 1" Bruel & Kjaer Type 4144 Condensor Microphones with diaphragm radius of R=0.35 inches. The array consisted of six microphones mounted flush in the wall of the test section aligned with the direction of the flow. The center to center spacing of the microphones was d=1.06 inches, giving a d/R ratio of 3.03. The desired ratio of 1.63 (d=0.86 inches) could not be obtained because the outer diameter of the Type 4144 microphone was 1 inch. Special caps were used for the microphones to eliminate discontinuities over the surface of the array.

The microphone signals passed through the B&K Type 2619 FET preamplifiers, B&K Type 2606 Microphone amplifiers, and then through a Precision Filter Programmable Multi-Channel Filter System. The signal then passed into an analog summation box that was built so the array could be used in real time. The box has six inputs, with the gain of each input controlled by a trimming potentiometer. Each input has an on-ground switch so that four, five or six elements can be tested. A schematic of the box is shown in Figure 2.6. The outputs of the box are the common phased array and the alternating phased array. The dynamic range of the summing

box is sufficient so that the box is not the limiting factor
in the array performance.

The performance of the array was qualitatively checked,
in-situ, using an acoustic source in the inlet to the muffler
diffuser. This caused a plane acoustic wave to travel down
the test section. The wavenumber of the acoustic wave could
be inferred from the relation $k_1 = \omega/c_o$, where c_o is the speed
of sound in air.

The microphones were calibrated using a B&K Pistonphone.
It yields a calibration at 250 Hz. The microphone response
was assumed to be flat through the frequency range of
interest, 1 kHz < f < 5 kHz. The microphones have a resonance
near 8 kHz. Near the resonance, the microphone frequency and
wavenumber response are independent and so an acoustic cali-
bration is not valid. However, the acoustic calibration is
useful for frequencies well below the microphone's resonant
frequency. The rejection of acoustic noise in the test
facility can be inferred from the acoustic calibration of
the microphones.

Figure 2.7 shows the result of the acoustic calibration
for the alternating phased uniform shaded array in both
frequencies as measured and the equivalent wavenumber. The
main lobe occurs at 6.3 kHz or $k=2.9$ in^{-1}. This is assumed
to be the main acceptance wavenumber region for the filter.
The sidelobes are approximately 12-15 dB down from the main
lobe. There are two nulls before the main lobe at 2.2 kHz
and 4.4 kHz. Data obtained at these frequencies will have a

reduction in the response to acoustic plane waves.

Figure 2.8 shows the effect of the Chebyshev and Binomial shading on the alternating phased array. For the Chebyshev shading, the reduction in the side lobe is approximately 30 dB and the width of the main lobe is approximately 1.5 times that for the Uniform shaded array. The Binomial shading virtually eliminates the side lobe, but the main lobe is increased to over twice that of the Uniform shaded array.

Figure 2.9 shows the result of the acoustic calibration of the common phased Uniformed shaded array. The main lobe occurs at k=0. The side lobes are again 12-15 dB down from the main lobe and the first two nulls occur at 2.2 and 4.2 kHz. The first aliasing lobe occurs about 12 kHz.

2.3 Structural Plate Wavenumber Filters

2.3.1--Plate Response. Aupperle and Lambers [4] have described analytically the wavenumber filtering action of beams. The concept of the wavenumber filter shape, $|A_m(k)|^2$, is shown to come from a normal mode analysis of structural response to random pressure excitation. Martin [5,12] discusses both analytical and numerical techniques for evaluating $|A_m(k)|^2$ for several ideal structures as well as techniques for measuring $|A_m(k)|^2$ via mode shape measurements. The techniques used within are the same as Martin [5] used and will be briefly summarized for rectangular plates.

The geometric configuration of the plate structure is shown in Figure 2.10. The structure is characterized by

dimensions L_1 and L_3, uniform mass per area σ, and flexual

rigidity D. The transverse displacement $W(x,z,t)$ represents

the response of the plate when excited by a normal random

pressure field $p(x,z,t)$ and subjected to a uniform damping

force per unit mass $\beta \frac{\partial W}{\partial t}$. The governing dynamic equation is

$$(D\nabla^4 + \sigma \frac{\partial^2}{\partial t^2} + \sigma \beta \frac{\partial}{\partial t}) \; W(x,z,t) \; = \; p(x,z,t) \qquad (2.20)$$

Solving this equation using normal mode techniques results in

$$W(x,z,\omega) \; = \; \sum_{m=1}^{\infty} \; \sum_{n=1}^{\infty} \; \frac{1}{\sigma(\omega^2 - \omega_{mn}^2 - i\beta\omega)} \; P_{mn}(\omega) f_{mn}(x,z) \qquad (2.21)$$

where ω_{mn} are the eigenvalues and $f_{mn}(x,z)$ are the normal

modes. The following normalization was used for the ortho-

gonal function

$$\int_0^{L_1} \int_0^{L_3} f_{mn}(x,z) \; f_{jk}(x,z) \; dxdz \; = \; \delta_{mj}\delta_{nk} \qquad (2.22)$$

P_{mn} is the modal pressure defined by

$$P_{mn} \; = \; \int_0^{L_1} \int_0^{L_3} p(x,z,\omega) f_{mn}(x,z) \, dx \, dt \qquad (2.23)$$

Martin [5,12] then shows when considering only the resonant

frequencies of the structure (ω_{mn}), and modal overlap is

negligible, the displacement response spectral density can

be written as

$$S_w(x,z,\omega_{mn}) \; = \qquad (2.24)$$

$$= f_{mn}^2(x,z) |H_{mn}(\omega_{mn})|^2 \int_{-\infty}^{\infty} \int |F_{mn}(k_1 k_3)|^2 \; \Phi(k_1,k_3,\omega_{mn}) dk_1 dk_3$$

where $\phi(k_1, k_3, \omega)$ is the wall pressure wavenumber-frequency spectrum as described in Equation (2.2). $|H_{mn}(\omega)|^2$ is the modal frequency response which at resonance is

$$|H_{mn}(\omega_{mn})|^2 = \frac{1}{(\sigma\beta\omega_{mn})^2} = \frac{1}{(\sigma\eta\omega^2)_{mn}^2} \qquad (2.25)$$

where $\eta_{mn} = (\beta_{mn}/\omega_{mn})$ is the loss factor. $|F_{mn}(k_1, k_3)|^2$ is the two-dimensional wavenumber filter shape defined as

$$F_{mn}(k_1, k_3) = \int_0^{L_1}\int_0^{L_3} f_{mn}(x, z) e^{i(k_1 x + k_3 z)} dx\, dt \qquad (2.26)$$

In an experimental sense Equation (2.24) can be used to relate the pressure excitation to the vibratory response if the modal characteristics $|H_{mn}(\omega_{mn})|^2$ and $|F_{mn}(k_1, k_3)|^2$ can be determined accurately. The evaluation of $|H_{mn}(\omega_{mn})|^2$ requires only a determination of the total damping and surface density associated with the modes under consideration.

In many cases the normal mode shape $F_{mn}(x, z)$ is easily separated into an x-dependent term and a z-dependent term. This separation of variables is analytically exact for plates having any two opposite sides simply supported. Even for the case of the fully clamped plate, a separation of variables technique using clamped beam function is often used as a reasonable approximation to the mode shape since an exact solution is unobtainable in closed form. To take advantage of this separation of variables, let

$$f_{mn}(x,z) = g_m(x) h_n(z) \tag{2.27}$$

Substitution of Equation (2.27) into Equation (2.25) yields

$$F_{mn}(k_1,k_3) = \int_0^{L_1} g_m(x) e^{ik_1 x} dx \int_0^{L_3} h_n(z) e^{ik_3 z} dz \tag{2.28}$$

Defining

$$A_m(k_1) = \int_0^{L_1} g_m(x) e^{ik_1 x} dx$$

$$A_n(k_3) = \int_0^{L_3} h_n(z) e^{ik_3 z} dz \tag{2.29}$$

then $|F_{mn}(k_1,k_3)|^2$ can be expressed in terms of one dimensional filter shapes as

$$|F_{mn}(k_1,k_3)|^2 = |A_m(k_1)|^2 |A_n(k_3)|^2 \tag{2.30}$$

Substituting Equations (2.29) and (2.24) into Equation (2.23) results in

$$S_w(x,z,\omega_{mn}) =$$

$$= \frac{f_{mn}^2(x,z)}{(\sigma\eta\omega^2)_{mn}^2} \int_{-\infty}^{+\infty}\int |A_m(k_1)|^2 |A_n(k_2)|^2 \phi(k_1,k_3,\omega_{mn}) dk_1 dk_3 \tag{2.31}$$

This equation forms the basis for evaluating the acoustic, convective and low wavenumber response.

2.3.2--<u>The Martin Plate</u>. The Martin plate tested was the clamped plate Martin [5] used in 1976. The aluminum plate was removed from its frame, refurbished, and then epoxied to the frame using EccoBond 45 Epoxy. The plate was made from 0.034" aluminum sheet stock. The frames were constructed from 3/4" thick by 3" wide steel members which were machined to the required lengths and bolted together. The total weight of the frame was about 30 lbs., and the ratio of frame to plate mass was nearly 200:1.

The plate's physical characteristics are as follows:

Surface dimension: $L_1 = 0.508m$, $L_3 = .0762m$;
Thickness: $8.64 \times 10^{-4}m$;
Surface density: $2.37 kg/m^2$.

The modal characteristics of the plate were determined after the plate was refurbished. The same procedure as Martin [5] used was repeated. To identify the modes, the plates were driven at a single frequency by a small area acoustic drive. When a resonant response was observed, the modal pattern was determined by lightly dusting the structure with sand to produce Chladni patterns. The odd number modes from the (3,1) to the (21,1) mode were identified.

The damping factors (η_{nm}) for the plate modes were determined experimentally from decay rate measurements. The small area acoustic drive was used to excite the structure at its natural frequencies, and the vibratory response at the location of interest (in this case at the center of the plate)

was monitored with a Wilcoxon Model 91 Accelerometer. After
adjusting the drive level to achieve a reasonable response
signal, the excitation was shut off, and the resulting decay
transient was captured on a B&K Model 7502 digital event
recorder. The decay transient was then played back at a
slower speed, and the decaying rms signal level was recorded
on a B&K Model 2305 graphic level recorder. The damping
factor (η_{mn}) is determined by the equation

$$\eta_{mn} = 1.833R_1\tan\alpha/f_{mn} \tag{2.32}$$

where R_1=recording rate/playback rate; α=decay angle;

   f_{mn}=natural frequency (Hz).

Table 2.1 lists the experimentally determined resonant
frequencies and damping factors. These are compared with
those values determined by Martin [5] in 1976. The comparison
is quite good.

2.3.3--<u>The Jameson Plate</u>. The Jameson plate tested
used the same steel bar frame and similar fixture as Jameson
[8] used in 1975. The steel plate used by Jameson was
replaced by a stainless steel plate. The plate thickness was
24 gauge, the same as Jameson used. The plate, 22.8 inches in
diameter, was flush mounted to a flat surface. The active area
of the plate is a rectangle of area 500 cm^2 with side lengths
in the ratio of 3 to 2, the longer side in the downstream
direction. The outside part was glued to wood to provide
mechanical support and damping; large steel bars (1.5"x0.75")
were epoxied to the underside to make a framework defining

the active area. The steel bars clamped the plate edge,
isolating the active area. The unsupported plate between the
wood and the beam, about one-quarter the length of a bending
wave at frequencies of interest, increased isolation from
vibrations of surrounding surface by acting as a quarter-wave
choke.

The plate's physical characteristics are as follows:

Surface dimension: L_1=0.274m; L_3=0.183m;

Thickness: 6.07×10^{-4}m;

Surface density: 4.92kg/m^2.

The modal characteristics of the plate were determined
using the same technique as was used for the Martin plate.
The response was monitored at two locations. First, at the
center of the plate to monitor the odd-odd modes. The second
location was at the center of the long direction of the plate
with the accelerometer moved along this midline until the anti-
node of the odd, 2 modes were located. The response was
monitored with a Wilcoxon Model 95 Accelerometer.

The results of the modal characteristic test are shown in
Table 2.2 and compared with Jameson's [8] 1975 results. The
comparison was not good. Three attempts were made to epoxy
the bars to the plate. All attempts resulted in the same
modal characteristics as shown in Table 2.2

III. EXPERIMENTAL FACILITIES

This section describes the experimental facilities and
the experiments. In Section 3.1 the Wind Tunnel is described.
The test set ups and boundary layer measurements are described
in Section 3.2. The background acoustic noise measurements
are described in Section 3.3, and a comparison of noise in
the M.I.T. Facility is made with the BBN Facility in Section 3.4.

3.1 M.I.T. Low Noise, Low Turbulence Wind Tunnel

The experiments were conducted in the M.I.T. low noise,
low turbulence wind tunnel using the equipment of the M.I.T.
Acoustics and Vibration Laboratory. The wind tunnel is shown
in Figure 3.1 and is described in Hanson [13]. The wind
tunnel consists of an intake, a flow straightening section, a
test section enclosed in an air tight blockhouse, a muffler
diffuser, and a variable speed centrifugal blower.

This wind tunnel has been used for low wavenumber measure-
ments by Martin [5] and by Moeller et al. [6]. The wind
tunnel has been modified since the experiments of Moeller et
al. The semianechoic treatment in the blockhouse has been
changed since the previous experiments were conducted. The new
treatment consists of a 4 inch blanket of urethane foam
covering the walls, floor and ceiling of the blockhouse. A
set of 4 inch foam blocks was then draped at random on the
walls, floor, and ceiling, with a set of 2 inch foam blocks
draped randomly over the 4 inch blocks. This change in semi-
anechoic treatment did not significantly affect the low wave-
number measurement program.

The wind tunnel was operated in the free jet mode. This
was done to isolate the wavenumber filters in the test
sections from noise propagating upstream from the blower. The
isolation was provided by allowing the noise to propagate into
the blockhouse and be absorbed by the semianechoic treatment.

3.2 Boundary Layer Tests

3.2.1--Test Boundary Configurations. The low wavenumber
measurements were conducted in three different test configura-
tions. The first configuration was to test in a hard walled
duct using the same ducting as Martin [5] and Moeller et al.
[6]. This test confiugration is shown in Figure 3.2. This
configuration was used for both structural filtering tests
and microphone array tests.

The next configuration tested was a lined duct. The
duct was lined with a 1 inch thick blanket of urethane foam
to attenuate the cross modes propagating in the duct. The
foam is faced with a coating to provide a smooth surface to
the flow. This configuration was used only for structural
wavenumber filtering tests.

The final configuration tested was similar to the test
configuration used by Jameson [7,8] at Bolt, Beranek & Newman
and is shown in Figures 3.3 and 3.4. The wind tunnel was
operated in the wall jet configuration. The walls of the
duct were removed and only the bottom remained in place. The
boundary layer on the bottom wall of the ducting was allowed
to develop naturally. Tests were done at two different
locations in this configuration. The first was 1.34 meters

downstream of the contraction exit plane. The second was
0.45 meters downstream of the contraction exit.

The open duct configuration produced the best results.
The hard walled duct allowed cross duct mode to propagate
upstream from the blower. The lined duct was thought to
generate as well as absorb high-frequency noise. The open
duct took greatest advantage of the blockhouse semianechoic
treatment. These conclusions are in agreement with
Jameson [7].

The results presented in this report will be only for two
different locations of the open duct configuration.

3.2.2--Boundary Layer Profiles. The boundary layer pro-
perties were measured for speeds ranging from 15 m/s to 40 m/s
for each configuration tested. The boundary layer profiles
were measured at the center of the test plate using a United
Sensors 0.035" total head tube and a static tap on the test
section wall. The pressure differences were measured using a
Validyne DP-15 pressure transducer that was calibrated against
a Beta micromanometer. The boundary layer parameters displace-
ment, thickness, δ^*, and momentum thickness, θ, were determined
by integrating the boundary layer profiles. The shape factor
$H=\delta^*/\theta$ was then calculated. By fitting the boundary layer
profiles to a law of the wall, the friction velocity, V_*, was
determined from the slope of the logarithmic overlap region of
the law of the wall. The boundary layer properties are
summarized in Table 3.1

The outer mean flows of the boundary layers follow quite closely the velocity-defect law derived from Cole's Law of the Wake. This law may be written [14]

$$u^+ = 1/K \log_e y^+ + B + \Pi/K \, W(y/\delta) \qquad (3.1)$$

where

$$W(g/\delta) \cong 2\sin^2(\frac{\Pi}{2} \frac{y}{\delta}) \qquad (3.2)$$

The wake parameter $\Pi=0.55$ for the zero-pressure-gradient boundary layer, $K=0.4$ is the von Karman universal constant, and the constant $B=5.0$. The agreement between a typical measurement and Equation (3.1) is shown in Figure 3.5. The agreement is good.

3.2.3--Single Point Wall Pressure Spectra. The single point wall pressure spectra were measured for each test configuration. The measurements were performed using a B&K 1/8" microphone with a 1/32" pinhole cap. The microphone was flush mounted at the center of the measurement location. The results were nondimensionalized on the previously determined boundary layer properties and are compared to Burton [15] and Blake [16,17] in Figure 3.6.

The single point wall pressure spectra are a measurement of the convective ridge levels at a particular frequency. The small area microphone does not attenuate the signal very much until the point where $\omega R/u_c=1.0$ is marked on the plots. The single point wall pressure spectrum levels measured this way are used to make estimates of the convective ridge contamination of the wavenumber filters.

3.3 Measurement of the Background Acoustic Noise

An accurate measurement of the background noise in the test facility is necessary to insure the quality of the low wavenumber data. The test set up used to measure the background noise in the blockhouse is shown in Figure 3.7. The levels were determined using a B&K 4144 1 inch microphone. The current measurements are compared to those of Martin [5] for the same test configuration in Figure 3.8. The noise in the blockhouse has not changed much since the earlier tests.

The wavenumber filtering behavior of the 1 inch flush mounted B&K Type 4144 microphone was used to provide an estimate of the acoustic noise at the measurement location. The measurement technique is the same as the single point wall pressure measurement. The 1 inch microphone was flush mounted using a cap that was designed and used by Farabee and Geib [3] in their experiments. The microphone's diaphragm was exposed such that it could be flush mounted in the test section.

The large area microphone is essentially a low pass filter in wavenumber. The typical single point spectrum levels measured this way are shown in Figure 3.7 for the wall jet test configuration and a test speed of 15 m/s. The low frequency behavior shows the response of the microphone to the convective ridge. The convective ridge is at $k_c = 2\pi f/u_c$. The microphone rapidly attenuates the convective ridge information by averaging it out over the face of the microphone. What is left at the higher frequencies, where the single point spectrum changes

levels slowly, is made up of background acoustic noise and the
low wavenumber components of the wall pressure spectrum.

A pair of microphones were used in the background noise
test configuration. The HP5425 Analyzer was used to compute a
normalized cross-spectrum between the pair of flush mounted
microphones. The pressure spectrum levels are shown in
Figure 3.9 and are the same at both measurement locations.
The separation between the microphones was 2.12 inches. The
normalized cross-spectrum is shown in Figure 3.10. The
coherence between the two microphones is shown in Figure 3.11.
In the region where the pressure spectrum levels are flat the
coherence between the two microphones is between 0.5 and 0.7.
In this region the phase of the normalized cross-spectrum shows
a linear phase delay that corresponds to acoustic wave propa-
gating upstream from the blower. In Figure 3.12 the single
point spectrum for a speed of 40 m/s is shown and in Figure 3.13
the corresponding normalized cross-spectrum is shown. Because
of the higher speed, the convective region of the single point
pressure spectrum extends to higher frequency than those of
the lower speed case. The phase of the normalized cross-
spectrum shows two distinct regions of linear phase delay. In
the low frequency region is a linear phase delay that corresponds
to turbulent eddies convecting downstream at a major fraction of
the freestream velocity. Conversely, in the high frequency
region one can see a phase delay of the opposite sense
corresponding to an acoustic wave propagating upstream from the
blower. The combination of the coherence between the pair of

microphones at the higher frequencies and the phase delay
corresponding to an acoustic wave propagating upstream, leads
to the interpretation of the pressure spectrum levels at the
higher frequencies to be primarily acoustic in nature.

The acoustic levels at the test location determined by the
large area flush mounted transducer are compared to the back-
ground noise measurements for the same test conditions with
the result shown in Figure 3.14. The acoustic levels at the
wavenumber filter location are more than 10 dB louder than
the blockhouse noise levels. The blockhouse noise levels under-
estimate the acoustic contamination of the wavenumber filter
data. This is due to the acoustic source downstream in the
blower being much more directive than previously anticipated
(see section 4.3.4 for further discussion).

3.4 Comparison of the M.I.T. Facility with
     the Bolt, Beranek & Newman Facility.

The current background noise and single flush mounted
microphone measurements are compared to those made by
Jameson [7] at Bolt, Beranek and Newman, Inc. The Jameson
data is from Figure 10 of BBN Report No. 1937 at a speed of
55 ft/s or 16.8 m/s. Figures 3.15 and 3.16 compare the
current measurements at 15 m/s and 20 m/s with the Jameson
measurements.

The scaling on Figures 3.15 and 3.16 is the same as
Jameson used. The length scale for the Strouhal parameter is
a fixed quantity equal to 0.139 inches, which happens to be
the average value of the displacement thickness for Jameson's
boundary layers. That the length scale is the average value of

the displacement thickness was just a matter of choice. Blake and Chase [2] used the microphone radius for the length scale.

Figures 3.15 and 3.16 indicate that for the flush mounted microphones, above a Strouhal number of 6, about 2.5 kHz, the levels are 3-4 dB higher at the M.I.T. Facility. The region above 2.5 kHz (see Section 3.3) is the region in which the flush mount microphone is thought to be measuring acoutic waves propagating upstream from the blower in the M.I.T. Facility. The background noise measure, although sensitive to position in the blockhouse and perhaps not indicative of what is happening in the flow, shows the M.I.T. Facility to be as quiet or slightly quieter than the BBN Facility.

IV. WAVENUMBER FILTERS MEASUREMENTS

4.1 Experimental Source of Excitation

As discussed in Section 2.1 and shown in Figure 2.1, at
a given frequency, wavenumber-frequency wall pressure spectrum
consists of convective, acoustic and low wavenumber components.
A reasonable model for the wavenumber-frequency spectrum is
to assume that the three components are statistically indepen-
dent and can be written as a sum

$$\Phi(\underline{k},\omega) = \Phi(\underline{k},\omega)_{conv.} + \Phi(\underline{k},\omega)_{acoustic} + \Phi(\underline{k},\omega)_{low\ k} \qquad (4.1)$$

Equation (4.1) can be used with Equation (2.23) to obtain the
total structural response as a sum of convective, acoustic and
low wavenumber responses. The wavenumber filters are designed
to reject or minimize the acoustic and convective contamination.
To ensure that the measured response is dominated by the wave-
number contribution, it is important to estimate the magnitude
of response due to acoustic and convective excitation. If
the measured response exceeds the predicted contaminating
levels by a sufficient amount, it is appropriate to use the
measured data to determine the actual magnitude of $\Phi(\underline{k},\omega)_{low\ k}$.

The estimate of the contamination levels is not trivial.
The levels of the convective contamination is only known near
the convective ridge, and the response of the filters (plates
or microphones) is not accurately known at high wavenumbers
where the convective ridge is located. In addition, because of
the directivity of the acoustic contamination source (see

Section 3.3), a blockhouse microphone will not measure the proper levels and a single flush mounted microphone will be convectively contaminated.

Because of the above difficulties, this report will not include a quantitative estimate of the response due to the contaminations. The levels measured will be upper bound to the low wavenumber levels. Qualitative estimates of the contamination will be given for the microphone array and the plates in Section 4.2 and 4.3 respectively. Estimates of the contaminated response have been done by earlier investigators [2,3,5,6,7,8] on the filters used in this measurement program, and contamination estimates can be found in the literature.

4.2 Microphone Array Measurements

4.2.1--Alternating Phased Array Measurements. Measurements using the microphone array were performed at 15, 20, 25, 30, 35 and 40 m/s. Data was obtained with a single 1 inch microphone, a 1/8 inch microphone with a 1/32 inch pinhole cap, and with the array of six microphones operating in the common phase mode and the alternating phase mode for each speed using uniform, Chebyshev and Binomial shading.

Figure 4.1 shows a comparison of the wall pressure measurements obtained with a single 1/8 inch microphone with pinhole cap, a 1 inch microphone, and the alternating phased array with uniform shading at 15 m/s. In addition, the blockhouse noise measurement is shown. The ordinate in Figure 4.1 is the mean square pressure in a 1 Hz frequency band and the abscissa is frequency.

Before discussing the response of the array, it is
helpful to study the relationship between the peak of the
array sensitivity (the major lobe) and the turbulent and
acoustic pressure spectra as shown in Figure 4.2. The major
lobe is at a fixed wavenumber k_{10}. The pressure measurements
are made in frequency space. As the frequency increases, the
array encounters the convective peak first at $\omega = k_{10} u_c$. As
frequency is further increased, the low wavenumber region is
encountered next, and finally the acoustic region at $\omega \geq k_{10} c_o$.
The same relation is also valid concerning the array nulls
and aliasing lobes.

4.2.2--<u>The Convective Region-Alternating Array</u>. Returning
to Figure 4.1, the 1/8 inch microphone with pinhole cap can be
assumed to be indicative of the convective ridge levels at a
particular frequency. The attenuation of the convective
ridge by a single 1 inch microphone can be readily seen by
comparing the two microphones.

Referring to Figure 3.10, the phase relation between two
1 inch microphones at 15 m/s, the microphones respond strongest
to the convective ridge below 1 kHz, between 1 kHz and 2.5 kHz
the phase denote a transition region, and above 2.5 kHz the
response is primarily to acoustic excitation coming from down-
stream. A similar phenomenon can be observed by comparing the
slope of the 1 inch flush mounted microphone with the block-
house microphone in Figure 4.1. The slopes become almost
parallel when the flush mounted microphone is responding to
the acoustic excitation.

Next observing the alternating phased array curve on
Figure 4.1 and starting from the low frequencies, a peak occurs
at 175 Hz. This peak is the coincidence of the major lobe at
$k=2.9$ in^{-1} (see Figure 2.7) with the convective peak. The
next peak at 525 Hz is due to the coincidence of the first
aliasing lobe at $k_1=8.8$ in^{-1} with the convective peak. Because
of the physical size of the microphone, it was not possible to
space the microphones to cancel the first aliasing lobe as
described in the ideal case in Section 2.2.2. The nulls in the
array response have been smoothed out by the response of the
major lobe and first aliasing lobe to the convective ridge.
All that can be seen is the dip between the two main lobes
response.

Figure 4.3 shows the coherence between the array response
and a single 1" microphone in the array. The response of the
main lobe and first aliasing lobe is readily evident in this
figure with the main lobe having a coherence about 0.7 and
the first aliasing lobe has a coherence about 0.35.

As the flow speed is increased, the coincidence of the
array main lobes with the convective ridge occurs at higher
frequencies. This can be clearly seen in Figure 4.4 where the
array response at 40 m/s is compared with the array response at
15 m/s. In addition, the first null in the acoustic region
which is evident at 15 m/s at 2.2 kHz is smoothed over by the
convective region. This is further substantiated by referring
to Figure 3.13, the phase relation between two microphones at
40 m/s. The convective region is clearly more evident and

extends to about 2kHz, with the transition region before the acoustic region being reduced.

The above figures indicate that to minimize the convective contamination, data should be obtained at the lowest speeds. The lowest speed that reasonable data was obtained (i.e., where the array response was at least 6 dB above the electronic noise floor) was 15 m/s. The least convectively contaminated data was obtained in the 15 to 25 m/s speed range.

4.2.3--The Acoustic Region-Alternating Array. The test set up shown in Figure 3.7 was used to determine the acoustic sensitivity of both the structural wavenumber filters and the microphone arrays. The loudspeaker was located upstream of the wind tunnel inlet. A two point normalized cross-spectrum was computed for this case. The excitation was white noise and there was zero flow velocity. The result is shown in Figure 4.5. The normalized cross-spectrum shows a flat magnitude and a linear phase delay. The coherence is good between the two microphones. The result is approximately an acoustic wave travelling down the test section. This set up was then used to determine the acoustic sensitivities of both types of wavenumber filters.

When comparing the phase relation in Figure 4.5 with the phase relation at a flow of 15 m/s in Figure 3.10 and the phase relation at a flow of 40 m/s in Figure 3.13, the slope at frequencies above 2.5 kHz of the flow curves is the negative of the acoustic curve. Both show a linear phase with the acoustic test indicating a plane wave propagating downstream

and the flow tests indicating a plane wave propagating upstream.

The test setup shown in Figure 3.7 was used to calibrate the array by computing the transfer function from one of the array elements to the array output. The acoustic calibration of the alternating phased uniformly shaded array was shown in Figure 2.7 and the major characteristics were described in Section 2.2.3.

Returning to Figure 4.1, and observing the array response at 15 m/s, as the frequencies increase beyond the convective region, the array dips below the blockhouse noise measurements. Two minimas are observed at 2200 Hz and 4200 Hz corresponding to the coincidence of the two nulls on either side of the side lobe before the major lobe of the array at $k_1 = 1.02$ in^{-1} and 2.04 in^{-1} and the sonic line $\omega = k_1 c_o$. These minima are more evident in the coherence plot at 15 m/s shown in Figure 4.3. The coherence at the two minimas or the nulls in the acoustic calibration, the coherence is practically zero.

After thw two minimas, the array response increases and a maxima occurs at 6.3 kHz. This maxima is due to the coincidence of the major lobe with the sonic line. This maxima asymptote with the single 1" microphone.

Again the fact that the frequency where the array responds essentially to an acoustic plane wave asymptotes to the single microphone response and coherence of the array is practically zero at the nulls of the plane wave acoustic calibration is another indication that the single microphone above

2.5 kHz is responding to predominately an acoustic plane wave traveling upstream.

4.2.4--<u>The Low Wavenumber Region-Alternating Array</u>. The low wavenumber region in the frequency response of the array occurs between the first aliasing lobe response of the convective region and the main lobe response of the acoustic region. The best frequencies to extract the low wavenumber data for the alternating phased uniformly shaded array would be at the two nulls, 2200 Hz and 4200 Hz, at speeds between 15 to 25 m/s. These frequencies have the effect of spatial averaging attenuation of the convective ridge and the array minimization of the acoustic contamination.

The low wavenumber region, except possibly at the two nulls, is dominated by the side lobe response. As discussed in Section 2.2.2, the side lobes can be suppressed by using a different type of array shading. Figure 4.6 shows a comparison of the alternating phased array response for uniform shading, Chebyshev shading and Binomial shading. Figure 4.7 shows the coherence of the shaded arrays with a single microphone in the array. As was discussed in Section 2.2.2, the Chebyshev shading reduces the minor lobe with the minimum widening of the major lobe, and the Binomial shading totally eliminates the minor lobe but greatly increases the major lobe's width. These effects are most evident in the acoustic region. For the Chebyshev shading, the minor lobe between the two nulls has been virtually eliminated. The coherence at this location is almost zero. Low wavenumber data can therefore be taken

anywhere in this region. The binomial shading, although it eliminates the minor lobe, increases the width of the major lobe so that the sonic response of the major lobe contaminates the second null and the minor lobe region between the first and second null. Only in the vicinity of the first null can good low wavenumber data be obtained.

4.2.5--The Common Phased Array. The common phased array has its major lobe response centered at $k_1=0$. Referring again to Figure 4.2, the main lobe occurs at the very low frequency for both the convective ridge and the sonic line $\omega=kc_o$. If as assumed, the acoustic contamination is primarily plane wave so that there are no trace waves, then at higher frequencies there should be minimal acoustic contamination.

Figure 4.8 shows a plot of the common phased array. The initial peak at the lower frequencies is masked because of use of a high pass filter at 100 Hz. The first aliasing lobe is coincidental with the convective ridge near 375 Hz. Two minimas occur which are the nulls in the acoustic response. They occur at approximately 2.4 and 4.2 kHz. Their location is more evident in Figure 4.9 showing the coherence of the common phased array. It is at these two locations where the low wavenumber measurement will be taken.

4.3 Plate Measurements

4.3.1--The Martin Plate. Martin [5] made mode shape measurements of selected modes of all his spatial filters. The mode shapes were Fourier transformed (see Equation 2.29)

by numerical techniques to obtain the wavenumber filter

shapes $|\overline{A}_m(\overline{k})|^2$. A reprint of the wavenumber filter shape

measured and computed by Martin [5] for the (15,1) mode is

shown in Figure 4.10. Also on Figure 4.10 is the curve for

the envelope of the peaks for the ideal clamped beam. The

comparison between the two is good.

As expected, the plot is characterized by a major lobe

which peaks near the characteristic wavenumber $\overline{k}_m$ of the mode

and a series of side lobes at higher and lower wavenumbers. On

Figure 4.10, in the high wavenumber vicinity, is indicated the

convective wavenumber $\overline{k}_c$ for a free stream velocity of 40 m/s.

At this point the wavenumber response is more than 40 dB down

from the main lobe. However in the acoustic region (the lower

wavenumbers) the wavenumber response is only 20 dB down from

the main lobe. This indicates that the plates are a better

rejector of convective contamination than they are of acoustic

contamination.

Measurements using the plate filters were performed at

15, 20, 25, 30, 35 and 40 m/s. A typical plate acceleration

spectrum excited at 40 m/s is shown in Figure 4.11. The

acceleration was measured at the center of the plate. The

spectrum exhibits sharp resonances corresponding to the odd

numbered modes ranging from (3,1) mode to the (21,1) mode.

The fundamental mode does not appear in a distinct form. Its

response would be expected to be severely limited by radiation

damping, and it is also quite likely that a model overlap

situation exists between the fundamental and the (3,1) mode.
Above 4kHz the third order lateral modes appeared and created
another modal overlap situation. The intermediate modes
(i.e., 7,1 mode through the 17,1 mode) are well separated in
frequency and have peak levels which are well above the
observed background levels. These are the modes that were
used to make low wavenumber measurements.

4.3.2--<u>The Jameson Plate</u>. The Jameson plate was designed
to have higher order lateral modes in the frequency range
of interest. Unlike the Martin plate, the lateral filter shape
$|A_n(k_3)|^2$ major lobe is not always centered at $k_3=0$ but is
located at the characteristic wavenumber k_n. As indicated in
Equation (2.30), the total wavenumber response can be expressed
as a product of the one dimensional wavenumber response. Each
one dimensional wavenumber response is similar to the one shown
in Figure 4.10 for the Martin plate.

The exact shape of the wavenumber response of the Jameson
plate is not known since mode shape measurements were not made.
As indicated in Section 2.3.3, the measured natural frequencies
for a particular mode were not as expected. When compared to
approximated calculated values, the natural frequencies occurred
between the case for clamped edges and the case for simple
supported edges, while the values measured by Jameson [8] in
1975 approached the clamped condition. There were no constant
shift in frequency to expect a difference in plate thickness
or material properties. It was assumed that the boundary
conditions were not met because of a poor bond. As mentioned

previously, three attempts were made to achieve the desired
boundary condition (one attempt was made by an outside facility),
all attempts had the same results. The epoxy used was the same
as Jameson used. The plate material however was stainless
steel and not steel. It is not known whether the plate
material would make a difference or not. Jameson [8] did have
more difficulty with a brass plate than he did with the steel
plate.

Low wavenumber measurements were made on the Jameson
plate at 15, 20, 25, 30, 35 and 40 m/s. Figures 4.12 and
4.13 show a typical acceleration spectrum for the two locations
monitored. The spectrum in Figure 4.12 is when the plate was
monitored at the center of the plate and the response of the
odd-odd modes were measured. The spectrum in Figure 4.13 is
for the case where the accelerometer was at the center of the
long direction of the plate and moved along this mid-line
until the anti-node of the odd, 2 modes were located.

Modal overlap is a more serious problem for the Jameson
plate than the Martin plate. The Jameson plate exhibited
the same limitation in the lower frequencies due to radiation
damping and modal overlap, but the problem of modal overlap
existed at all frequencies because of the addition of higher
order lateral modes. An attempt was made to select modes
that were well separated for the low wavenumber measurements.
The modes selected are indicated on Figures 4.12 and 4.13.

4.3.3--Plate Convective Response. As mentioned in
Section 4.1, because of uncertainties about the shape of
the convective ridge and the response of low wavenumber
filters to high wavenumber excitation, estimates of convective
contamination is not trivial and only qualitative estimates
will be provided.

Martin [5] predicted by calculation that his membranes
and s-c-s-c plate exhibits a flow speed dependence of $(U_\infty)^9$
while the clamped plate has $(U_\infty)^{11}$ dependence. This means,
in general, the convective response will become increasingly
significant at the higher flow speeds. Martin [5] also
indicated from calculation that the clamped plate will have
less convective response by a factor $(\overline{k}_m/\overline{k}_c)^2$ than the s-c-s-c
plate, where the $(\overline{k}_m/\overline{k}_c)$ in the experiments range from 0.07 to
0.25. The clamped plate would therefore be expected to have
significantly less convective response than the s-c-s-c plate.

Martin [5] predicted the levels of the plate's convective
response and compared those with his measured response. The
convective estimates of the clamped plate were found to be
10 to 30 dB below the measured levels and were not considered
a significant contaminant. The s-c-s-c plate did have some
predicted responses within 4 dB of the measured responses at
50 m/s. This data was discarded, Comparing Martin's [5]
measured results for the clamped plate with the measured
results for the s-c-s-c plate shows that the s-c-s-c plate
measures lower values (even when corrected for differences in
damping and frequency) than the clamped plate. This indicates

that convective response is not the significant contaminant for the s-c-s-c plate.

Jameson [8] concluded similar results concerning convective contamination. The present data for the Jameson plate is also assumed not to be seriously convectively contaminated even though the plate boundaries may be simply supported. This assumption is made based on comparison of the two Martin plates.

4.3.4--Plate Acoustic Response. The wavenumber response of a single mode, determined by Martin [5] and shown in Figure 4.10 indicated that the plate responds better to the low wavenumber acoustic waves than the high wavenumber convective waves. Both Martin [5] and Jameson [8] determined their plate's acoustic response by the same method. An acoustic source was used to insonify the blockhouse, similar to the test setup shown in Figure 3.7, and the coupling between the sound measured by a microphone located outside the flow and the plate response was calculated to determine the plate's acoustic sensitivity. The level of the acoustic contamination was estimated using the blockhouse microphone during the flow tests. From these results, the acoustic contribution to the modal excitation was estimated.

Jameson [8] kept only the data for which the acoustic contribution was at least 8-10 dB below the measured data. Martin [5] calculated acoustic contribution typically fell below, but reasonably close to, the measured levels. Data points that were less than 4 dB below the measured data were discarded.

The acoustic contamination estimates were repeated for both the Martin plate and the Jameson plate in the open jet configuration. The results were similar for both plates. The acoustic contamination estimates typically fell below, but reasonably close to, the measured levels. Very few of the acoustic estimates, however, were 8-10 dB below the measured levels. Also, at the lower flow speeds, where there is less convective contamination, more modes had acoustic contamination estimates that exceeded the measured levels.

The accuracy of the acoustic contamination estimates are highly suspect. As indicated in Section 3.2.3, the primary acoustic source located downstream in the blower is thought to be more directive than previously anticipated. A rough estimate of the directivity of the acoustic source can be calculated by modeling the source as an equivalent circular cylinder with an area equal to the area of the duct. This assumes that the acoustic contamination is primarily plane wave.

The directivity pattern for a circular piston [18] is

$$D(\theta) = \frac{2J_1(ka\sin\theta)}{ka\sin\theta} \qquad (4.2)$$

where θ is the polar angle from the axis of the cylinder, a is the radius of the cylinder. Values of the directivity function, $2J_1(x)/x$, are plotted as a function of x in Figure 4.14. It can be observed from the plot that the curve has zero crossings at x=3.83,7.02, etc.

For a duct 15"x15", the equivalent circular radius is
8.5". Figure 4.15 plots the polar angle, Θ, versus frequency
for directivity pattern 3 dB down, 6 dB down, and the first
null for such a duct. The directivity of the acoustic con-
tamination, especially in the higher frequencies, is obvious
from the plot.

The speaker used to insonify the blockhouse is also
directive. However, its directive pattern is probably
different than the acoustic contamination occurring during
flow and is dependent on its location. Because of the
differences in directivity patterns, the plate could respond
quite differently to the same level measured by the blockhouse
microphone for the two cases. As an example, Table 4.1 shows
the results of two acoustic sensitivity tests with the
speaker in two different locations. The first test on the
speaker was located in the inlet of the diffuser (see Figure
3.1). In the second test, the speaker was located at an inlet
of the wind tunnel (see Figure 3.7). As the table indicates,
for some modes there could be quite a difference.

In light of the above, the method for determining the
plates' acoustic response can only be considered an indication
of the acoustic contamination, and no real values can be
assigned.

As mentioned in Section 4.3.3, Martin's [5] s-c-s-c
plate resulted in lower levels than the clamped plate. In
addition, the sensitivity test indicated that the s-c-s-c
plate typically responded less to acoustic excitation than

the clamped plate. This is an indication that acoustic contamination is still a major contributor to the total response of the plate.

4.3.5--Plate Low Wavenumber Response. The peaks of the modal response shown in Figure 4.11 for the Martin plate and Figures 4.12 and 4.13 for the Jameson plate are assumed to be low wavenumber data points. The spectrums were measured at analyzer bandwidth greater than the plate modal bandwidth. Corrections were performed on the peak values to account for the difference in bandwidths. Data was obtained at various analyzer bandwidths to evaluate the correction method. Spectral levels for various analyzer bandwidths after correction generally differ by less than 2 dB.

No corrections was made to the low wavenumber data to account for acoustic or convective contamination. However, only those modes thought to have good modal separation were used.

V. LOW WAVENUMBER RESULTS

5.1 Microphone Low Wavenumber Results

5.1.1--Method of Calculating Low Wavenumbers. The array output at any frequency, as shown in Equation (2.15) represents an integration over wavenumber space of the array response and the spectral density. If the spectral density is assumed to be independent of $\underline{k}$ for the frequencies of interest (2), then from Equation (2.15)

$$\Phi_M(\omega) \cong \Phi(\underline{k},\omega)_L \int\limits_{-\infty}^{+\infty}\int |W(\underline{k})|^2 \, d\underline{k} \tag{5.1}$$

Blake and Chase [2] performed an integration on a four microphone array with uniform shading to obtain an estimate for

$$\int\limits_{-\infty}^{+\infty}\int |W(\underline{k})|^2 \, dk = 37 \text{ in}^{-2} \tag{5.2}$$

The assumption used in obtaining Equation (5.1) is the main contribution to the array output comes from the major response lobe. Since the six element array is similar to that of Blake and Chase [2], Equation (5.2) can be used by modifying it to account for the difference in bandwidth of the main response lobe. The modified version of Equation (5.2) is then

$$\int \int |W(\underline{k})|^2 d\underline{k} = \left(\frac{37.0}{B}\right)\left(\frac{4}{N}\right) \text{ in}^{-2} \tag{5.3}$$

where   B = 1.0 for Uniform shading,

             = 1.53 for Chebyshev shading,

             = 2.0 for Binomial shading,

         N = the number of microphones;

B was estimated by comparing the main lobe width in the
acoustical calibration for various shadings.

Then substituting Equation (5.3) into Equation (5.1)
and solving for $\Phi(\underline{k},\omega)_L$

$$\Phi(\underline{k},\omega)_L = \frac{\Phi_m(\omega)BN}{(4)(37)} \qquad (5.4)$$

The values for $\Phi_m(\omega)$ are selected as discussed in
Section 4.2.4.

5.1.2--Alternating Phased Results. The measured
levels for the spectral density in the low wavenumber region
are presented in nondimensional form. The first non-
dimensional form presented is for the ordinate
$\Phi(\underline{k},\omega)_L U_\infty/q^2\delta^{*3}$ and the abscissa is the Strouhal number
$S=\omega\delta^*/U_\infty$. This is the same nondimensional form used by
Farabee and Geib [3] and Martin [5].

Figure 5.1 shows the results for the alternating phased
uniform shaded array in position 1 (see Section 3.2.1)
located 1.34 m downstream from the contraction exit plane.
The plot shows the results at various speeds. Two points
were measured, each corresponding to the nulls in the acoustic
response. The important thing to notice is how the data tends

to curve upward at the higher speeds, especially for the
low frequency data points where the convective ridge
encroaches the first null region. The second point to notice
is that the data from the first null region (i.e., of the two
data points obtained for a particular speed, the one with the
lower Strouhal number) has a different slope than the data
from the second null region. Remember the data from the
second null lies strictly in the acoustic region while the
data from the first null lies in the transition region (see
Sections 4.2.2 and 4.2.3).

Figure 5.2 shows a comparison between the data measured
at position 1 and the data measured at position 2 for the
alternating phased uniformly shaded array. The main
difference between the two locations is the boundary layer
displacement thickness. The average displacement thickness
at position 1 is 0.21 inches, while the average displacement
thickness for position 2 is 0.09 inches. As shown on the
figure, the nondimensional form used, having a strong
dependence on boundary layer thickness, does not collapse the
two different sets of data. The two sets of data do have
parallel slope indicating (as will be shown in Section 5.3) a
weak dependence on displacement thickness as a length scale.

Figure 5.3 shows a comparison between the data for the
three different shadings for the alternating phased array
measured at position 1. Both the Chebyshev shading and the
binomial shading produces slightly lower results than the
uniform shading.

Table 5.1 tabulates the raw data for all the various cases measured using the alternate phased array.

5.1.3--Common Phased Array. Figure 5.4 shows a comparison between the common phased array data and the alternating phased array data at position 1. The alternating phased array typically gave lower results than the common phased array.

Table 5.2 tabulates the raw data for all the various cases measured using the common phased array.

5.2 Plate Low Wavenumber Results

5.2.1--Method of Calculating Low Wavenumber. If the excitation $\Phi_p(k,\omega)$ is reasonably constant in the low wavenumber region, the integral of Equation (2.31) will be dominated by contributions from the major lobes of the wavenumber filter shapes, $|A(k_1)|^2$ and $|A_n(k_3)|^2$. The major lobes of the mode shapes $|A_m(k_1)|^2$ and $|A_n(k_3)|^2$ are located at the characteristic wavenumbers k_m and k_n respectively. For the plates used, the wavenumber bandwidths are sufficiently narrow to allow the filter shapes to be approximated by Dirac delta functions at $k_1 = \pm k_m$ and $k_3 = \pm k_n$. Since

$$\int_{-\infty}^{+\infty} |A(k)|^2 dk = 2\Pi ,$$

the approximations are

$$|A_m(k_1)|^2 = \pi[\delta(k_1-k_m) + \delta(k_1+k_m)]$$

$$|A_n(k_3)|^2 = \pi[\delta(k_3-k_n) + \delta(k_3+k_n)] \tag{5.5}$$

The substitution of Equations (5.5) into Equation (2.31) yields

$$S_w(x,z,\omega_{mn}) = \frac{2\pi^2 f_{mn}(x,z)}{(\sigma\eta\omega^2)^2_{mn}} [\Phi_p(k_m,k_n,\omega_{mn}) + \Phi_p(-k_m,k_n,\omega_{mn})]$$

$$\tag{5.6}$$

It was assumed when computing Equation (5.6), that because of symmetry in the lateral dimension

$$\Phi_p(\underline{+}k_m,k_n,\omega_{mn}) = \Phi_p(\underline{+}k_m,-k_n,\omega_{mn}) \tag{5.7}$$

For the plate experiments, it is the acceleration response which is measured. Since $S_a(x,z,\omega_{mn}) = \omega_{mn}^4 S_w$
$S_a(x,z,\omega_{mn}) = \omega_{mn}^4 S_w(x,z,\omega_{mn})$, the acceleration spectral density at resonance is given by

$$S_a(x,z,\omega_{mn}) = \frac{2\pi^2 f_{mn}^2(x,z)}{(\sigma\eta)^2_{mn}} [\Phi_p(k_m,0,\omega_{mn}) + \Phi_p(-k_m,0,\omega_{mn}]$$

$$\tag{5.8}$$

Equation (5.6) and (5.8) provide the basis for the experimental measurements of $\Phi_p(\underline{k},\omega)$ in the low wavenumber region. Once the plate has been calibrated by determining

its physical parameters and resonance characteristics, it
is possible to determine the level of the excitation
$\Phi_p(\underline{k}, \omega)$ from displacements or acceleration measurements. As
the equation indicates, there is no way to separate the
component of excitation at $k_1 = k_m$ from that at $k_1 = -k_m$. To
be consistent with Martin [5], both terms will be retained
by defining

$$P(k_1, k_3, \omega) = \Phi_p(k_1, k_3, \omega) + \Phi_p(-k_1, k_3, \omega) \tag{5.9}$$

Substituting Equation (5.9) into Equation (5.8) and solving
for $P(k_m, k_n, \omega)$ yields

$$P(k_m, k_n, \omega) = \frac{(\sigma\eta)_{mn}^2}{2\pi^2 f_{mn}^2(x,z)} S_a(x, z, \omega_{mn}) \tag{5.10}$$

In all experiments the response was measured at the
anti-node of a particular mode. From analytical mode
shapes [5], it was found that at the anti-node

$$f_{mn}^2(x,z) \cong \frac{5.044}{L_1 L_3} \qquad \text{for} \quad \begin{matrix} n = 1 \\ m \geq 3 \end{matrix} \text{ or } \begin{matrix} n \geq 3 \\ m = 1 \end{matrix}$$

$$\cong \frac{4.554}{L_1 L_3} \qquad \text{for} \quad \begin{matrix} n = 2 \\ m \geq 3 \end{matrix} \text{ or } \begin{matrix} n \geq 3 \\ m = 2 \end{matrix}$$

$$\cong \frac{4}{L_1 L_3} \qquad \text{for} \quad \begin{matrix} n \geq 3 \\ m \geq 3 \end{matrix} \tag{5.11}$$

5.2.2--Martin Plate Results.   Figure 5.5 shows the
results of the Martin plate located in position 1 for
various speeds.   Again there is a slight upturn of the data
at the higher speeds, although not as pronounced as the
microphone data.   The plate data is thought to be more
convectively contaminated at the higher speeds and more
acoustically contaminated at the lower speeds.

Figure 5.6 shows a comparison between the data measured
at position 1a nd the data measured at position 2.   Again
the non-dimensional form does not collapse the data very well.

Table 5.3 tabulates the raw data for all the various cases
measured using the Martin plate.

5.2.3--Jameson Plate Results.   Figure 5.7 shows the
results of the Jameson plate at position 1 for various
speeds.   The Jameson plate data is slightly lower than the
Martin plate data but still within each plate's scatter.   One
possible reason for the slightly lower results of the Jameson
plate is additional rejection of acoustic contamination by
the higher order lateral modes.   The (3,3), (5.3) etc. modes
have corner mode [19] canacellation while the (1,5), (1,7),
etc. modes have only edge mode cancellation.

Table 5.4 tabulates the raw data for all the various
cases measured using the Jameson plate.

5.3 Effect of Boundary Layer Thickness on Low Wavenumber Results

As indicated in Figures 5.2 and 5.6, the use of boundary layer thickness as a length scale does not collapse the data very well. Comparing the raw data at the two positions in Table 5.1 and 5.3, one notices that the data does not vary significantly from one position to another. From this it was decided that a length scale that does not vary from position to position would be more suitable.

As an initial trial, an arbitrary constant length scale was chosen. The length scale chosen was 0.2 inches (the average boundary layer thickness measured by Martin [5]. Figures 5.8 and 5.9 repeat the data of Figures 5.2 and 5.6 with a constant length scale. A much better collapse of the data occurs.

This indicates that the data measured in the M.I.T. Wind Tunnel does not have a strong dependence on boundary layer thickness.

5.4 A Look at Other Normalization

To get a better collapse of the data, two other normalizations have been tried. The one is normalized on the inner variable V_*, the friction velocity, where the ordinate is $\Phi(\underline{k},\omega)_L \omega^3/\rho^2 V_*^6$ and the abscissa is the Strouhal number $S = \dfrac{\omega\nu}{V_*^2}$. A plot of the microphone results for the two positions is shown in Figure 5.10. The collapse of the data is still not good.

The other normalization was on flow parameters, where the ordinate is $\Phi(\underline{k},\omega)_L/\rho^2\nu^3$ and the abscissa is $\omega\nu/U_\infty^2$. A plot of the microphone data is shown in Figure 5.11 and a plot of the Martin plate data is shown in Figure 5.12. This seems to result in a much better collapse of the data.

5.5 Comparison with Other Investigators

5.5.1--Martin Plate. A plot of the Martin plate results measured at position 1 with $\delta^*=0.2$ inches is shown in Figure 5.13. On that figure is a curve representing a least square fit of the data measured by Martin [5] in 1976. Also on the plot is a curve representing a least square fit of the data measured by Jameson [8] in 1975.

The present Martin plate data lies 2-3 dB below what Martin measured in 1976. This is primarily due to Wall Jet Configuration allowing the acoustic cross modes to be absorbed by the anechoic treatment in the chamber. However, the results are still more than 10 dB above Jameson's 1975 data.

5.5.2--Jameson Plate. A plot of the Jameson plate results measured at position 1 with nominal $\delta^*=0.2$ inches is shown on Figure 5.14. The Martin 1976 data and the Jameson 1975 data is also indicated on this figure. In addition, the Jameson 1975 data was also adjusted for a nominal $\delta^*=0.2$ inches instead of actual $\delta^*=0.139$ inches and is indicated on the plot as a dotted line.

As the plot indicates, without compensating for the difference in δ^*, Jameson's 1975 data is typically 12-13 dB below the present data. When the contribution from the

difference in δ^* is removed the present data is still 10dB higher.

In Section 3.4 a comparison was made between the MIT facility and the BBN facility. If it is assumed that the high frequency response of a 1" flush mounted microphone is indicative of the acoustic contamination (argument for this assumption has been given previously and is repeated in the conclusion), then the BBN facility seems to be approximately 3 dB quieter than the M.I.T. facility according to Figures 3.15 and 3.16. With the above compensations, the present data is approximately 7-8 dB higher than Jameson's 1975 data.

Jameson [8] used a 2 gram accelerometer to make his measurement while the present data was measured using a .5 gram accelerometer. Jameson [8] corrected this data for the mass of his accelerometer, but used an infinite plate model which assumes modal overlap conditions. The actual data was measured at modes where modal overlap did not exist. Tests were performed on the Jameson plate comparing response of the 2 gram accelerometer used by Jameson and the 1/2 gram accelerometer presently used. The test indicated that the 2 gram accelerometer would have a 2-4 dB effect on the results while the infinite plate model would only predict errors on the order of 1/2 dB.

Accounting for all the above, the present data at best is still 5-6 dB above Jameson's 1975 data. This would allow the results to be within each other's scatter.

5.5.3--<u>Microphone Array</u>. A plot of the alternating phased microphone array results measured at position 1 with δ^*=0.2 inches is shown on Figure 5.15. The Martin 1976 data and the Jameson 1976 data is also indicated on this figure. In addition, the Farabee and Geib [3] 1976 data is shown on the plot adjusted for a nominal δ^*=0.2 inches instead of the average actual δ^*=0.5 inches measured by Farabee and Geib.

Farabee and Geib also indicated two different slopes in their data as was discussed in Section 5.1.2. The lower speed data had a slope of S^{-4} and the higher speed data, which is thought to be more convectively contaminated has a slope of S^{-5}.

If the present microphone data which is thought to be possibly convectively contaminated is ignored, the remaining data lies in the same vicinity and has close to the same slope as the plate data. The adjusted Farabee and Geib 1976 S^{-4} data also lies in this region, and the Martin 1976 data, which possibly responded to more acoustic contamination by 2-3 dB (see Section 5.5.1), also lies in this region. The Jameson 1975 data is still well below this region as was discussed in Section 5.5.2.

VI. CONCLUSIONS

6.1 Conclusion of Acoustic Contamination

A. The data from the 1" flushed mounted microphone
at frequencies higher than the convective ridge
roll-off is almost entirely acoustic contamina-
tion because

i) The phase relation between two microphones
(see Figures 3.10 and 3.13) show a linear
phase delay at the higher frequencies with
a slope of opposite direction than the
linear phase delay due to the convective
velocities occurring at the lower frequen-
cies. This indicates that the acoustic
contamination is coming from downstream.
The velocity calculated from the linear
phased delay was approximately the speed
of sound. When the phase delay was compared
to the phase delay of an acoustic source
without flow (see Figure 4.5), except for
a difference in direction, they were
almost exactly the same.

ii) The alternating phased array response to
flow (see Figure 4.1) at the frequency
coincident with the sonic line main lobe
response asymptotes to the single micro-
phone response.

iii) The coherence of the alternating array and
single microphone in the array during flow
(see Figure 4.3) is nearly zero at the loca-
tions of the sonic region nulls in the array.

B. Acoustic contamination during flow is mostly
plane wave due to the semianechoic treatment
in the tunnel and its better utilization in the
wall jet configuration. This is substantiated
by the linear phased delay discussed in Item A.

C. The acoustic contamination during flow is very
directive. The arguments discussed in Item A
indicate that the high frequencies measurements
of the flushed mounted 1 inch microphone is
mostly acoustic. When compared to the block-
house microphone in Figure 3.14, there are
substantial differences. This comparison agrees
with the qualitative argument concerning
directivity given in Section 4.3.4.

D. If the high frequency response of the flush
mounted 1" microphone is more indicative of the
acoustic contamination during flow than the
blockhouse microphone as argued above, then the
BBN wind tunnel is perhaps 3 dB quieter (at
least at the higher frequencies) than the M.I.T.

wind tunnel (see Figures 3.15 and 3.16).

E. The plates are responding very strongly to acoustic contamination. The acoustic response test, although not conclusive, indicated the response to acoustic contamination was nearly as great as the measured levels, especially at the lower speeds. When attempts to reduce acoustic contamination were made, such as using the wall jet test configuration, reduction in overall levels were observed. This indicated that acoustic contamination contributed to the results.

6.2 Conclusion on Convective Contamination

A. The results of the microphone array becomes convectively contaminated at the higher speeds and lower frequencies. This follows from

i) The rejection of the convective contamination is due mostly to the low pass wavenumber filtering effect of the single 1" microphone. The phase relation between two microphones (see Figures 3.10 and 3.13) distinctly show the region where the microphones are responding to the convective contamination. As the free stream velocity increases, this region extends to the frequency where low wavenumber data is measured.

ii)   Figure 5.1 distinctly shows an increasing

negative slope for the higher speed, low

frequency, low wavenumber data points. This

corresponds to the convective ridge shifting

to higher frequencies with higher speeds.

B.   Martin [5] and Jameson [8] indicated increasing

convective contamination with increasing speed,

but this was not significant until 50 m/s.

6.3   Conclusions on Low Wavenumber Data

A.   With the exception of the microphone array where

the high speed data is obviously convectively

contaminated, the Martin plate, the Jameson

plate, and the microphone array all result in the

same low wavenumber measurements. They typically

lie 2-3 dB below a least "square fit" of Martin's

[5] 1976 data with a significant amount of

scatter.

B.   The scatter is believed to be due to different

amounts of acoustic and convective contamination

measured by each filter. Each mode of each plate

has a slightly different wavenumber-frequency

response characteristic and the various shadings

of the microphone produces different wavenumber-

frequency response characteristics. The con-

tamination varies with wavenumber, frequency, and

speed. All of this contributes to spreading the data.

C. Measurements were made at two locations with substantially different boundary layer displacement thickness, $\delta*$ = 0.09 and 0.21 inches. The measured data showed little difference between location indicate a weak $\delta*$ dependence.

D. The Farabee and Geib [3] 1976 microphone data when adjusted to a nominal $\delta*$ = 0.2 inches (Farabee's and Geib's actual average $\delta*$ = 0.5 inches), lay in the same region as the current data.

E. Arguments were made in Section 5.5.2, reducing the difference between Jameson's [8] 1975 data and the current data from 12-13 dB difference to 5-6 dB difference. This would bring the two results to within each other's scatter. The arguments for reducing the scatter were adjustment for difference in $\delta*$ (Jameson's average $\delta*$ = 0.139 inches), differences in acoustic contaminations, and a more accurate adjustment due to mass of the accelerometer. The remaining 5-6 dB difference could not be explained quantitatively. Possible differences could be differences in wavenumber-frequency response of

the current Jameson plate and the one used in
1975, inaccurate estimation of facility acoustic
contamination, technical differences between the
two experimental programs, or facility dependent
low wavenumber excitation.

F. Based on the arguments of Sections 6.1 and 6.2,
    it cannot be certified that a true measure of
    the low wavenumber levels has been made. Because
    of convective contamination, the best data is
    obtained at the lower speed. However at the
    lower speeds, the low wavenumber levels are also
    reduced and acoustic contamination or equipment
    sensitivity becomes a problem.

References

[1]   Maidanik, G. and D.W. Jorgenson, "Boundary Wave
       Vector Filters for the Study of Pressure Fields
       in a Turbulent Boundary Layer," JASA, 42, pp.
       494-501 (1967).

[2]   Blake, W.K. and D.M. Chase, "Wavenumber-Frequency
       Spectra of Turbulent Boundary Layer Pressure
       Measured by Microphone Arrays," JASA, 49, pp.
       862-867 (1971).

[3]   Farabee, T.M. and F.E. Geib, Jr., "Measurements of
       Boundary Layer Pressure Fields with an Array of
       Pressure Transducers in a Subsonic Flow," NSRDC
       Report 76-0031 (1976).

[4]   Aupperle, F.A. and R.F. Lambert, "On the Utilization
       of a Flexible Beam as a Spatial Filter," JS&V,
       24, pp. 259-267 (1972).

[5]   Martin, N.C., "Wavenumber Filtering by Mechanical
       Structures," M.I.T. Ph.D. Thesis (January 1976).

[6]   Moeller, M.J., N.C. Martin and P. Leehey, "Low
       Wavenumber Levels of a Turbulent Boundary Layer
       Wall Pressure Fluctuations in Zero and Adverse
       Gradients," M.I.T. Acoustics & Vibration Lab.
       Report 82464-2 (1978).

[7]   Jameson, P.W., "Measurements of the Low Wavenumber
       Component of Turbulent Boundary Layer Wall Pressure
       Spectrum," Bolt, Beranek & Newman Report #1937
       (1970).

[8]   Jameson, P.W., "Measurement of Low Wavenumber Component
       of Turbulent Boundary Layer Pressure Spectral
       Density," 4th Symposium on Turbulence in Liquids,
       University of Missouri-Rolla, September 1975.

[9]   Bruel, P.V. and G. Rasmussen, "Bruel & Kjaer Technical
       Review," No. 2 (1959).

[10]   Chase, D.M., "Turbulent Boundary Layer Pressure Fluc-
       tuations and Wavenumber Filtering by Non-uniform
       Spatial Averaging," JASA, 46, pp. 1350-1356 (1969).

References (cont'd)

[11] Dolph, C.L., "A Current Distribution for Broadside Arrays which Optimize the Relationship between Beam Width and Side-Lobe Level," Proceedings of the Institute of Radio Engineers, 34, pp. 335-348 (1948).

[12] Martin, N.C. and P. Leehey, "Low Wavenumber Wall Pressure Measurements Using a Rectangular Membrane as a Spatial Filter," JASA, 52, pp. 95-120 (1977).

[13] Hanson, C.E., "The Design and Construction of a Low-Noise, Low-Turbulence Wind Tunnel," M.I.T. Acoustics & Vibration Lab. Report 79611-1 (1967).

[14] White, R.M., Viscous Fluid Flow, McGraw-Hill, 1974, 480p.

[15] Burton, T.E., "Wall Pressure Fluctuation at Smooth and Rough Surfaces under Turbulent Boundary Layers with Favorable and Adverse Pressure Gradients," M.I.T. Acoustics & Vibration Lab. Report 70208-9 (1973).

[16] Blake, W.K., "Turbulent Boundary Layer Wall Pressure Fluctuations on Smooth and Rough Walls," M.I.T. Acoustics & Vibration Lab. Report 70208-1 (1969).

[17] Blake, W.K., "Turbulent Boundary Layer Wall Pressure Fluctuation on Smooth and Rough Walls," JFM, 44, pp. 637-660 (1970).

[18] Kinsler, L.E. and A.R. Frey, Fundamentals of Acoustics, John Wiley & Sons, Inc., 1962.

[19] Smith, P.W. and R.H. Lyon, "Sound and Structural Vibration," NASA publication CR-160.

MODE (m,n)	1976 DATA Frequency	Loss Factor	1983 DATA Frequency	Loss Factor
3,1	805	.023	792	.026
5,1	910	.0082	914	.0073
7,1	1070	.0089	1078	.0051
9,1	1290	.0031	1304	.0029
11,1	1585	.0049	1606	.0038
13,1	1960	.0019	1979	.0017
15,1	2405	.0017	2425	.0018
17,1	2920	.0018	2938	.0017
19,1	3500	.0019	3519	.0016
21,1	4150	.0014	4166	.0014

TABLE 2.1   Comparison of Experimentally Determined Characteristics of Martin's CCCC Plate

MODE (m,n)	1975 DATA Frequency	1983 DATA Frequency	Loss Factor
3,2	487	376	.0030
5,2	830	695	.0023
5,3	---	918	.0010
3,4	---	948	.0017
7,1	1205	1017	.0021
7,2	1336	1167	.0012
1,5	---	1204	.0035
3,5	---	1358	.0019
7,3	1612	1403	.0016

TABLE 2.2   Comparison of Experimentally Determined Characteristic of Jameson Plate

Flow Velocity	Position #1				Position #2			
	δ^*	θ	H	V_*	δ^*	θ	H	V_*
	(In.)	(In.)	(M/S)	(M/S)	(In.)	(In.)	(M/S)	(M/S)
15 M/S	0.079	0.058	1.36	0.67	0.215	0.161	1.33	0.55
20 M/S	0.082	0.060	1.37	0.83	0.205	0.153	1.34	0.70
25 M/S	0.087	0.064	1.36	1.04	0.213	0.154	1.33	0.90
30 M/S	0.090	0.067	1.34	1.22	0.213	0.160	1.33	1.09
35 M/S	0.094	0.070	1.34	1.35	0.216	0.164	1.31	1.28
40 M/S	0.096	0.072	1.33	1.54	0.211	0.160	1.32	1.47

TABLE 3.1 Boundary Layer Flow Properties

MODE	Sensitivities for Speaker @ Inlet to Diffuse/(dB)	Sensitivities for Speaker @ Inlet to Tunnel (dB)
3,1	31.4	24.7
5,1	33.2	20.6
7,1	22.5	16.6
9,1	25.5	24.5
11,1	36.2	27.8
13,1	25.8	25.3
15,1	29.3	21.0
17,1	34.8	34.2
19,1	32.2	32.5
21,1	36.5	34.7

$$\text{Sensitivity} = 20 \text{ Log } \left(\frac{\text{Accelerometer Value}}{\text{Microphone Value}}\right)$$

TABLE 4.1 Comparison of Acoustic Sensitivity Test on Martin Plate with Speakers at Two Different Locations

Alternating Array Measurements @ Position 1

Speed (M/S)	Shading	Frequency (Hz)	Measured Level (dB)
15	Uniform	2150	- 95.9
15	Uniform	4200	-103.7
20	Uniform	2150	- 84.1
20	Uniform	4200	- 95.0
25	Uniform	2150	- 72.8
25	Uniform	4200	- 88.7
30	Uniform	2150	- 68.2
30	Uniform	4200	- 83.4
35	Uniform	2150	- 62.7
35	Uniform	4200	- 78.9
40	Uniform	2150	- 53.9
40	Uniform	4200	- 72.2
15	Chebychev	1950	- 93.7
15	Chebychev	3550	-106.0
20	Chebychev	1950	- 80.1
20	Chebychev	3550	- 96.2
25	Chebychev	1950	- 70.9
25	Chebychev	3550	- 87.8
15	Binomial	2000	- 93.6
15	Binomial	2400	- 98.8
20	Binomial	2000	- 79.0
20	Binomial	2400	- 86.4

TABLE 5.1 Measured Alternating Array Spectral Levels
All Levels Are dB re 1 Pa and Hz

Alternating Array Measurements @ Position 2

Speed	Shading	Frequency (Hz)	Measured Level (dB)
15	Uniform	2350	- 96.0
15	Uniform	4200	-103.0
20	Uniform	2400	- 82.9
20	Uniform	4100	- 92.1
25	Uniform	2100	- 70.5
25	Uniform	4100	- 86.1
30	Uniform	2350	- 67.7
30	Uniform	4100	- 81.4
35	Uniform	2350	- 62.2
35	Uniform	4100	- 75.1
40	Uniform	2350	- 58.9
40	Uniform	4100	- 69.3
15	Chebychev	1950	- 88.3
15	Chebychev	3550	-102.9
20	Chebychev	1675	- 72.0
20	Chebychev	3100	- 89.2
25	Chebychev	2000	- 69.1
25	Chebychev	3450	- 84.7
15	Binomial	2300	- 93.2

TABLE 5.1 (cont.)   Measured Alternating Array Spectral Levels
All Levels Are dB re 1 Pa and Hz

Common Array Measurements @ Position 1

Speed	Shading	Frequency (Hz)	Measured Levels (dB)
15	Uniform	2400	- 97.6
15	Uniform	4200	-103.3
20	Uniform	2400	- 86.3
20	Uniform	4200	- 94.2
25	Uniform	2400	- 77.0
25	Uniform	4200	- 86.8
30	Uniform	2400	- 68.1
30	Uniform	4200	- 81.7
35	Uniform	2400	- 62.6
35	Uniform	4200	- 77.0
40	Uniform	2400	- 57.2
40	Uniform	4200	- 72.8
15	Chebychev	2400	- 99.3
15	Chebychev	4200	-107.4
20	Chebychev	2400	- 86.4
20	Chebychev	4200	- 93.4
25	Chebychev	2400	- 76.8
25	Chebychev	4200	- 88.0
15	Binomial	2400	- 94.7
15	Binomial	4200	-106.3
20	Binomial	2400	- 83.8
20	Binomial	4200	- 95.5
25	Binomial	2400	- 74.2
25	Binomial	4200	- 86.4

TABLE 5.2   Measured Common Array Spectral Levels
All Levels Are dB re 1 Pa and Hz

Martin Plate Acceleration Response @ Position 1

MODE	15 M/S	20 M/S	25 M/S	30 M/S	35 M/S	40 M/S
7,1	-58.2	-49.2	-41.6	-36.2	-31.5	-26.8
9,1	-61.4	-52.7	-43.4	-35.8	-30.4	-21.9
11,1	-63.4	-55.7	-48.4	-42.3	-37.2	-29.7
13,1	-59.4	-49.1	-40.1	-34.7	-29.4	-25.2
15,1	-63.9	-60.1	-51.3	-43.8	-37.3	-32.5
17,1	-60.0	-54.3	-49.8	-45.7	-41.3	-37.3

Martin Plate Acceleration Response @ Position 2

MODE	15 M/S	20 M/S	25 M/S	30 M/S	35 M/S	40 M/S
7,1	-57.5	-50.8	-43.7	-38.7	-32.6	-26.9
9,1	-58.2	-50.2	-41.6	-34.7	-27.5	-21.9
11,1	-58.5	-48.1	-41.7	-37.5	-33.1	-29.1
13,1	-56.4	-45.2	-39.2	-32.8	-28.1	-21.6
15,1	-62.1	-55.8	-50.0	-44.3	-37.0	-32.2
17,1	-62.4	-54.4	-48.0	-42.5	-37.9	-33.5

TABLE 5.3   Measured Martin Plate Spectral Levels
All Levels Are dB re 1 M/S^2 and Hz

Jameson Plate Acceleration Response @ Position 1

MODE	20 M/S	25 M/S	30 M/S	35 M/S	40 M/S
5,2	-46.0	-39.0	-31.4	-25.0	-18.4
5,3	-45.1	-40.7	-33.9	-27.5	-21.8
3,4	-48.5	-44.9	-38.8	-33.0	-28.2
7,1	-49.8	-45.5	-39.0	-32.2	-24.9
7,2	-49.5	-43.4	-38.4	-30.5	-25.4
1,5	-54.5	-48.4	-44.8	-40.6	-35.6
3,5	-52.2	-46.8	-40.9	-34.1	-29.8
7,3	-52.3	-47.5	-42.0	-35.9	-29.1

TABLE 5.4   Measured Jameson Plate Spectral Levels
All Levels Are dB re 1 M/S^2 and Hz
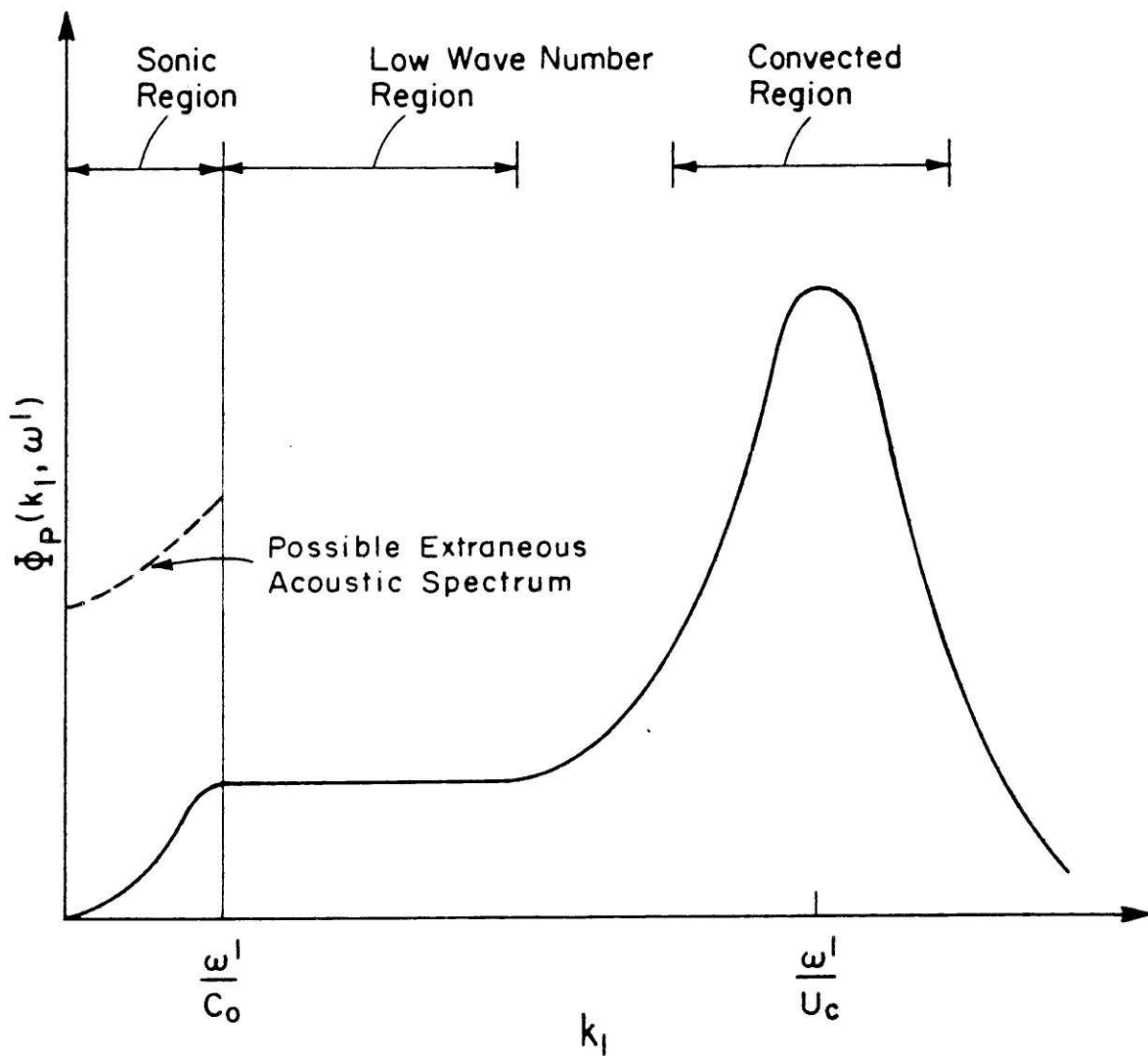
FIGURE 2.1   Schematic of the Variation of Magnitude of the
Wavenumber Frequency Spectrum at a Particular
Frequency, ω'.
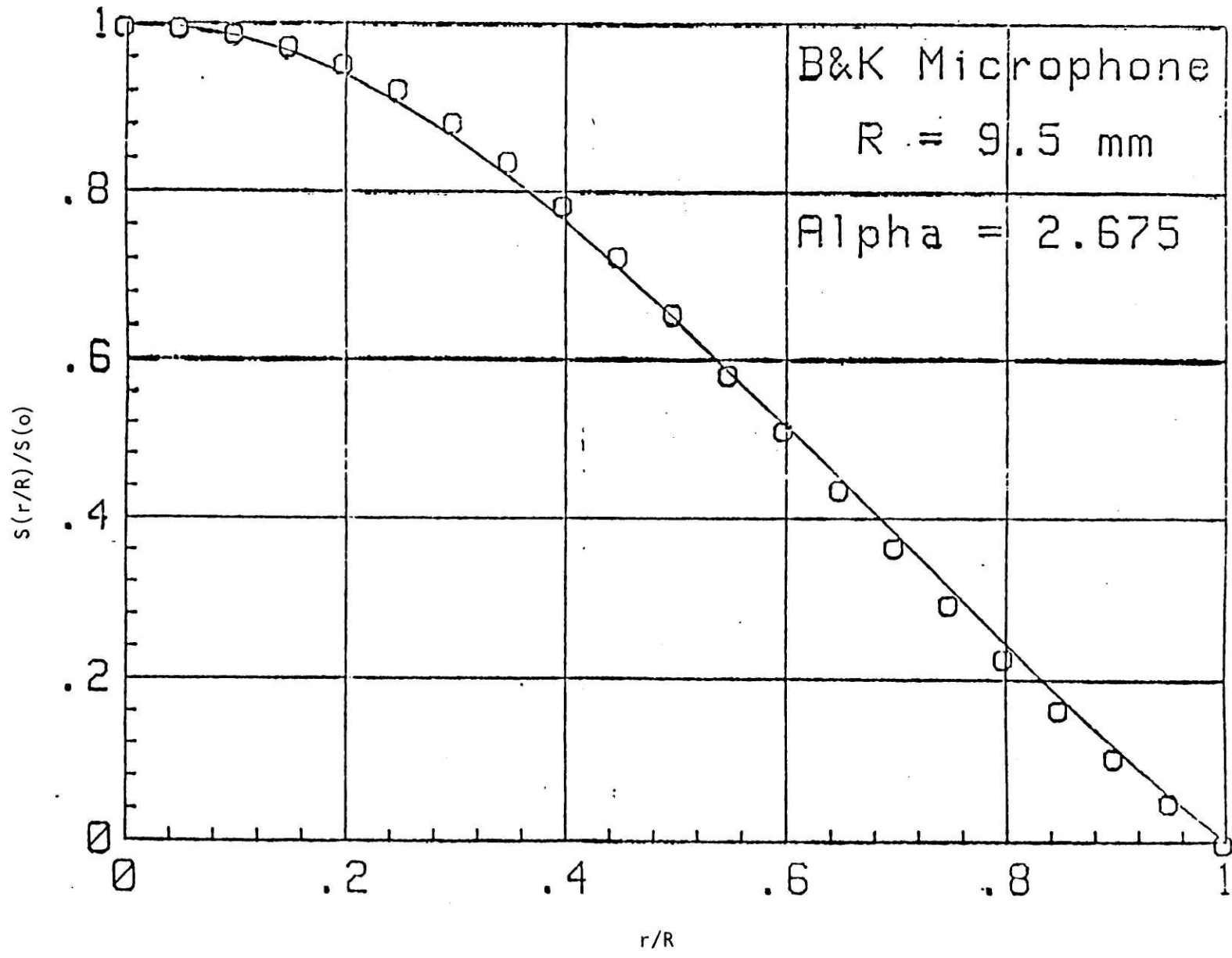
Figure 2.2. Microphone Spatial Sensitivity.
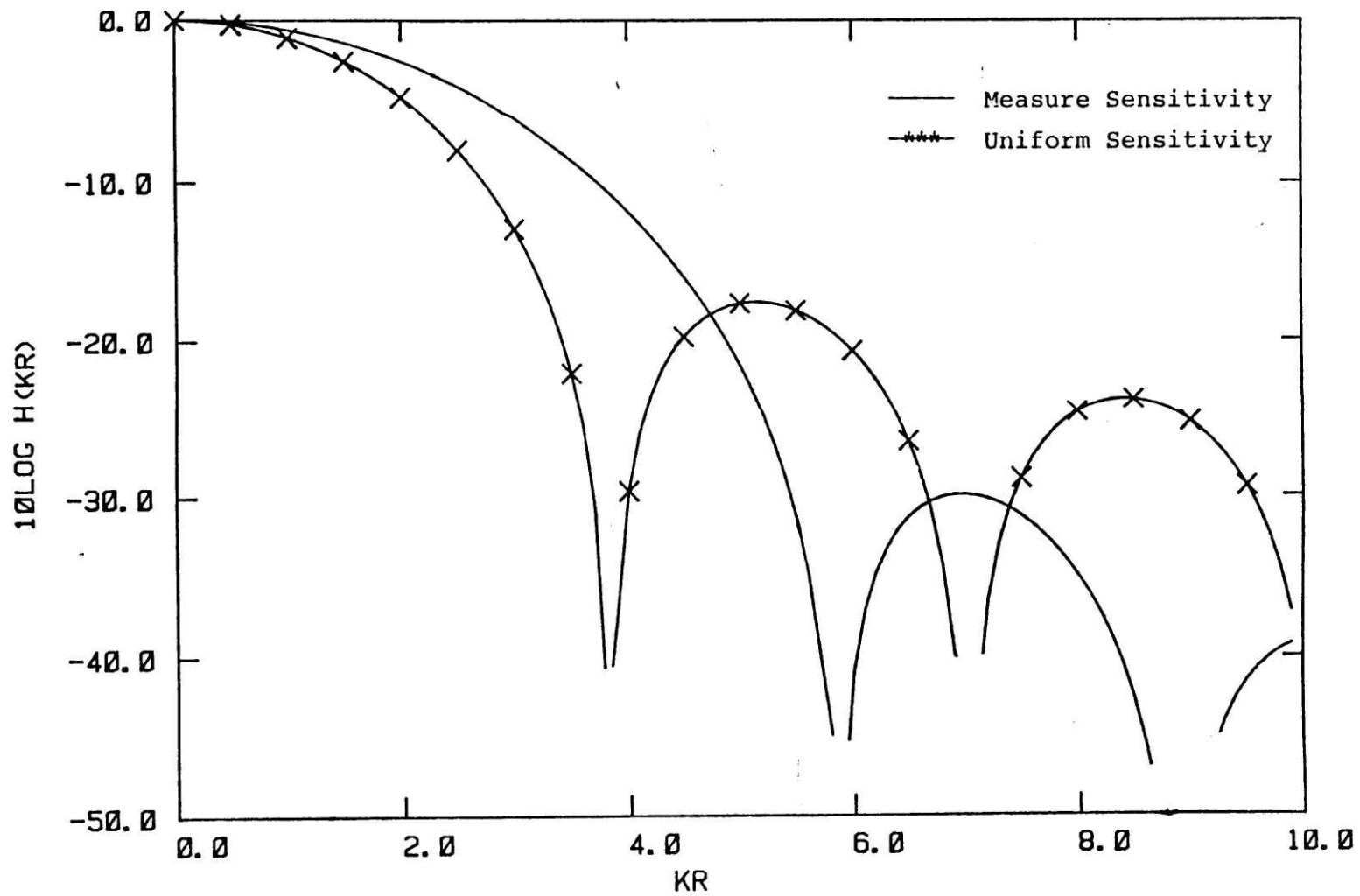
FIGURE 2.3 Single Microphone Wavenumber Response.
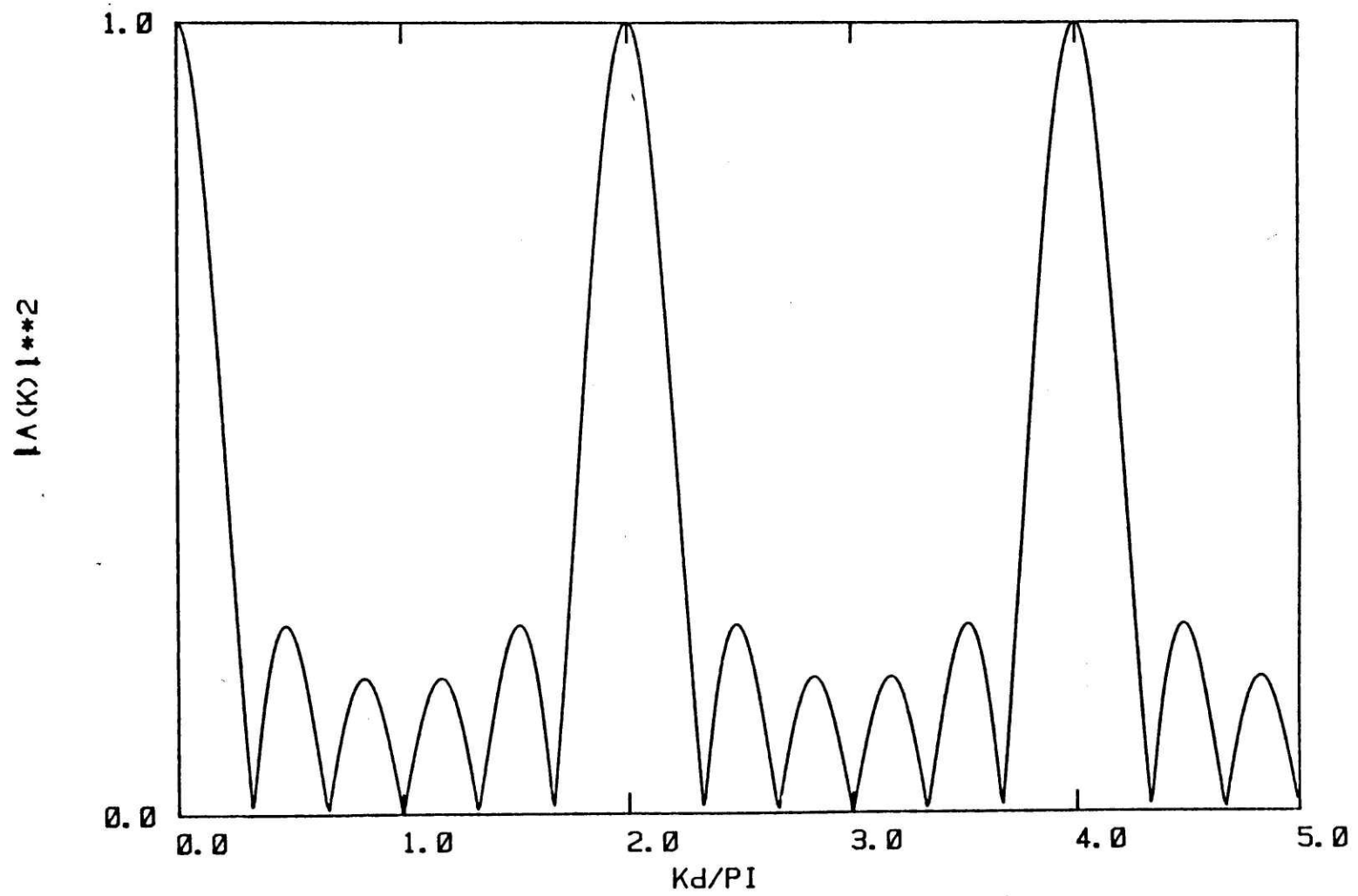
FIGURE 2.4   Common Phase Array Wavenumber Response.
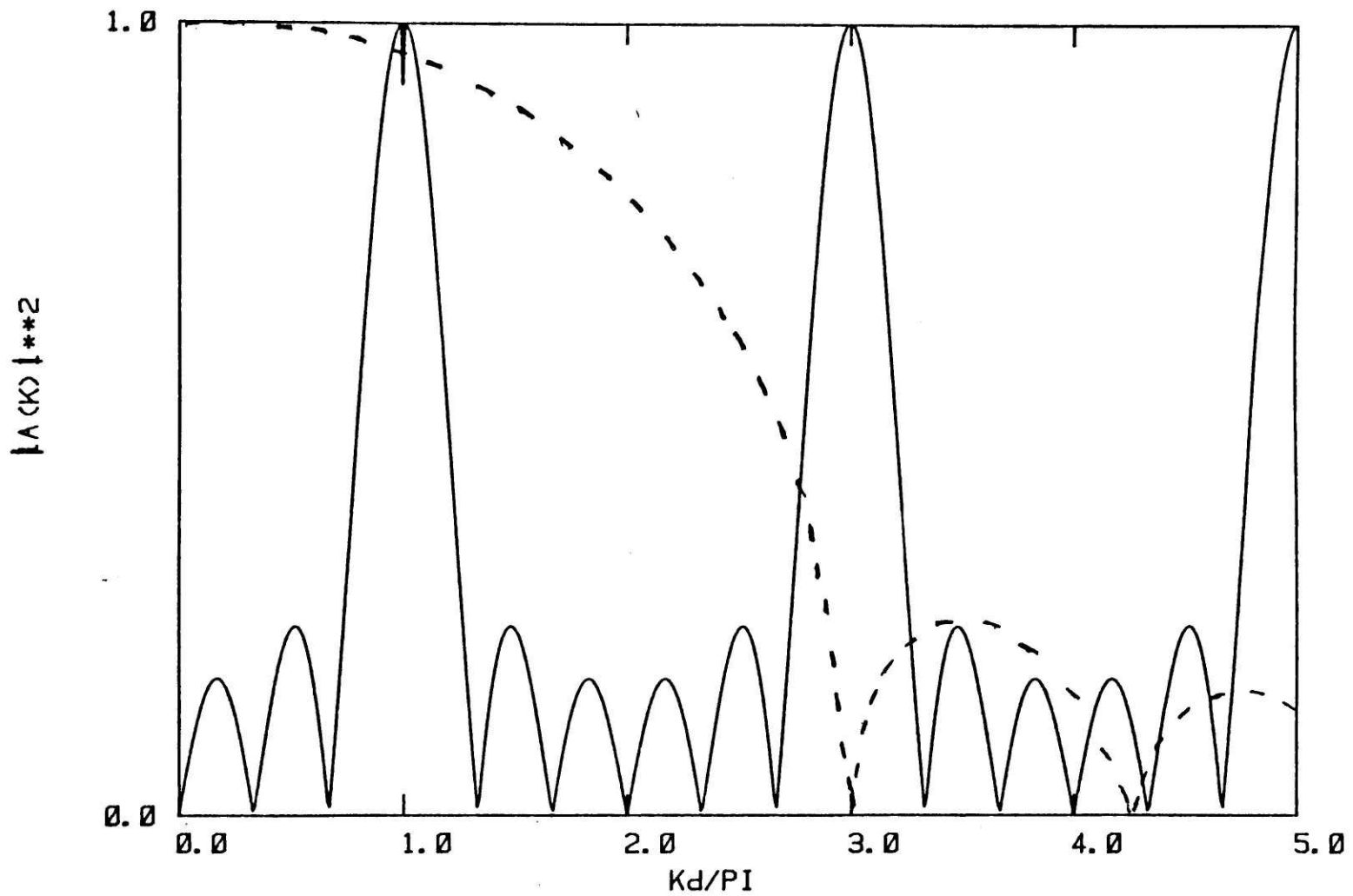
FIGURE 2.5   Alternating Phase Array Response With Single Microphone
Response for d/R = 2.19.

variable gain,
set by potentiometer

G_1 +

G_2 +
+

Σ

COMMON
PHASING

G_3 +
+

G_4 +
−

G_5 +
−

Σ

ALTERNATE
PHASING

G_6 +

inputs switch selectable, input or ground
for array sizes of 6, 5, or 4
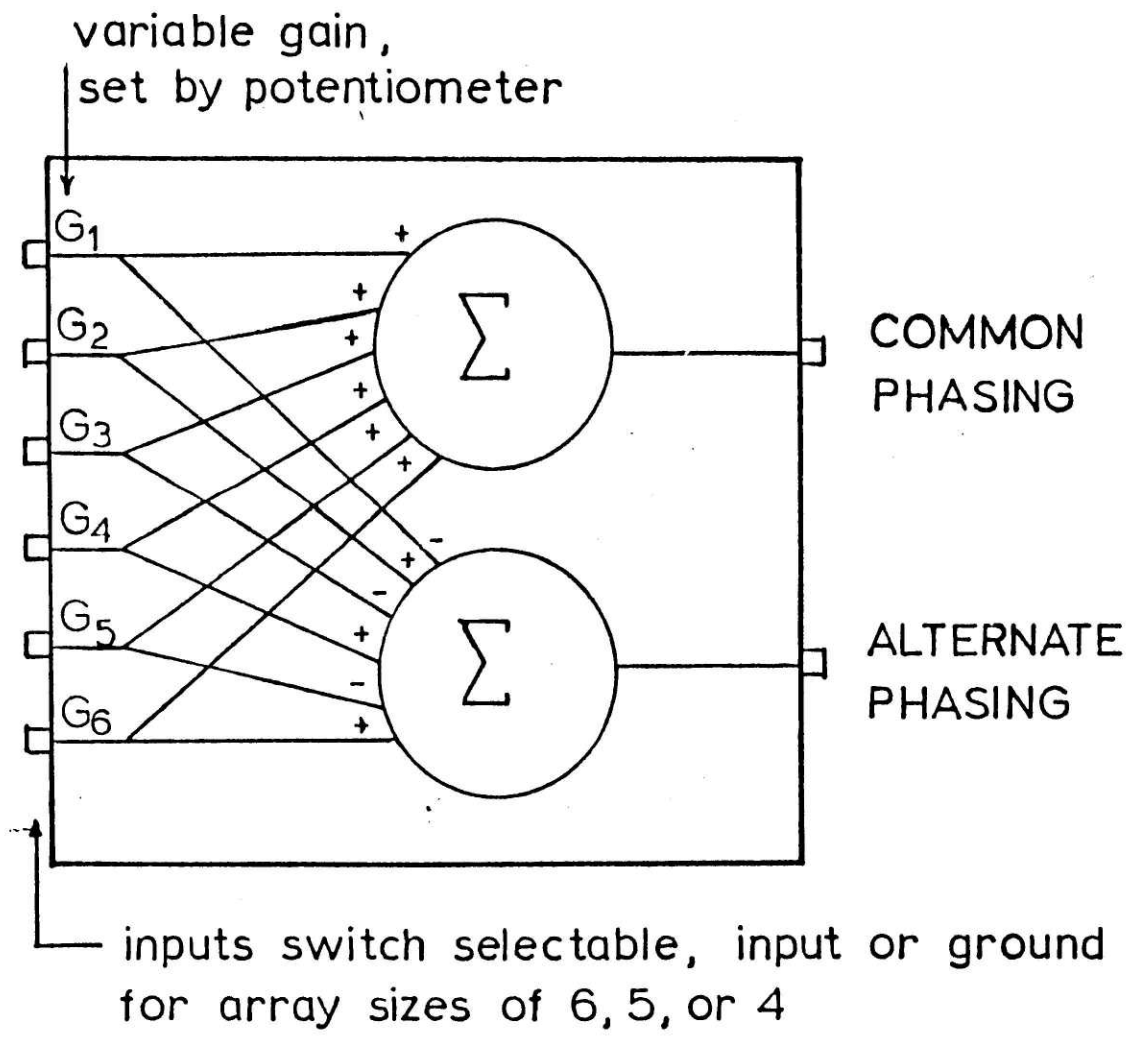
FIGURE 2.6   Schematic of Summation Box
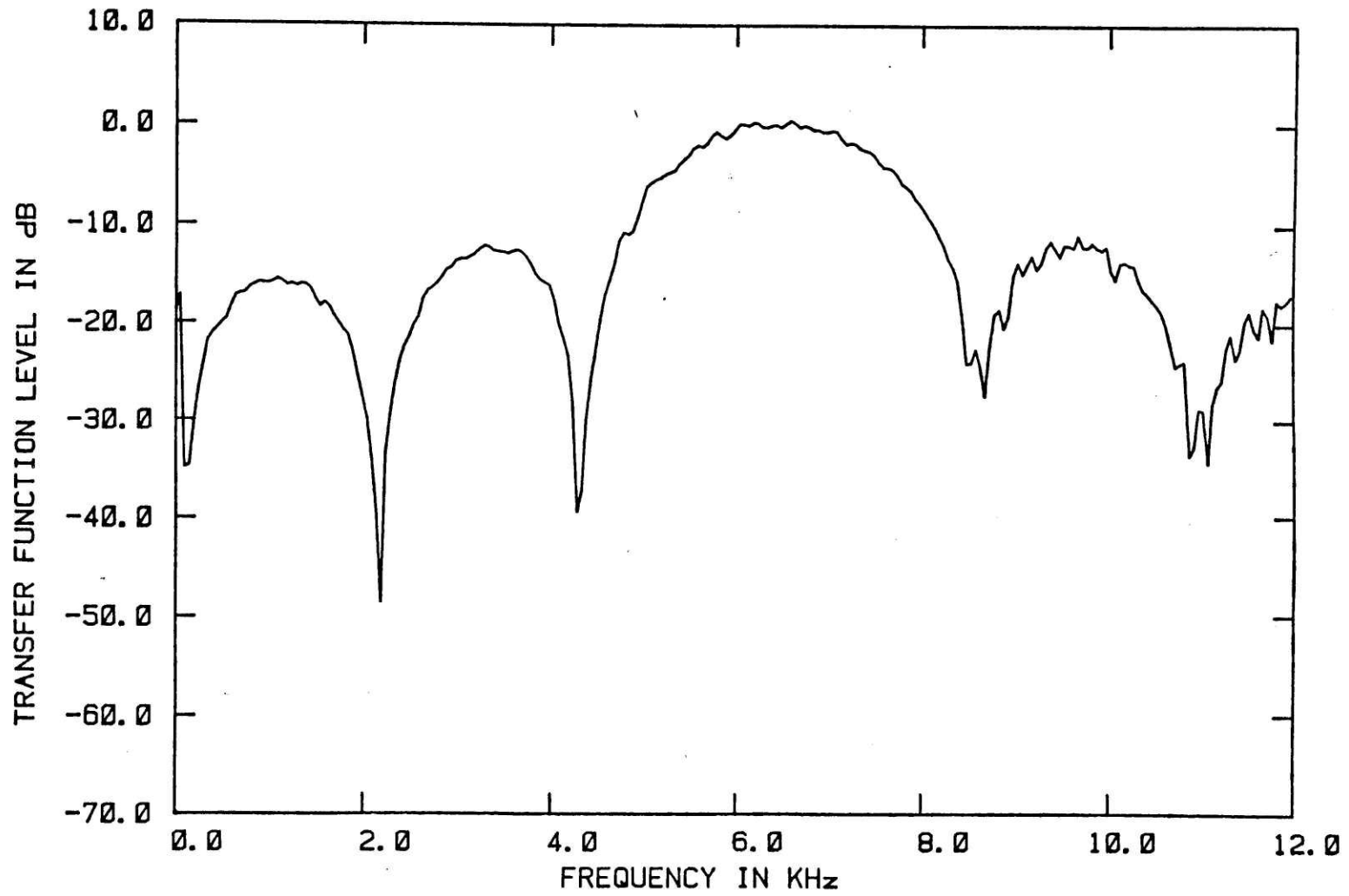
FIGURE 2.7   Measured Alternating Phased Wavenumber Response.
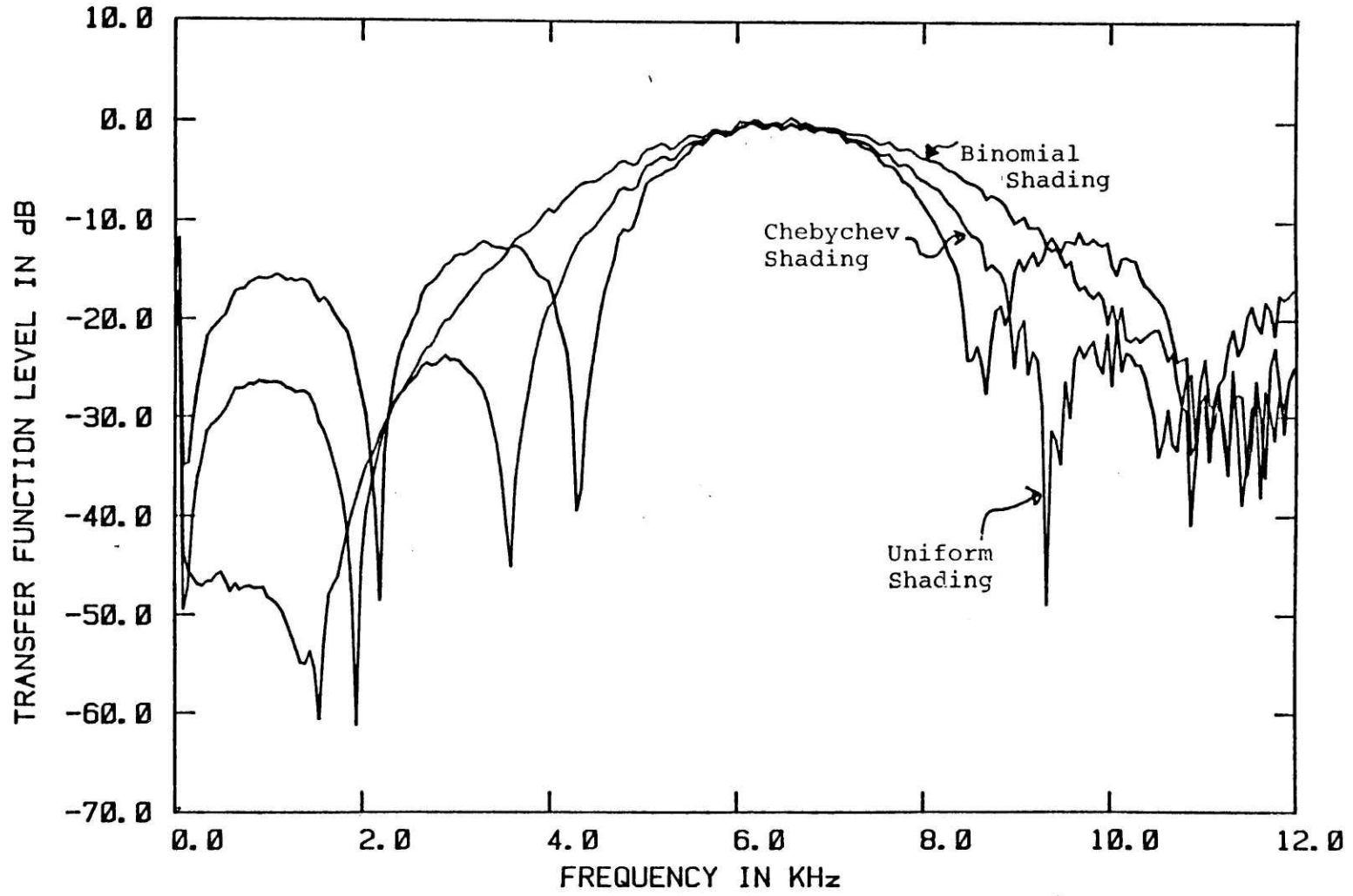
FIGURE 2.8 Effect of Shading on Wavenumber Response.
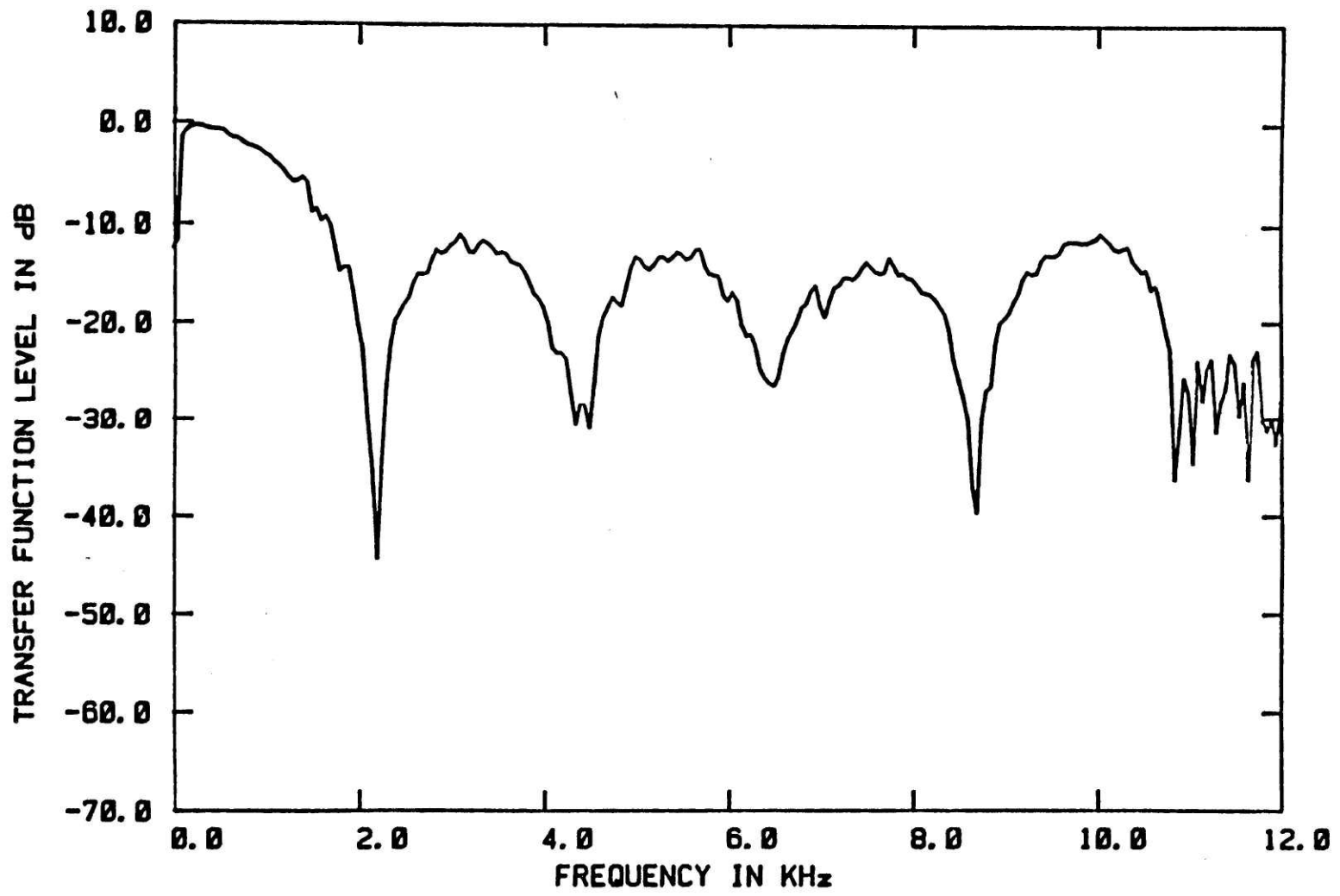
FIGURE 2.9 Measured Common Phase Array Wavenumber Response.
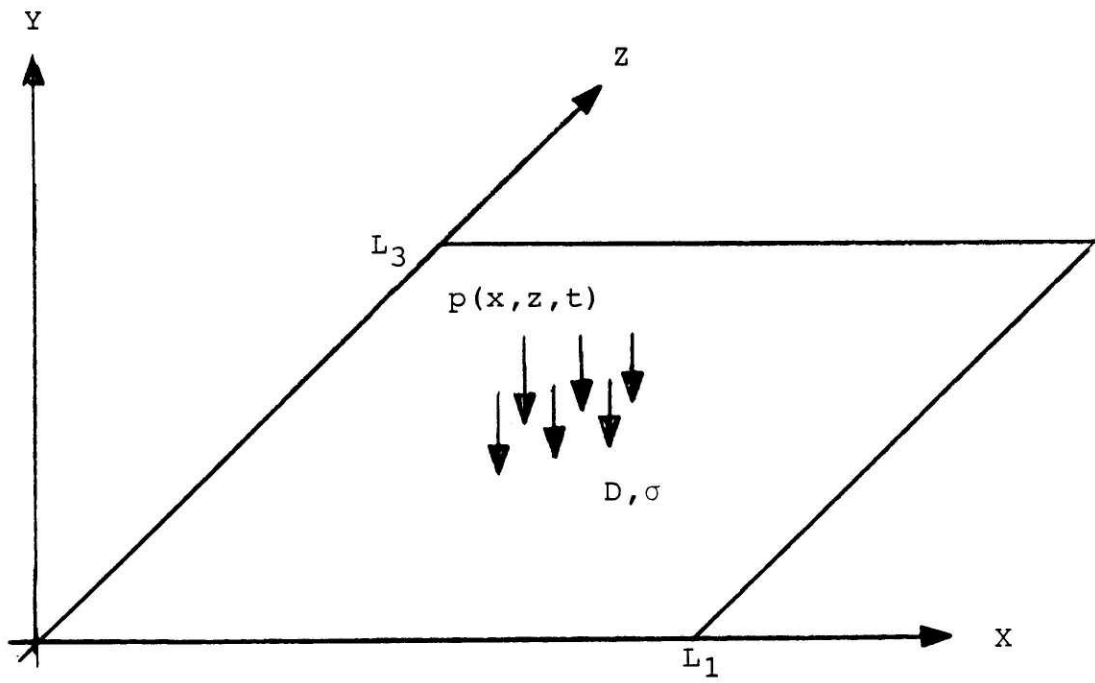
Figure 2.10. Geometric Consideration for Plates.

Test Section in
Reverberant/Anechoic
Chamber (Blockhouse)

Muffler &
Diffuser

Centrifugal
Blower

Settling Chamber

Contraction
Section

137.2 cm

223.5 cm

Honeycomb

16 x 18 Mesh
Screens

24 Mesh
Screens

Concrete Inertia Block
on Isolation Pads

20 H.P.
D.C. Motor

Elevation Scale:

100 cm'
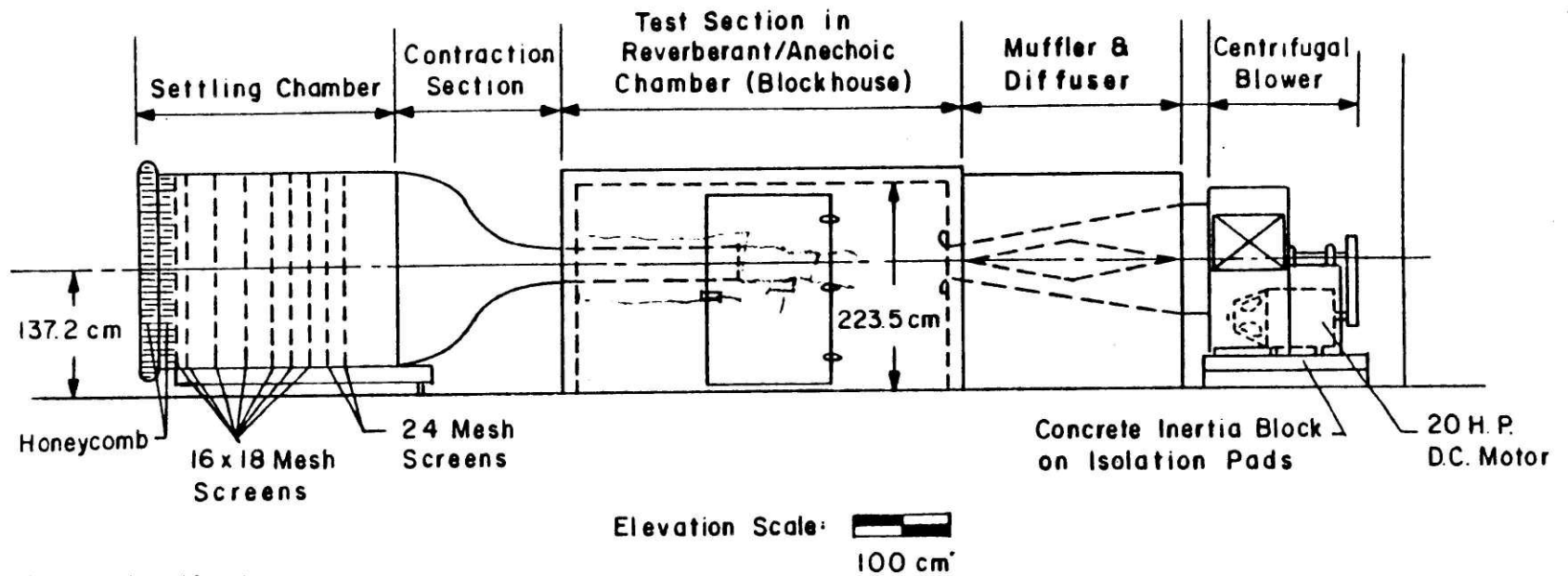
General Specifications:
Contraction Ratio: 20:1
Test Section: 38cm x 38cm, shown in
            open duct configuration

WIND TUNNEL FACILITY — ROOM 5-024
ACOUSTICS & VIBRATIONS LABORATORY
MASSACHUSETTS INSTITUTE OF TECHNOLOGY

FIGURE 3.1

FLOW ⟶

Splitter
Plate

Upstream
Ducting

Test
Section

Diffuser

Test fixture

Blockhouse
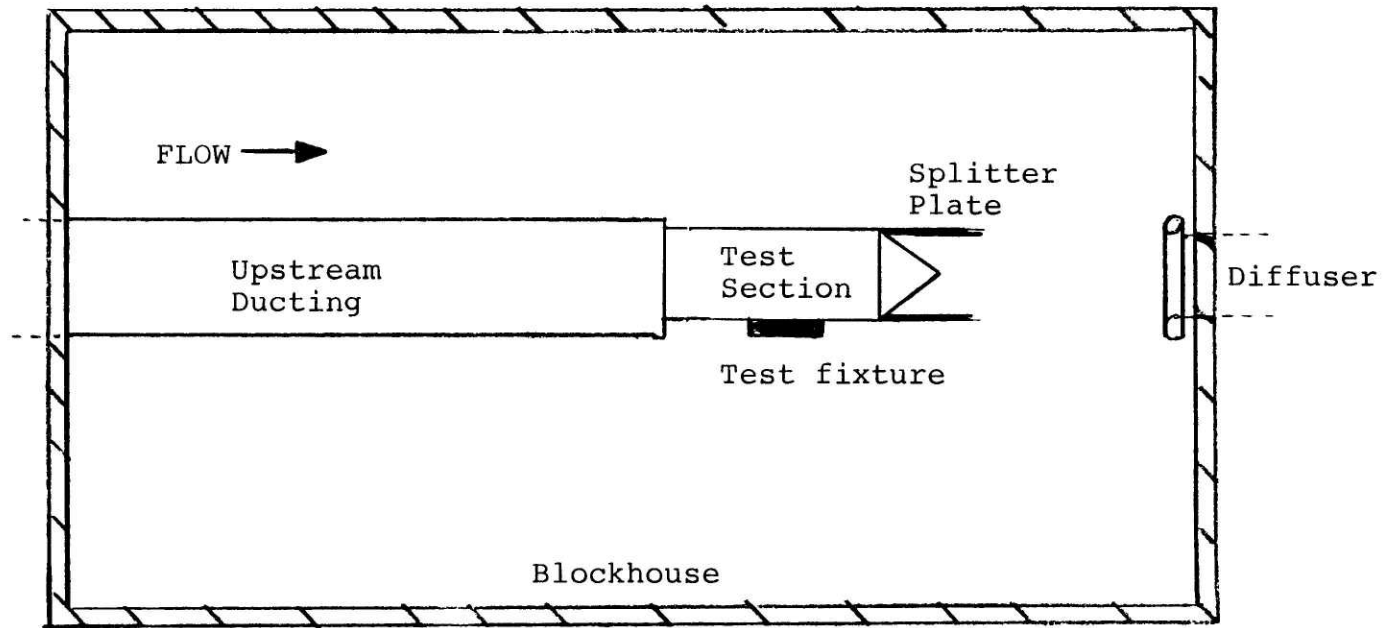
Figure 3.2.   Hardwalled Duct Configuration.

FLOW →

Test
Position 1

Test
Position 2

Diffuser

|← 0.45 →|

|← 1.34m →|

Blockhouse
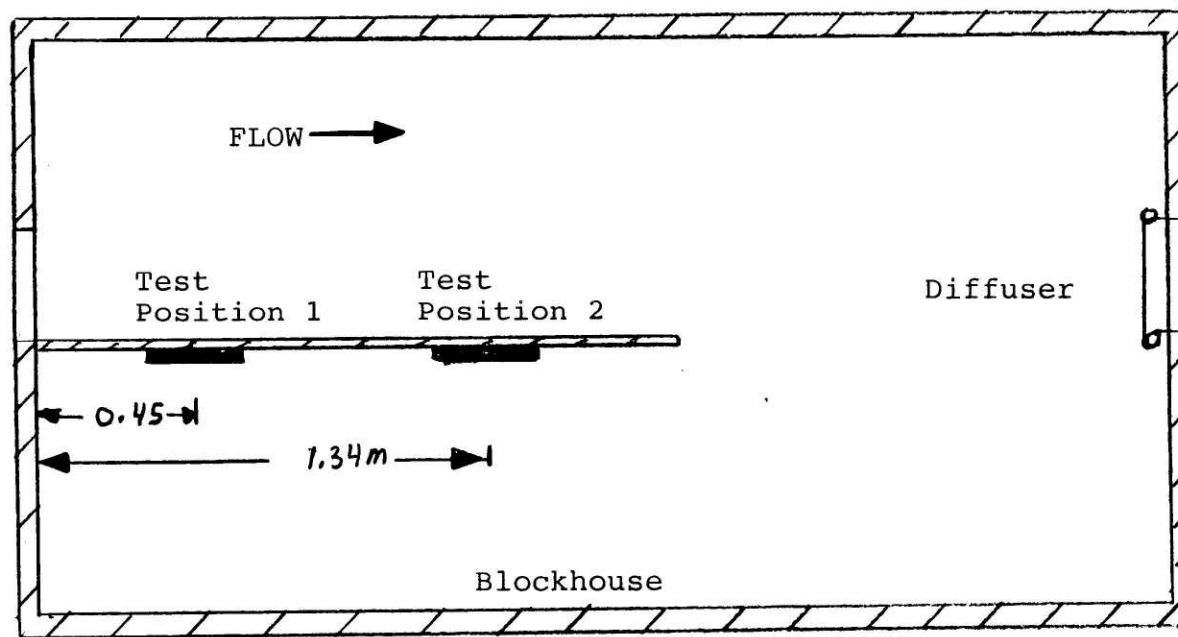
Figure 3.3. Wall Jet Configuration (side view).
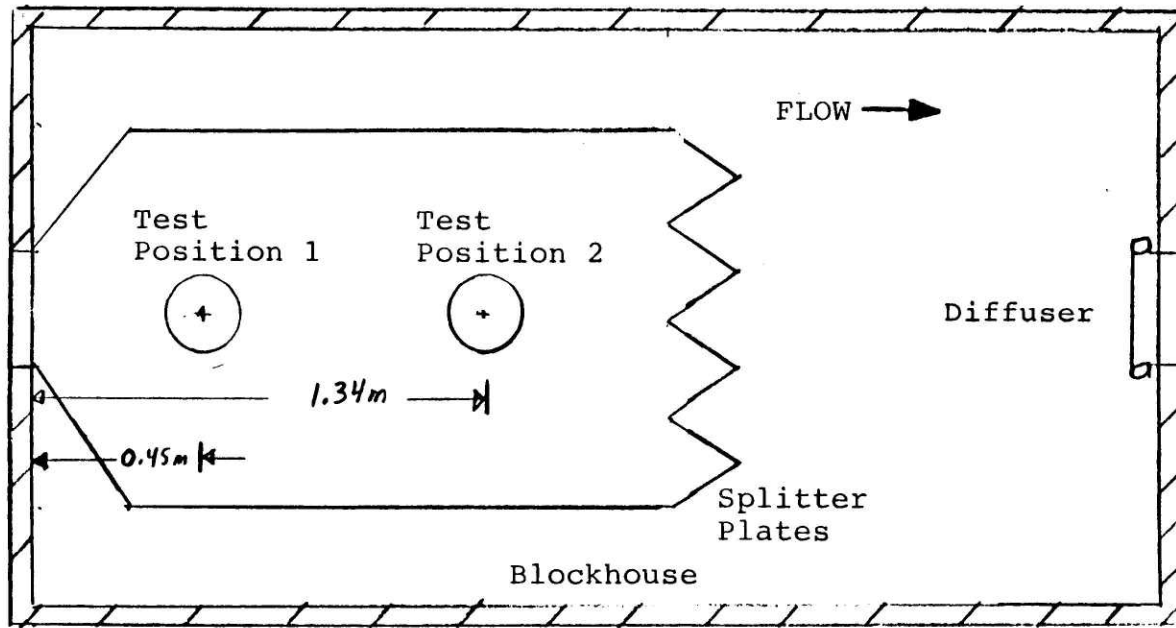
Figure 3.4. Wall Jet Configuration (top view).
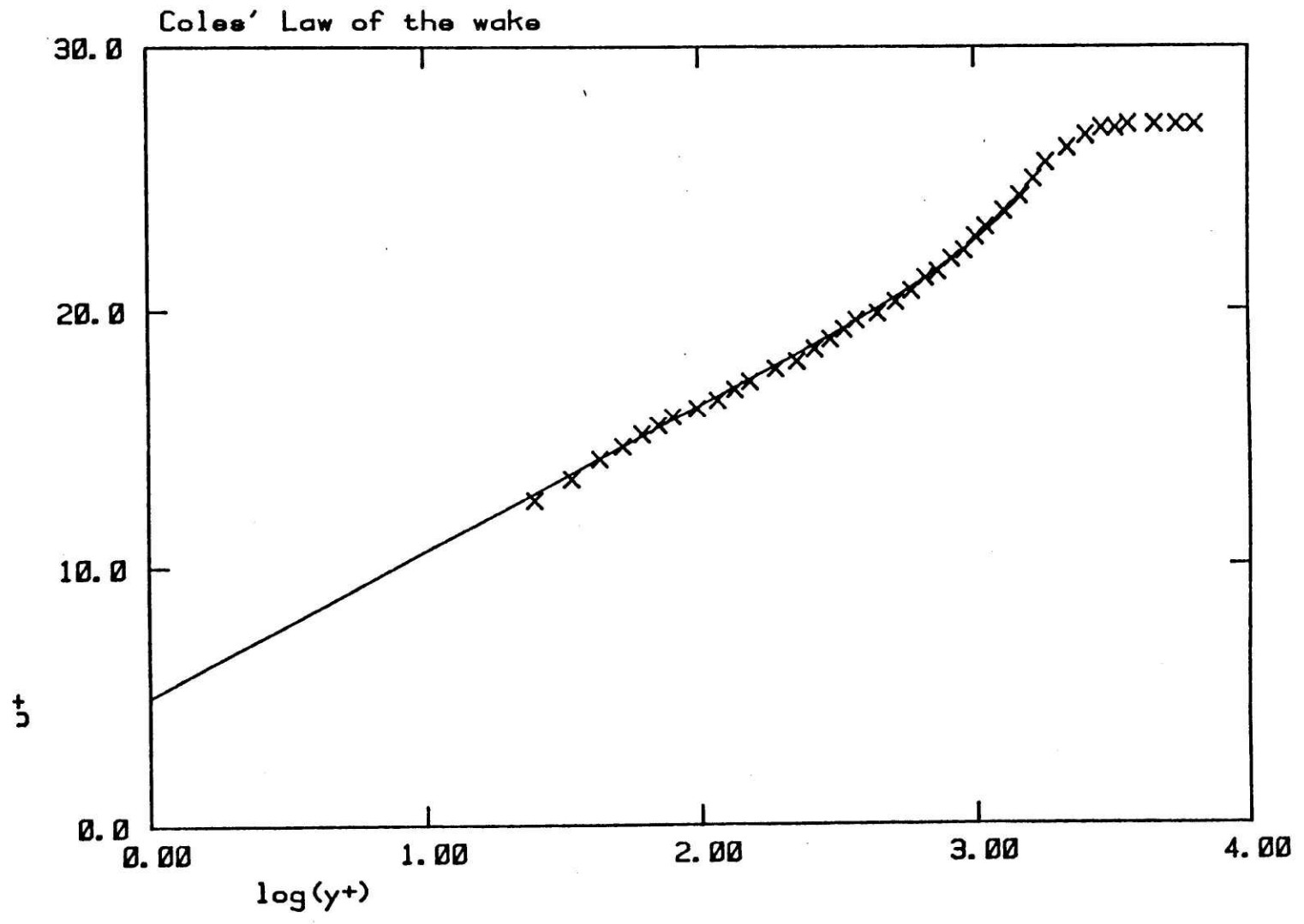
FIGURE 3.5 Boundary Layer Measurement Comparison
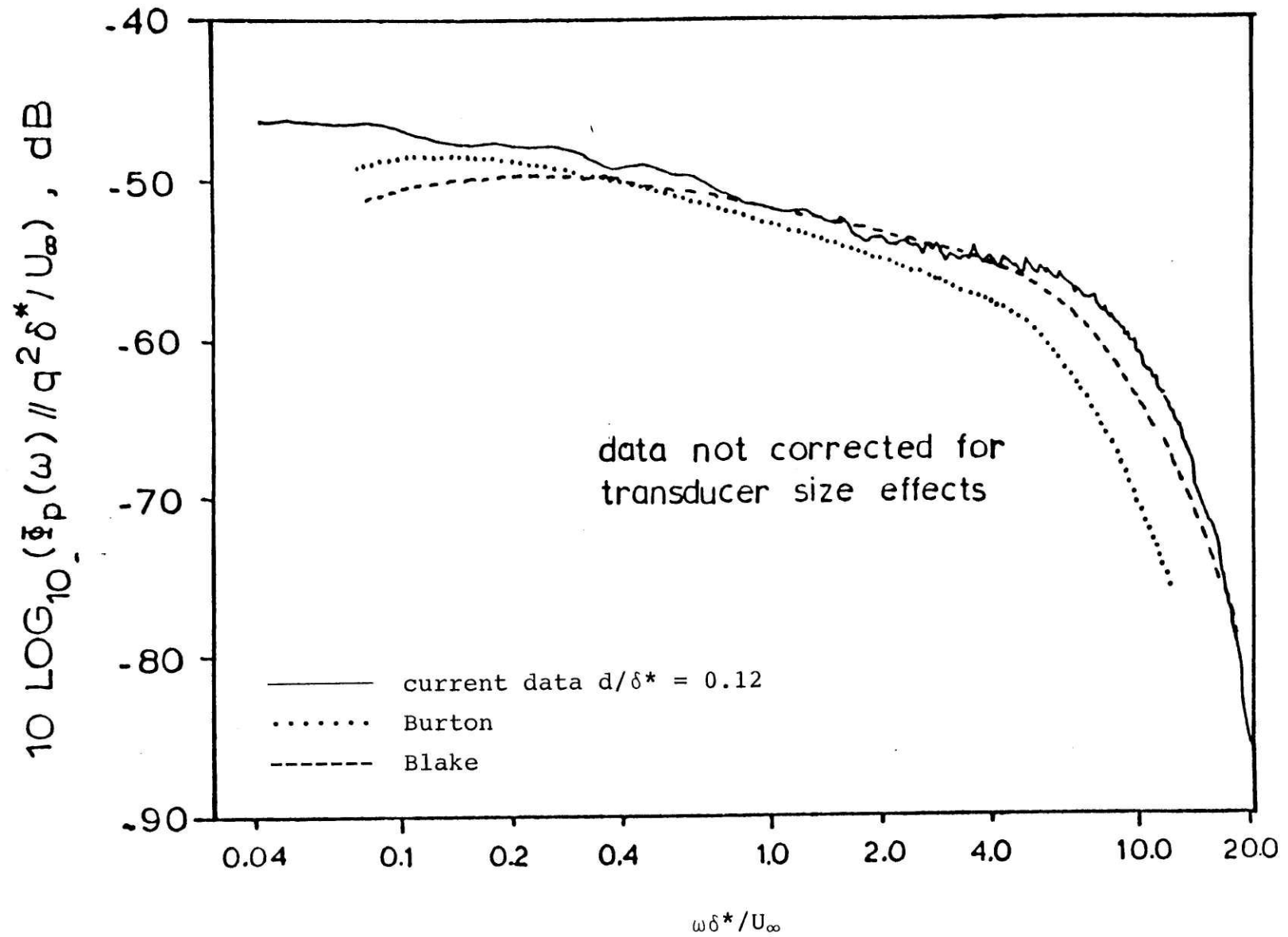
Figure 3.6. Single Point Wall Pressure Spectrum.

Blockhouse

Speaker

Test
Position

Speaker

Blockhouse
Microphone
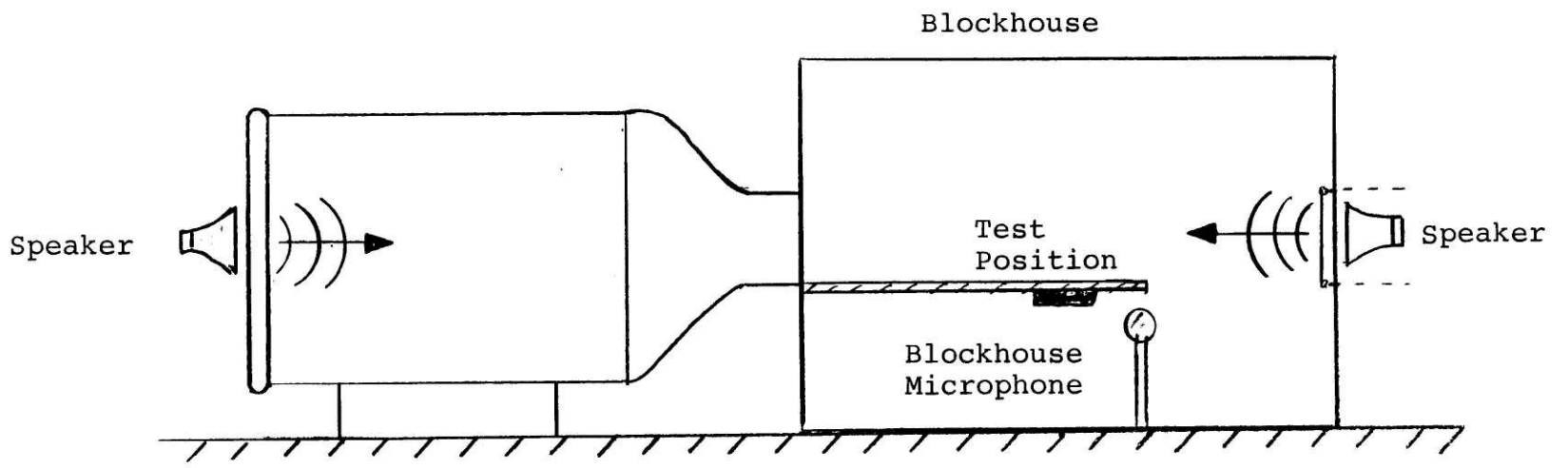
Figure 3.7. Acoustic Measurement Setup.
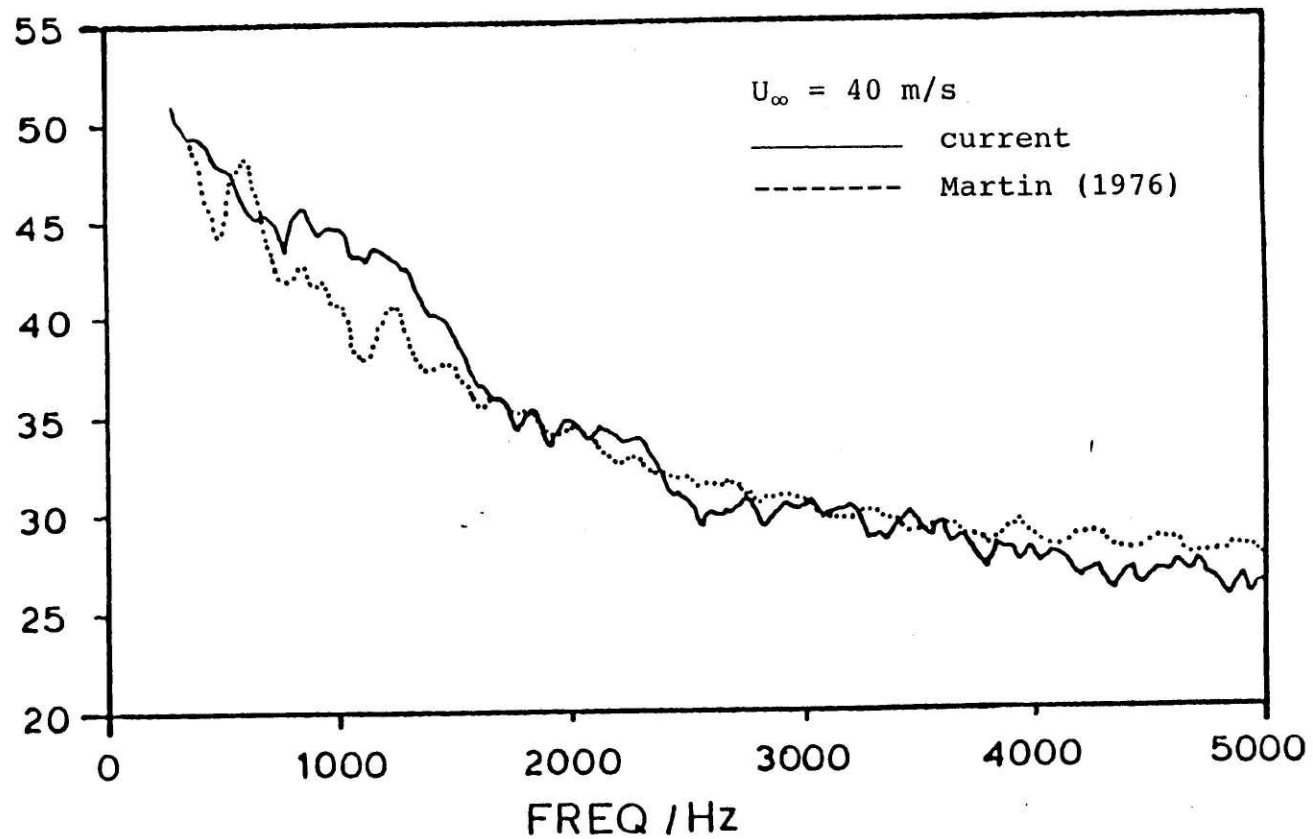
Figure 3.8. Spectrum Level Background Noise.
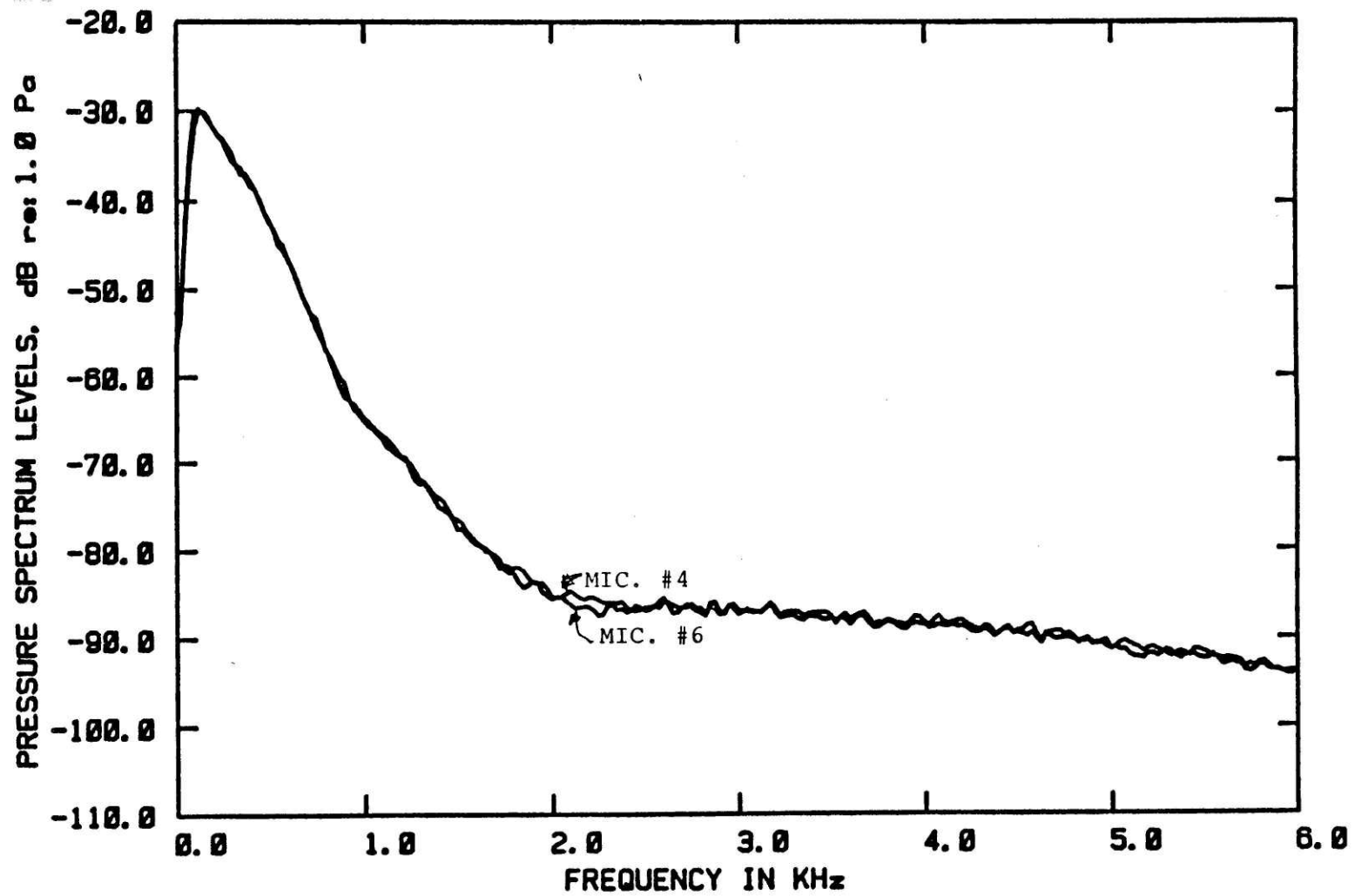
FIGURE 3.9 Comparison Between Two Flushed Mounted 1" Microphones @ 15 M/S.
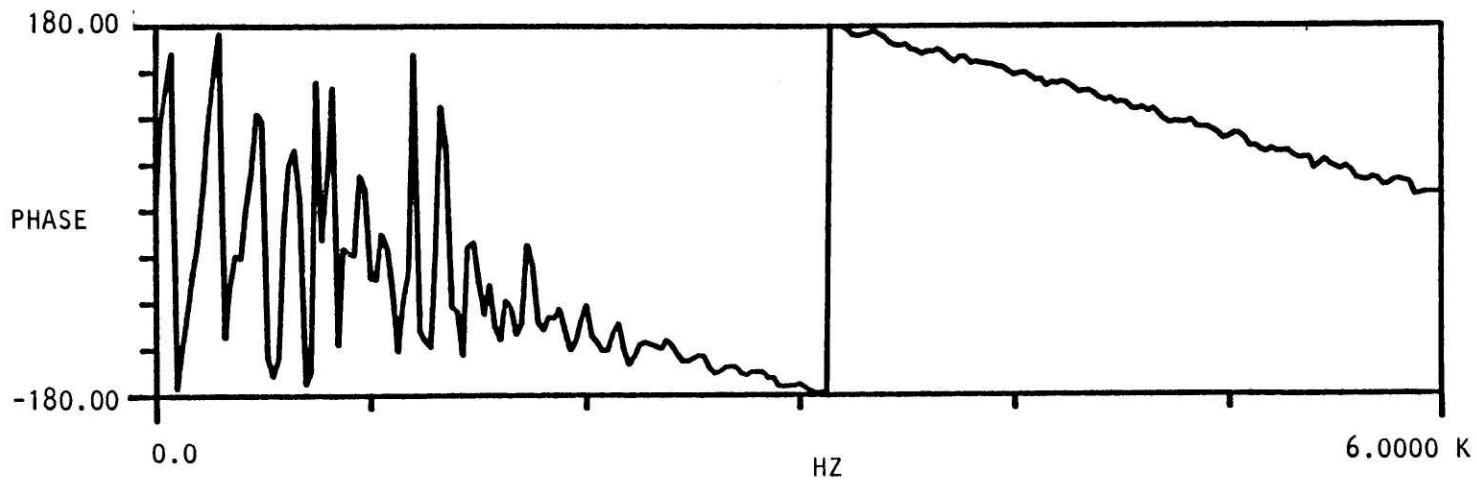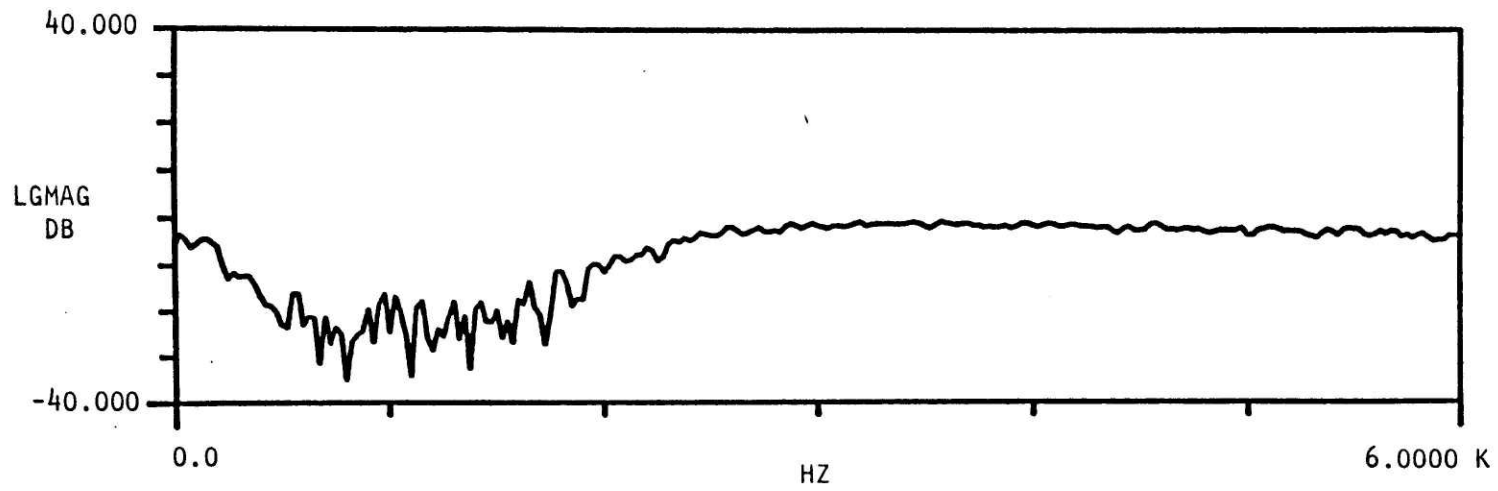
FIGURE 3.10   Cross Spectrum and Phase Between Two 1" Microphones @ 15 M/S.
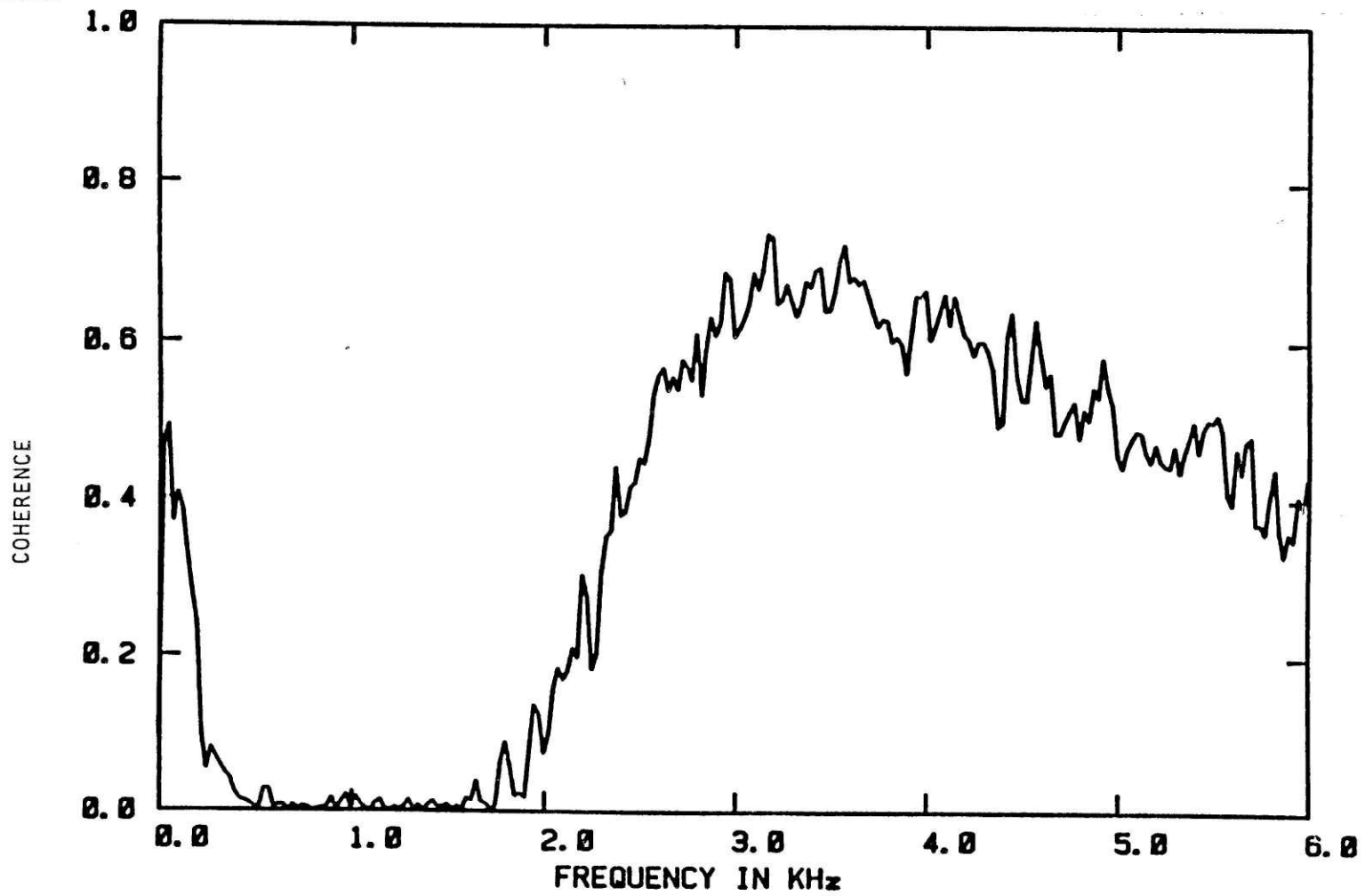
FIGURE 3.11   Coherence Between Two 1" Microphones @ 15 M/S.
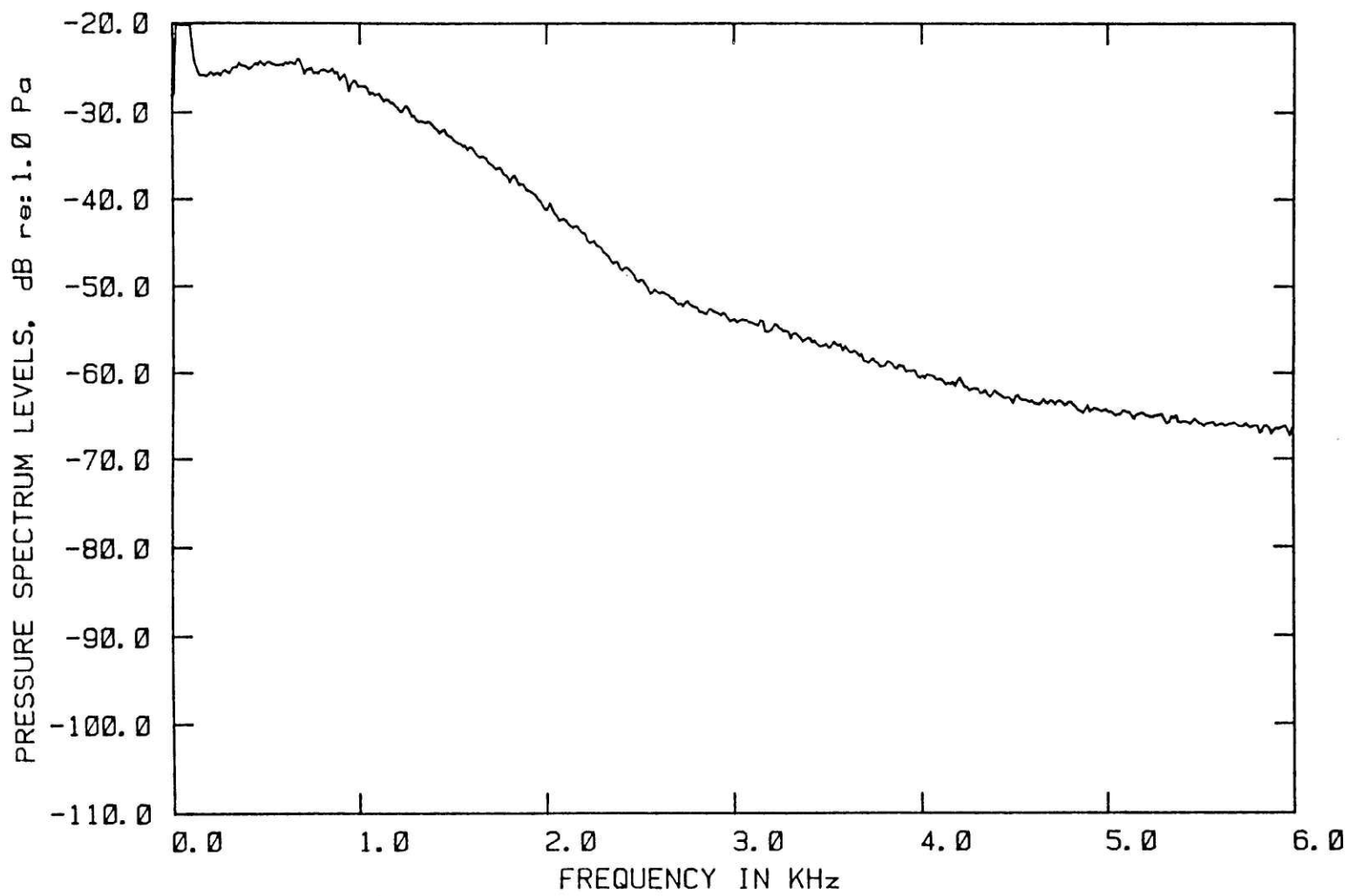
FIGURE 3.12 Single Point Wall Pressure Measurement @ 40 M/S.
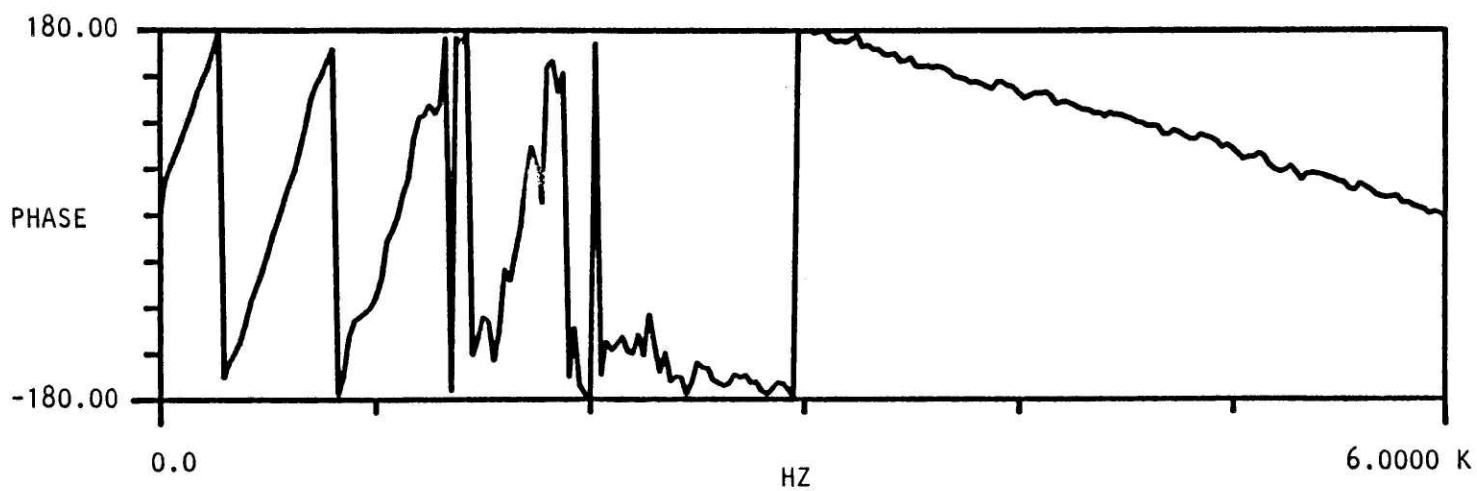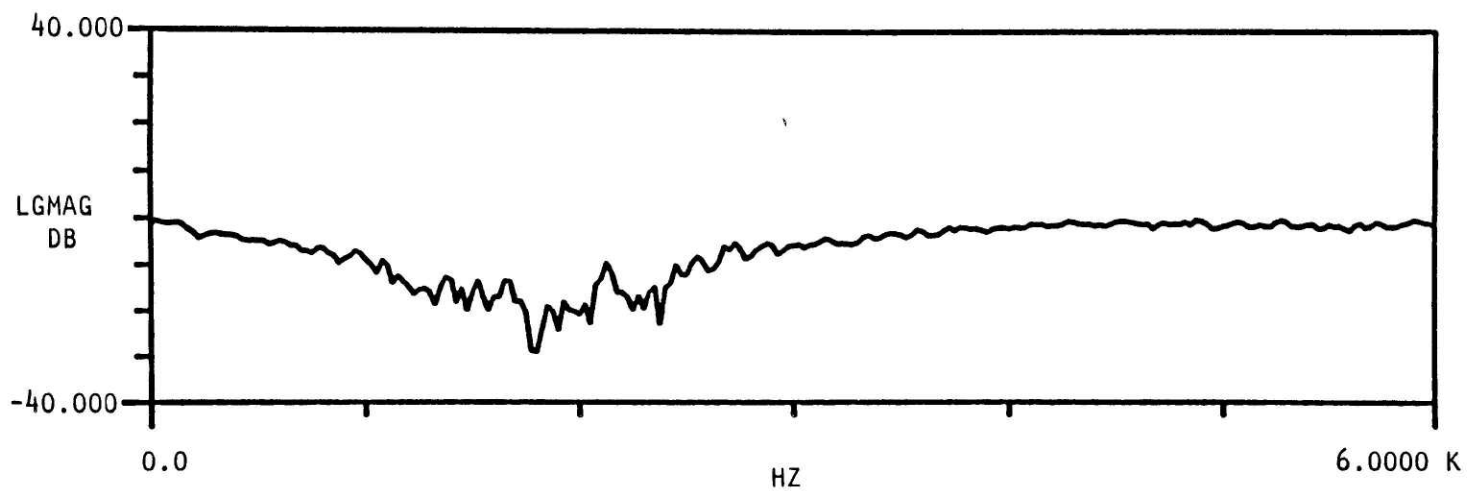
FIGURE 3.13 Cross Spectrum and Phase Relation Between Two Microphones
@ 40 M/S.
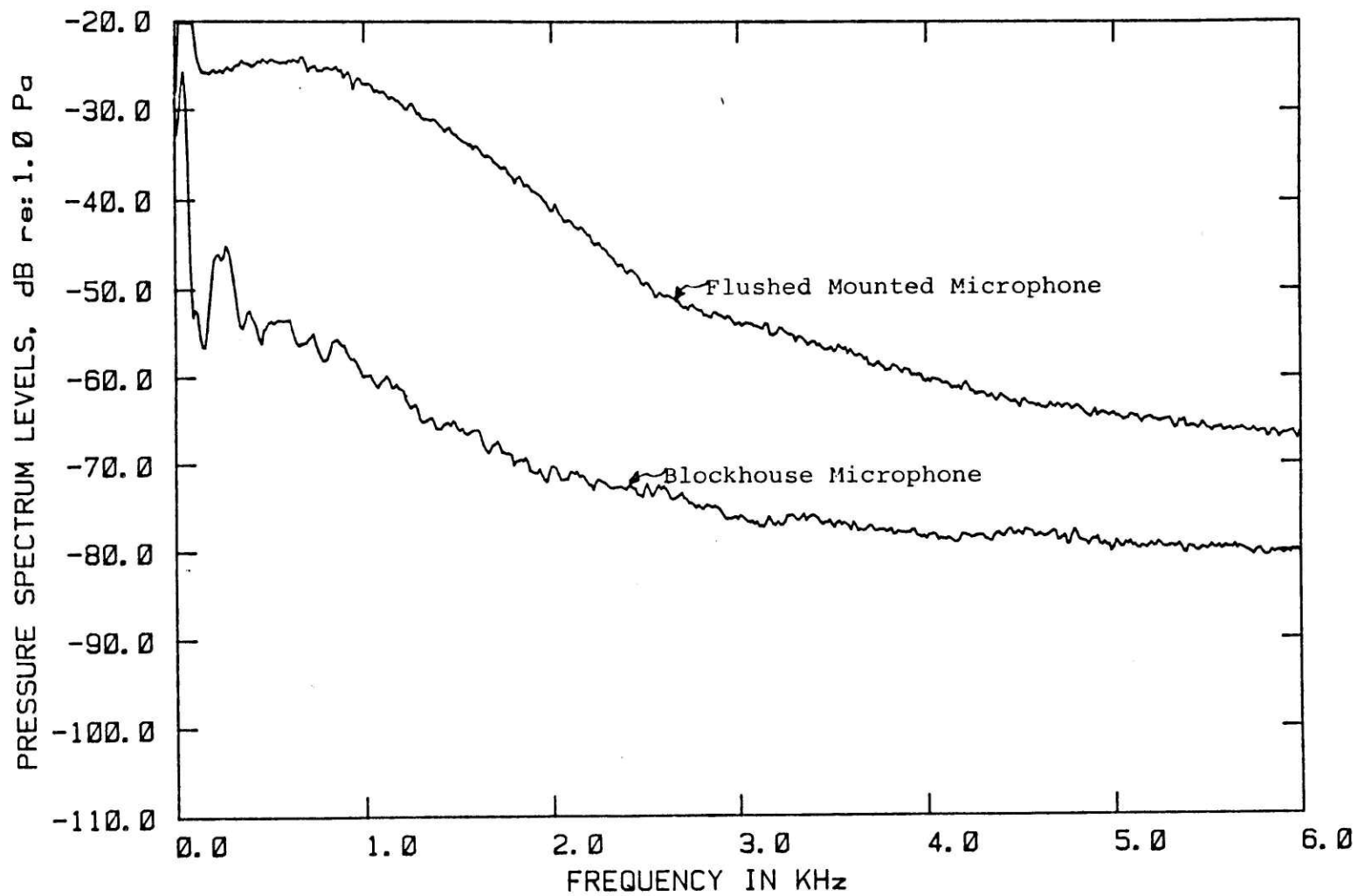
FIGURE 3.14   Comparison Between Blockhouse Noise Measurements and Flush
Mounted Microphone @ 40 M/S.
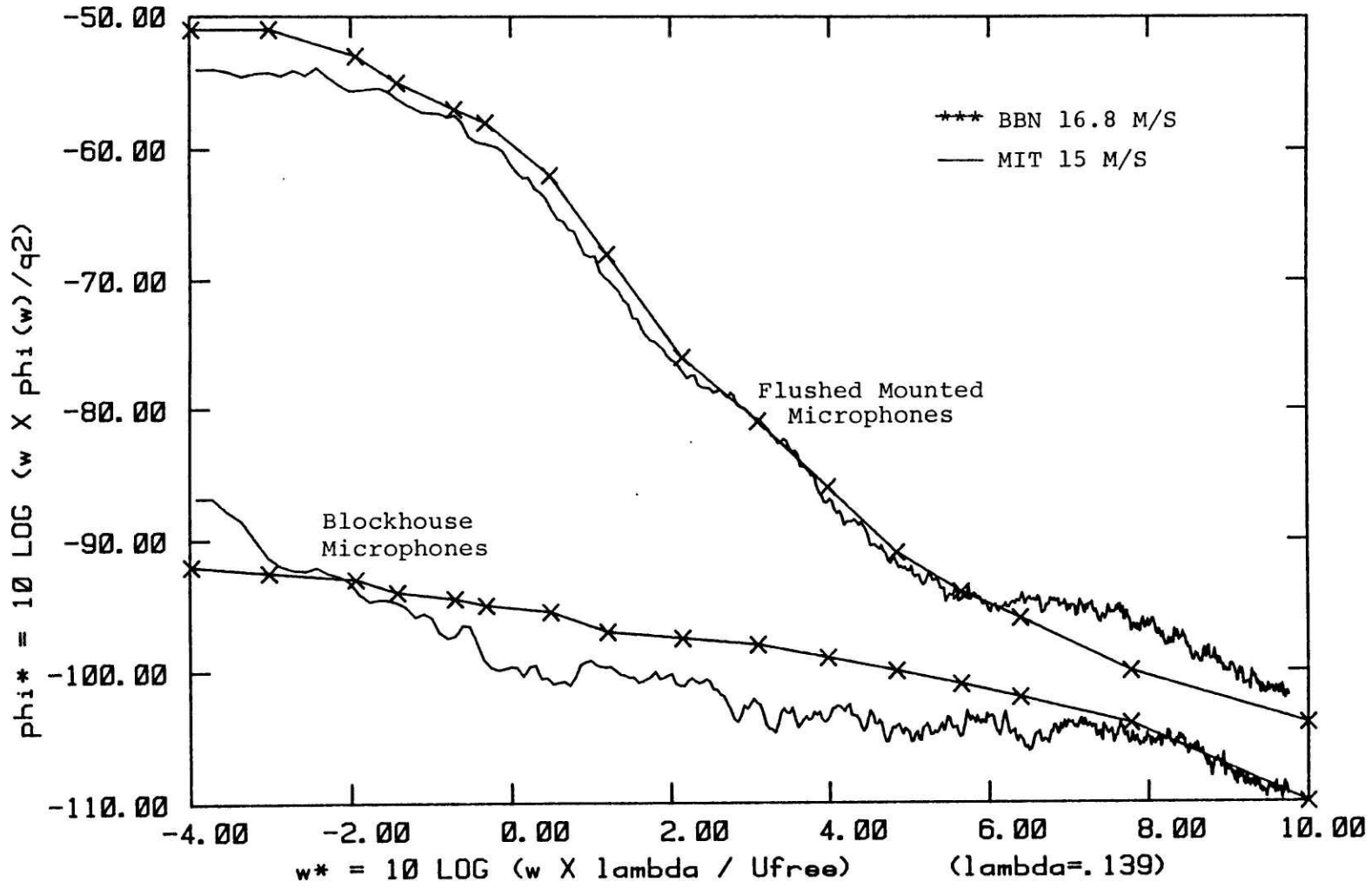
FIGURE 3.15   Comparison of M.I.T. Facility With BBN Facility.
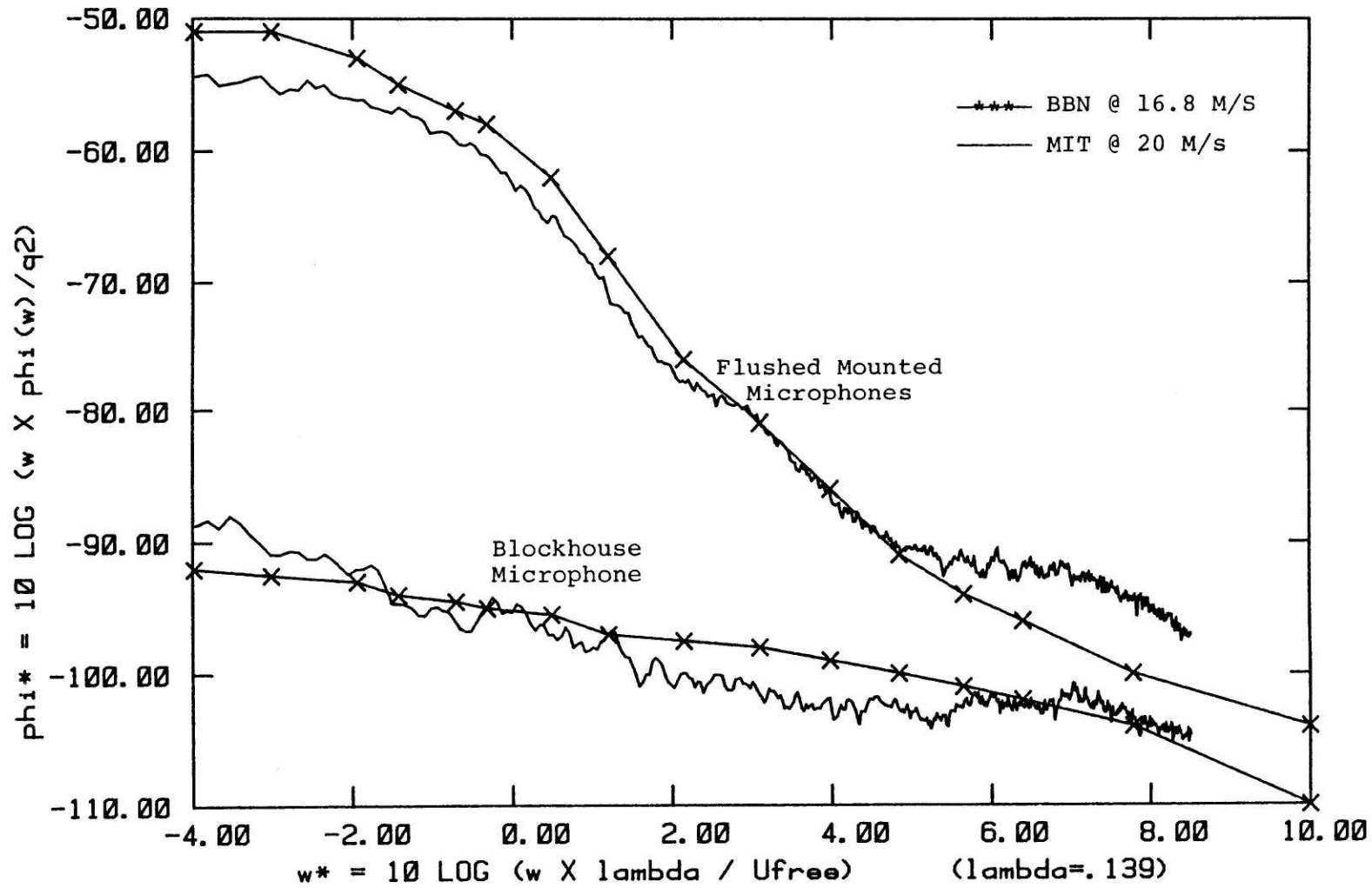
FIGURE 3.16 Comparison of M.I.T. Facility With BBN Facility.
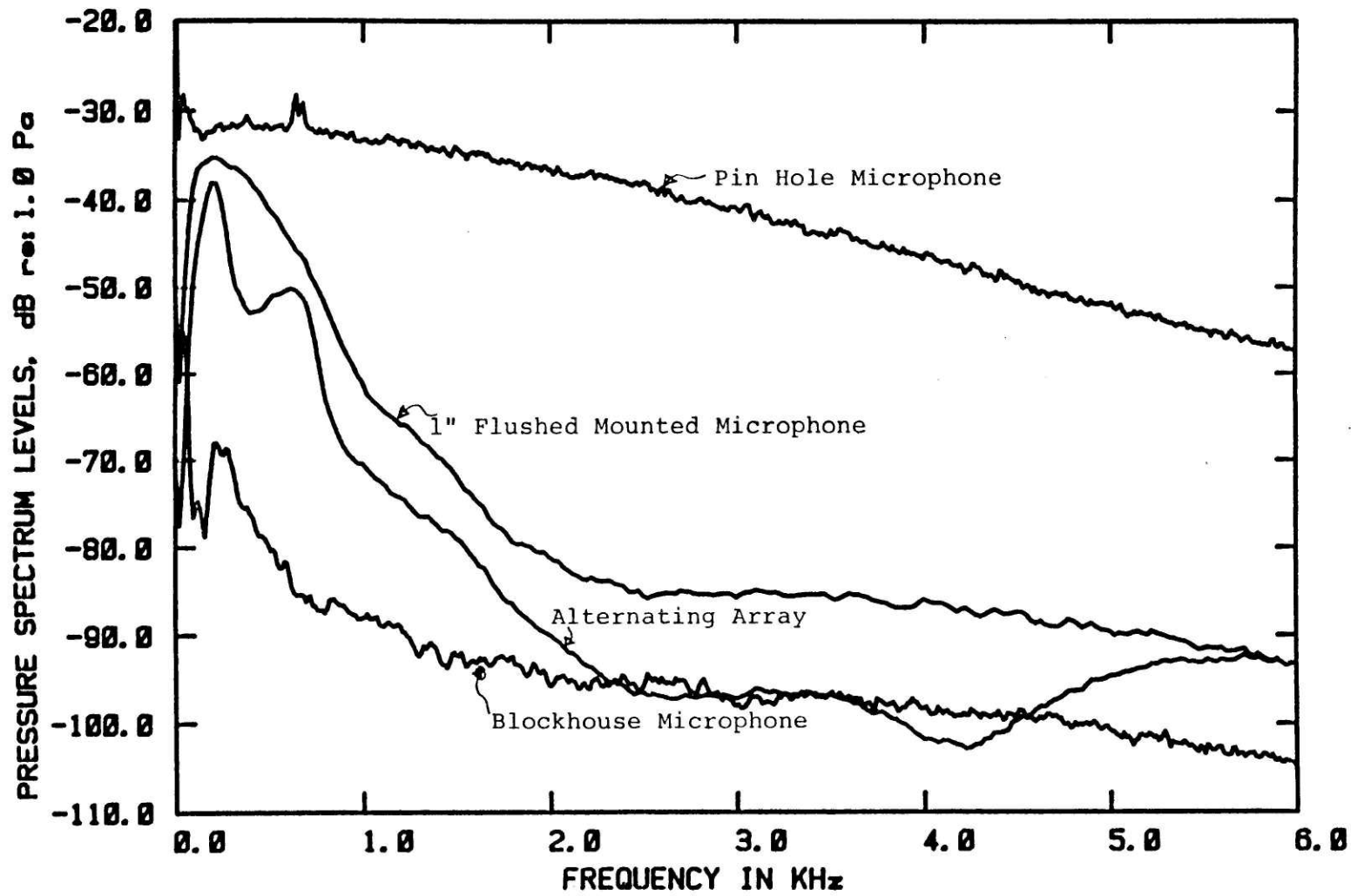
FIGURE 4.1 Comparison of Various Microphone Measurements @ 15 M/S.

$\Phi(k_1, \omega_o)$

Possible Acoustic
Pressure Spectrum

Array
Sensitivity

Turbulent
Pressure
Spectrum in k_1
at frequency
$\frac{\omega_o}{2\Pi}$

$\frac{\omega_o}{c}$ $\frac{1}{2\delta^*}$ k_{1_o} $\frac{\omega_o}{U_c}$ k_1

ω

ω_o

Locus of
the peak
of the
turbulent
pressure
spectrum

Peak of array
sensitivity

k_1 limit
of
acoustic
spectrum

$\frac{\omega_o}{c}$ k_{1_o} $\frac{\omega_o}{U_c}$ k_1
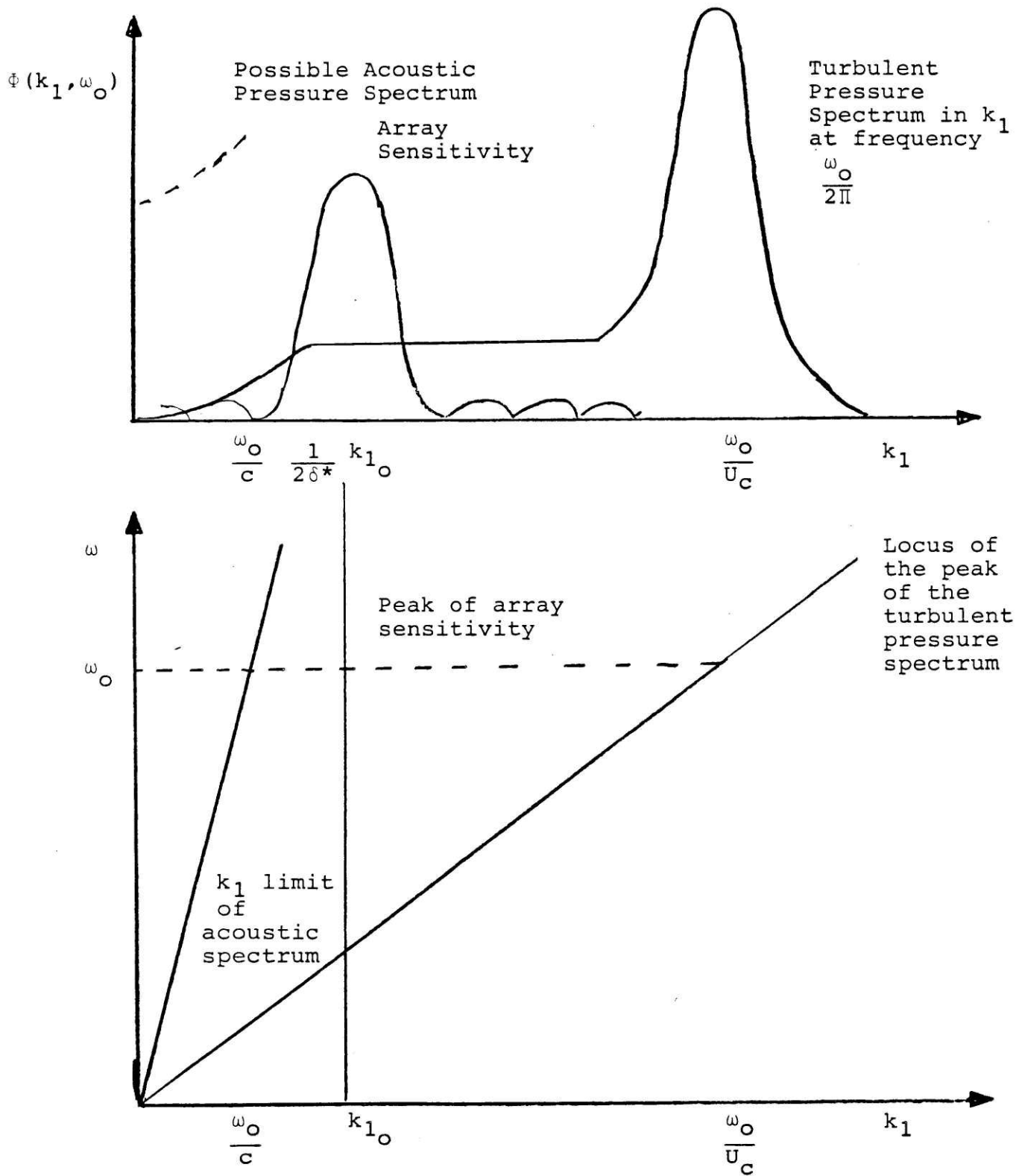
Figure 4.2.   Schematic of the Relationship among the Turbulent,
Array, and Acoustic Pressure Spectra at Fixed
Frequency $\omega_o/2\Pi$.
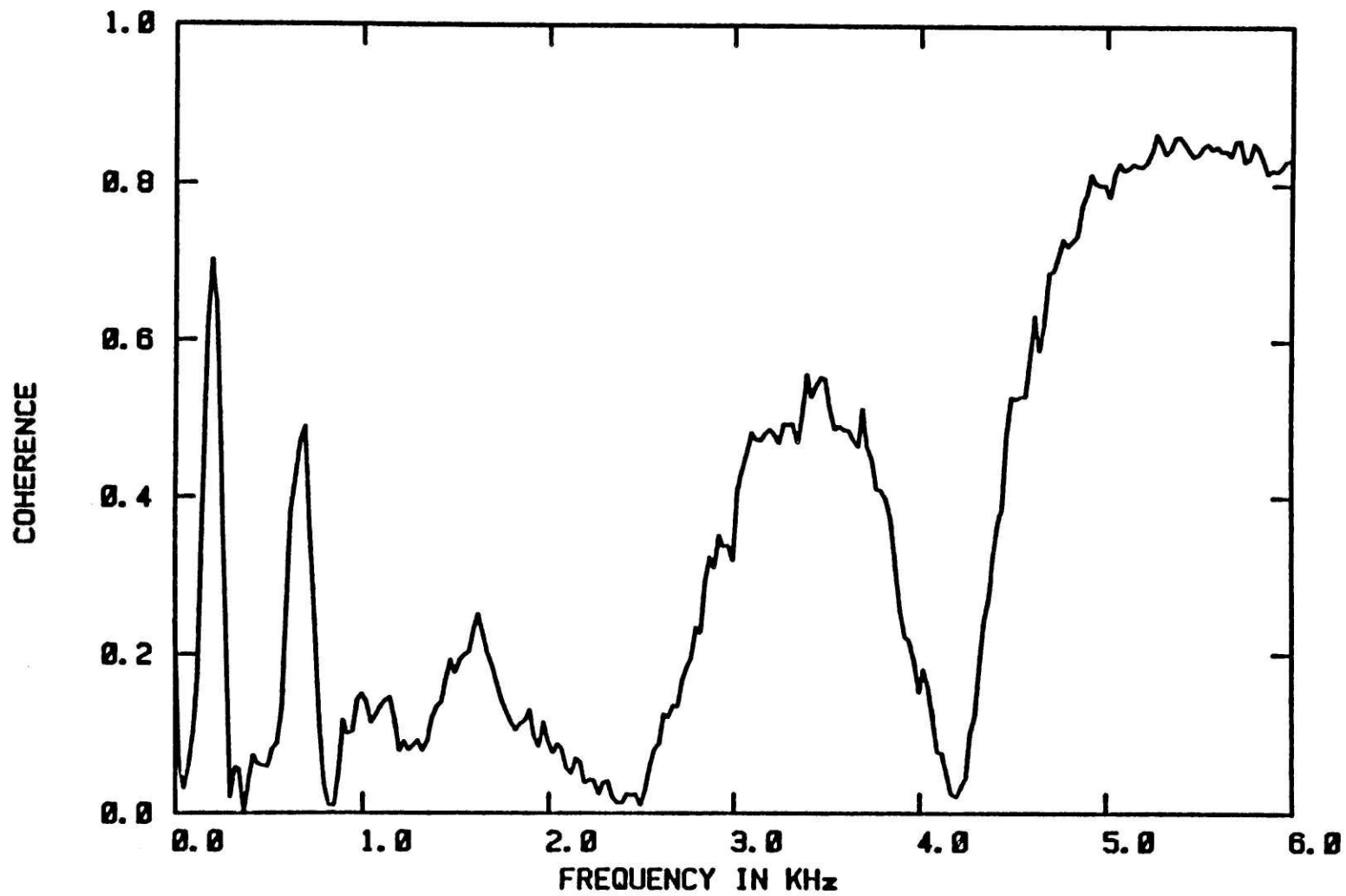
FIGURE 4.3   Coherence Between the Array and a Single Microphone in the
Array @ 15 M/S.
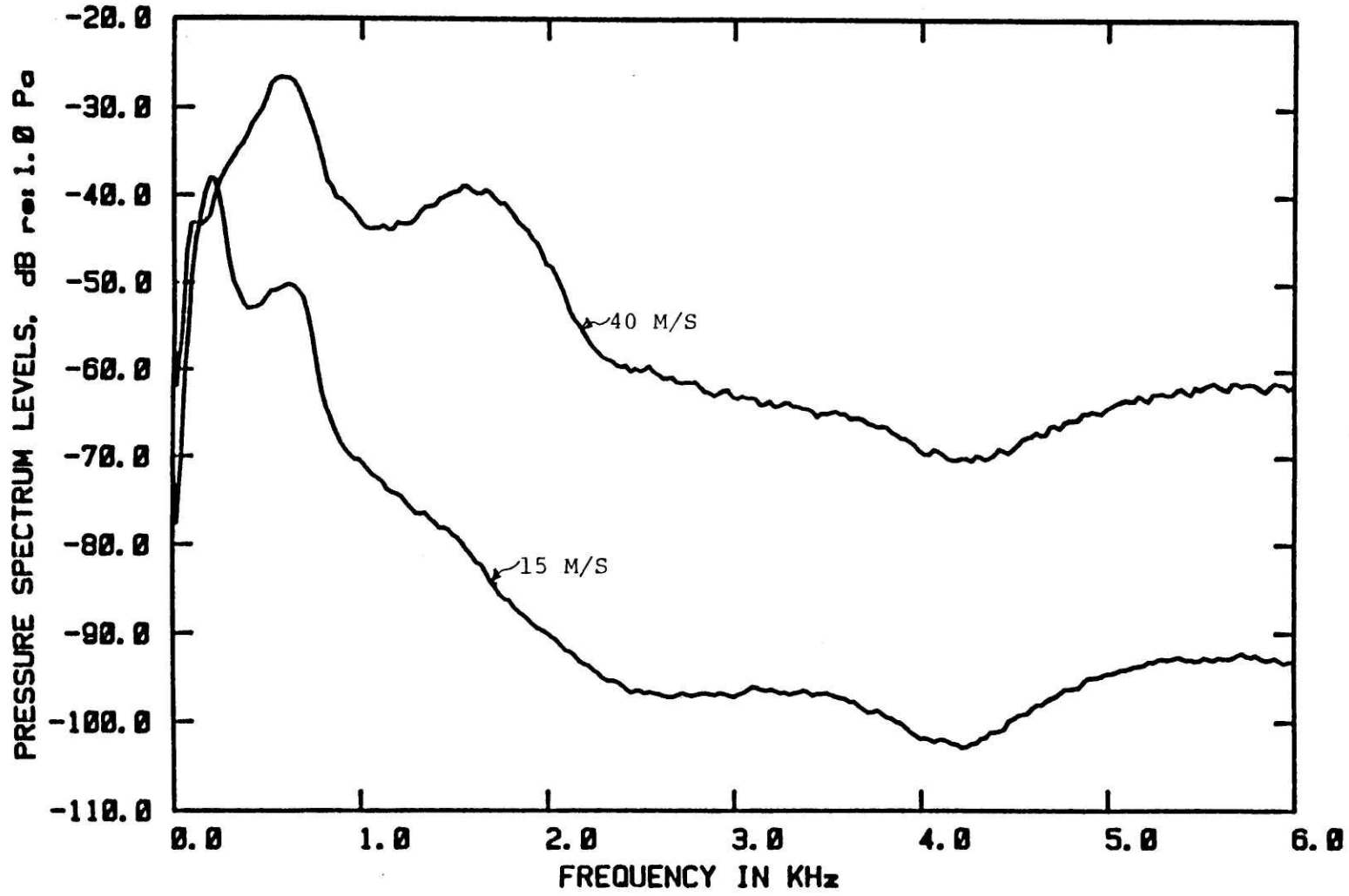
FIGURE 4.4 Comparison of Alternating Phased Array @ 15 M/S and 40 M/S.
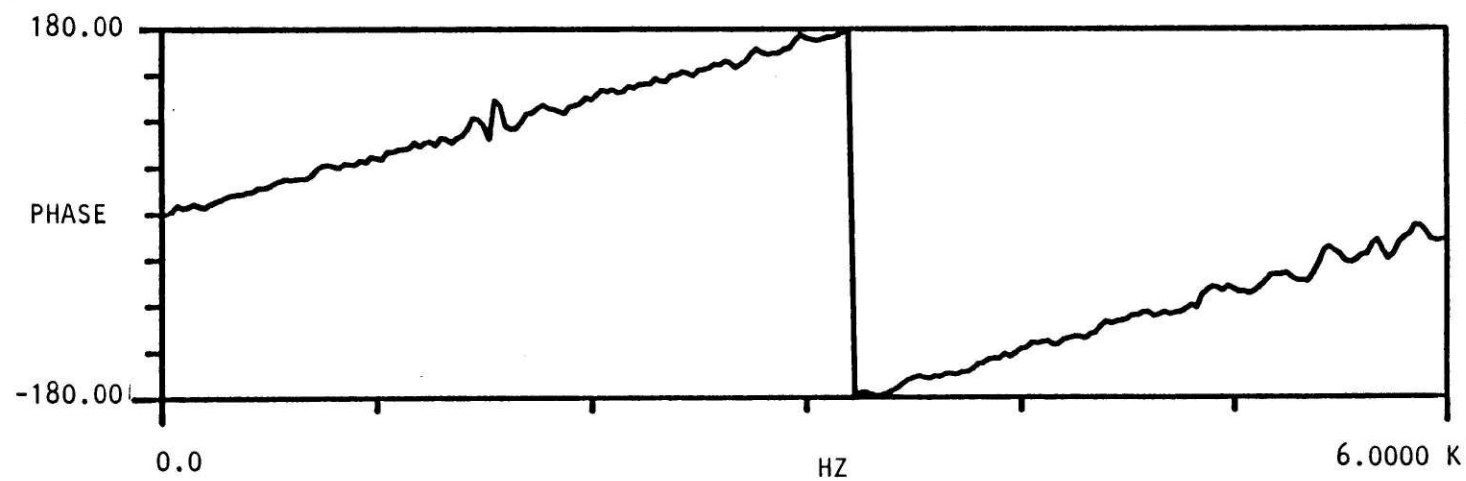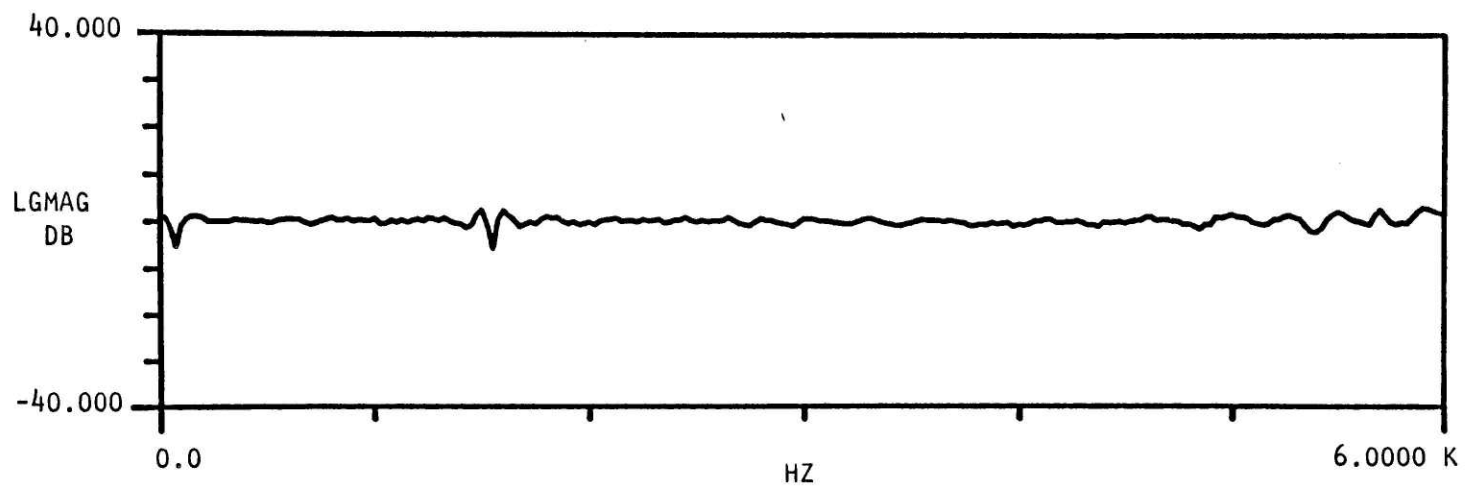
FIGURE 4.5 Cross Spectrum and Phase Relation Between Two Microphones
Excited by a Plane Acoustic Wave.
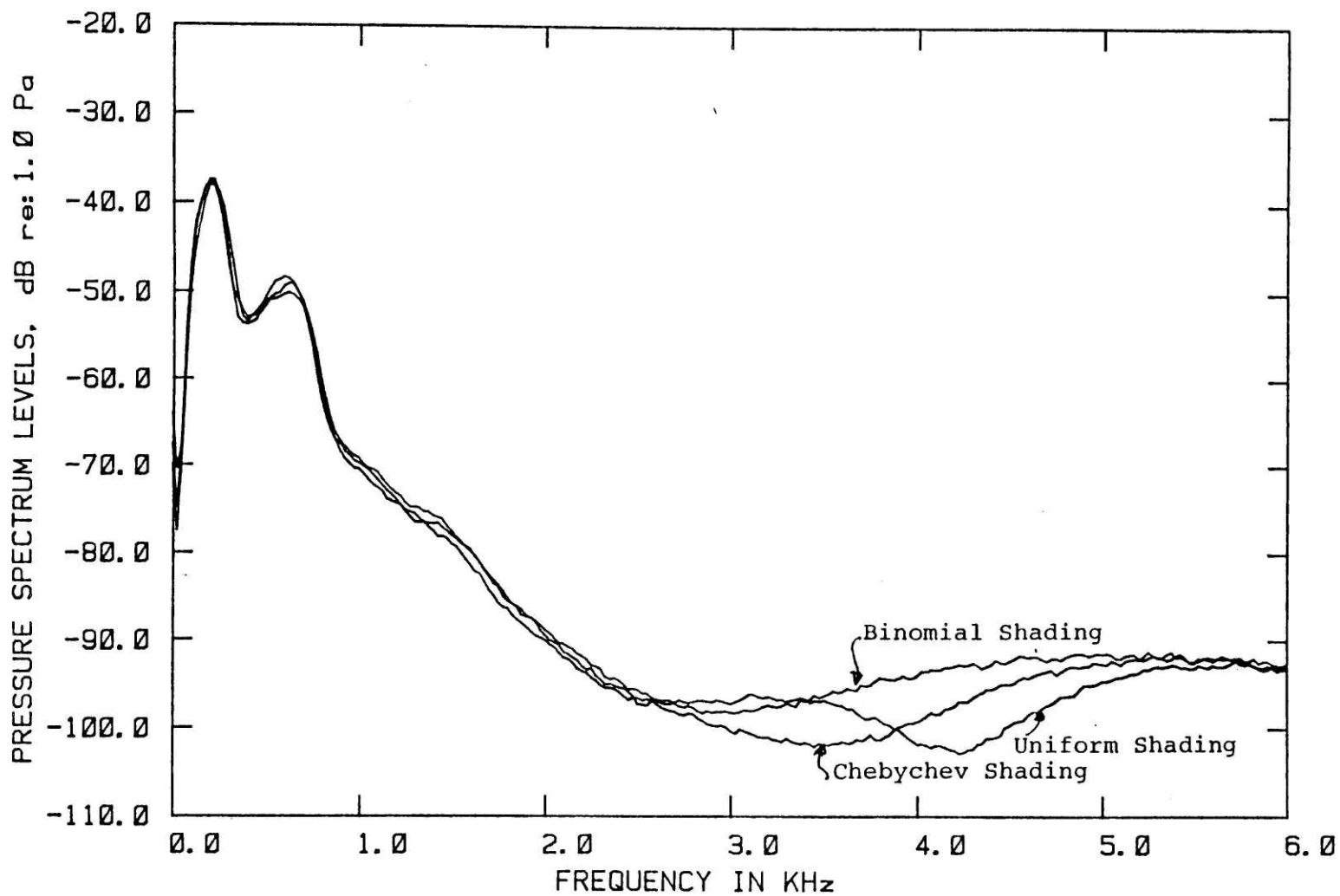
FIGURE 4.6   Comparison of the Alternating Phased Array Response for
Various Shading @ 15 M/S.
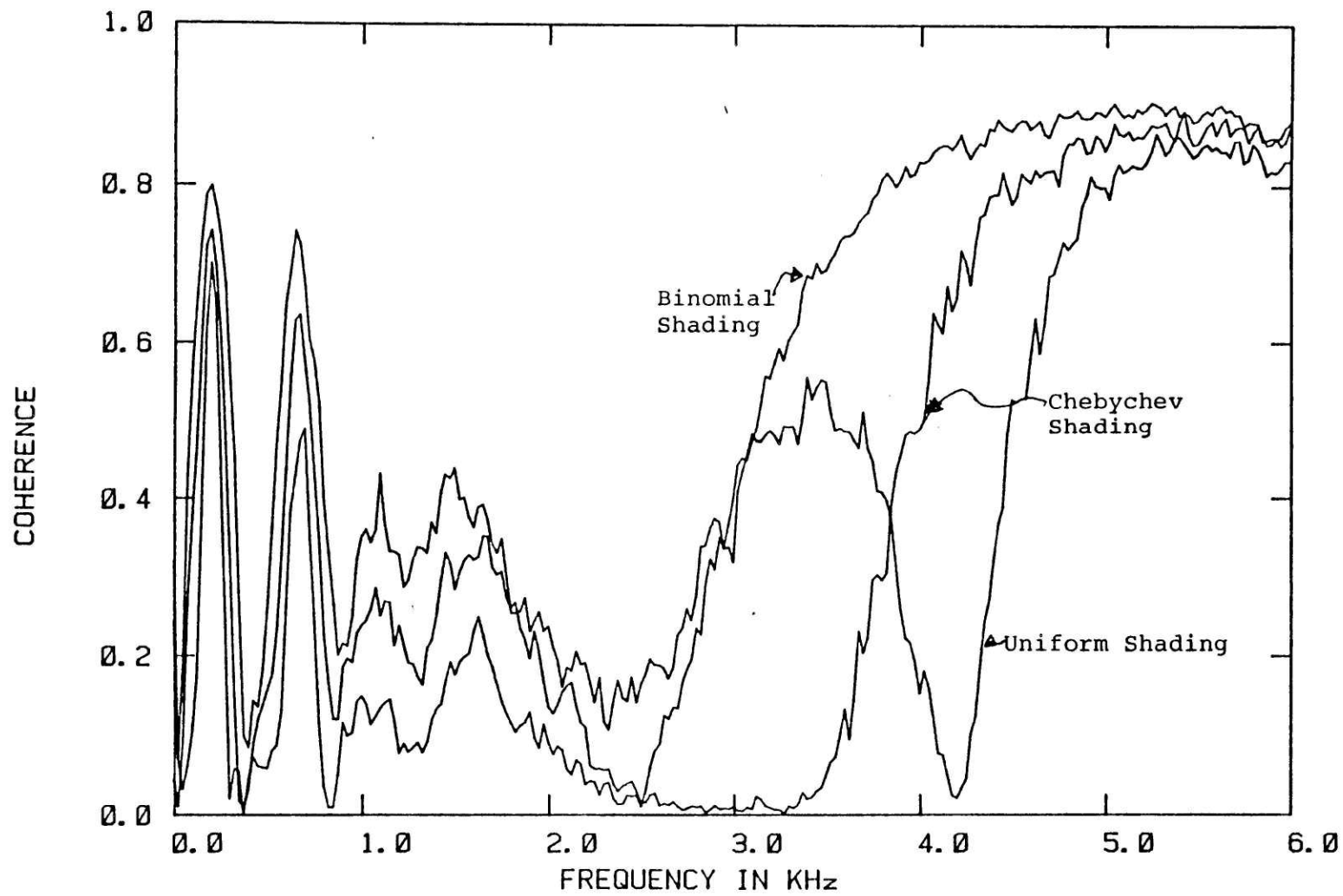
FIGURE 4.7   Comparison of Coherence for Various Shadings.
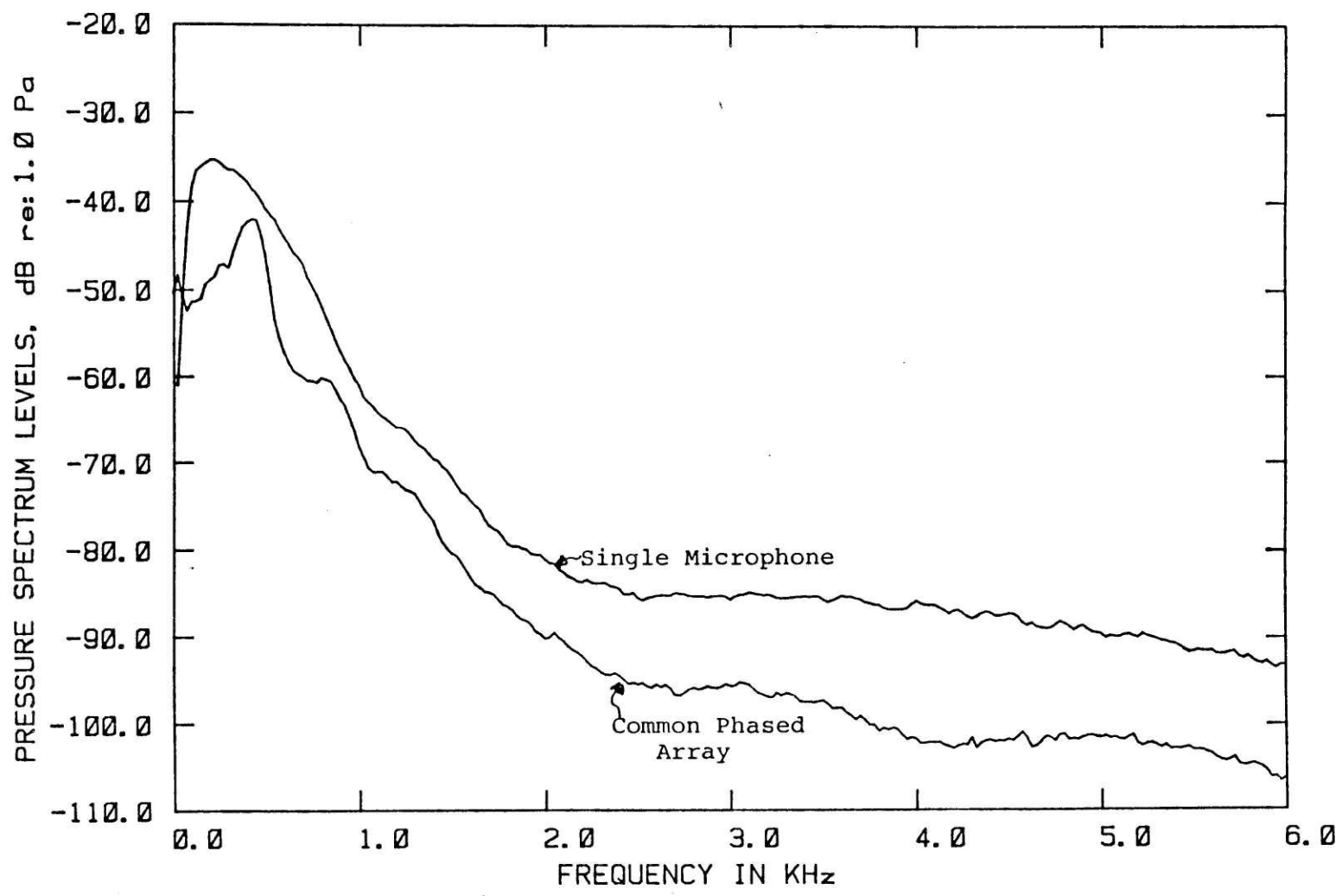
FIGURE 4.8   The Common Phased Array Response @ 15 M/S.
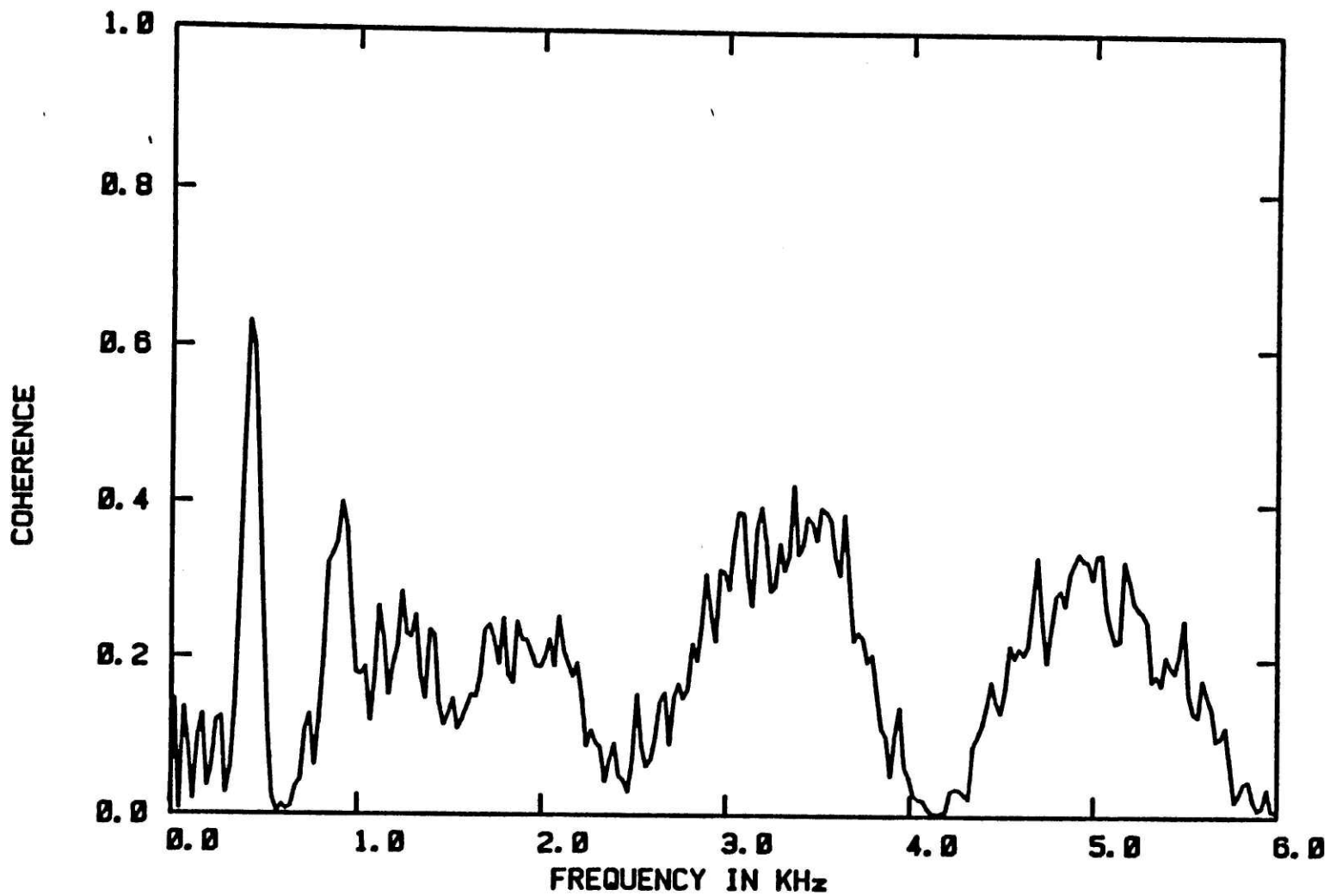
FIGURE 4.9   Coherence of Common Phased Array @ 15 M/S.
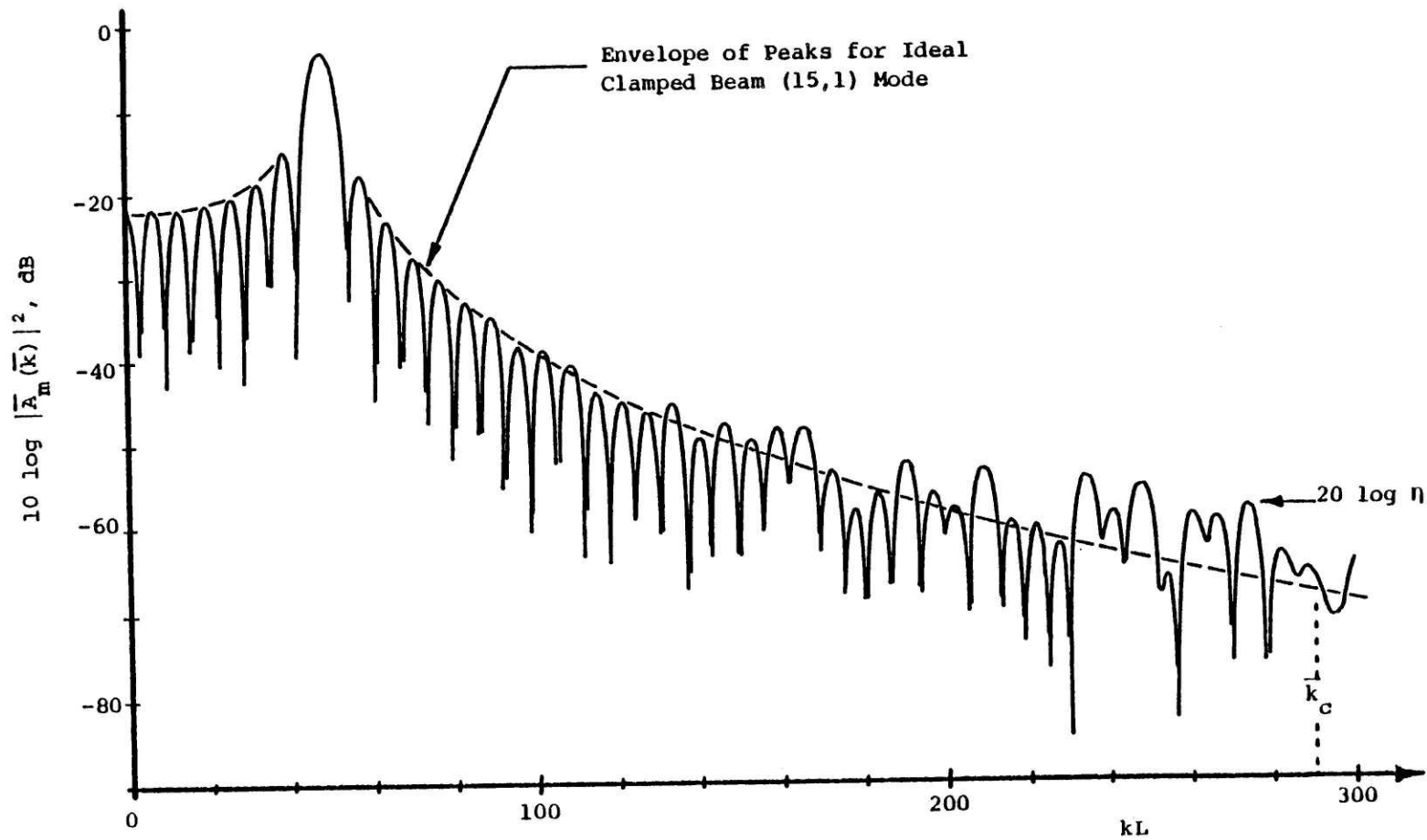
FIGURE 4.10   Measured $|A_m(\bar{k})|^2$:   (15,1) Mode of the Clamped Plate,
$\bar{k}_c$ = Typical Covective Wavenumber (U_∞ = 40 m/sec).
(By Permission from Martin)
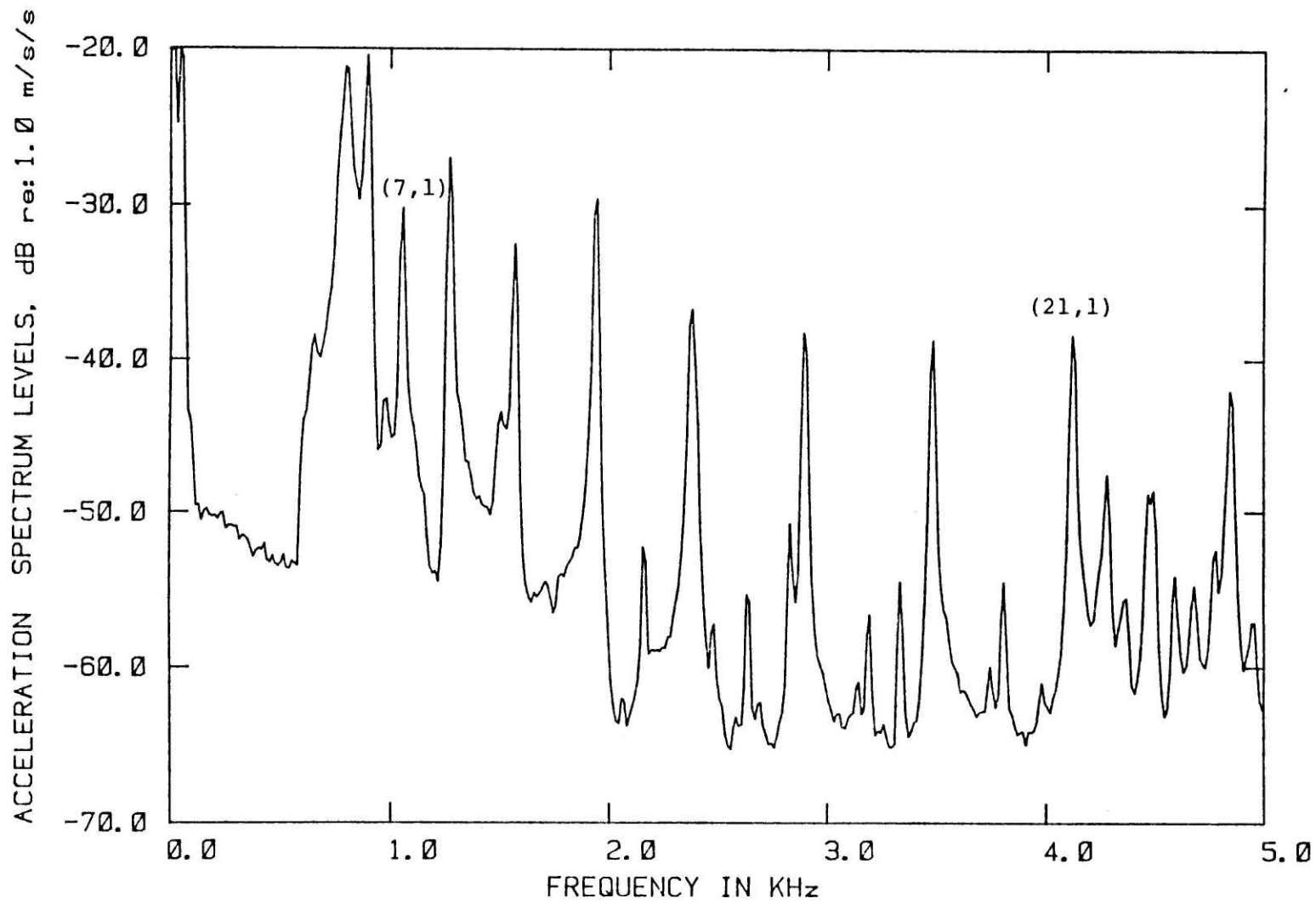
FIGURE 4.11 Measured Acceleration Spectrum of Martin Plate @ 40 M/S.
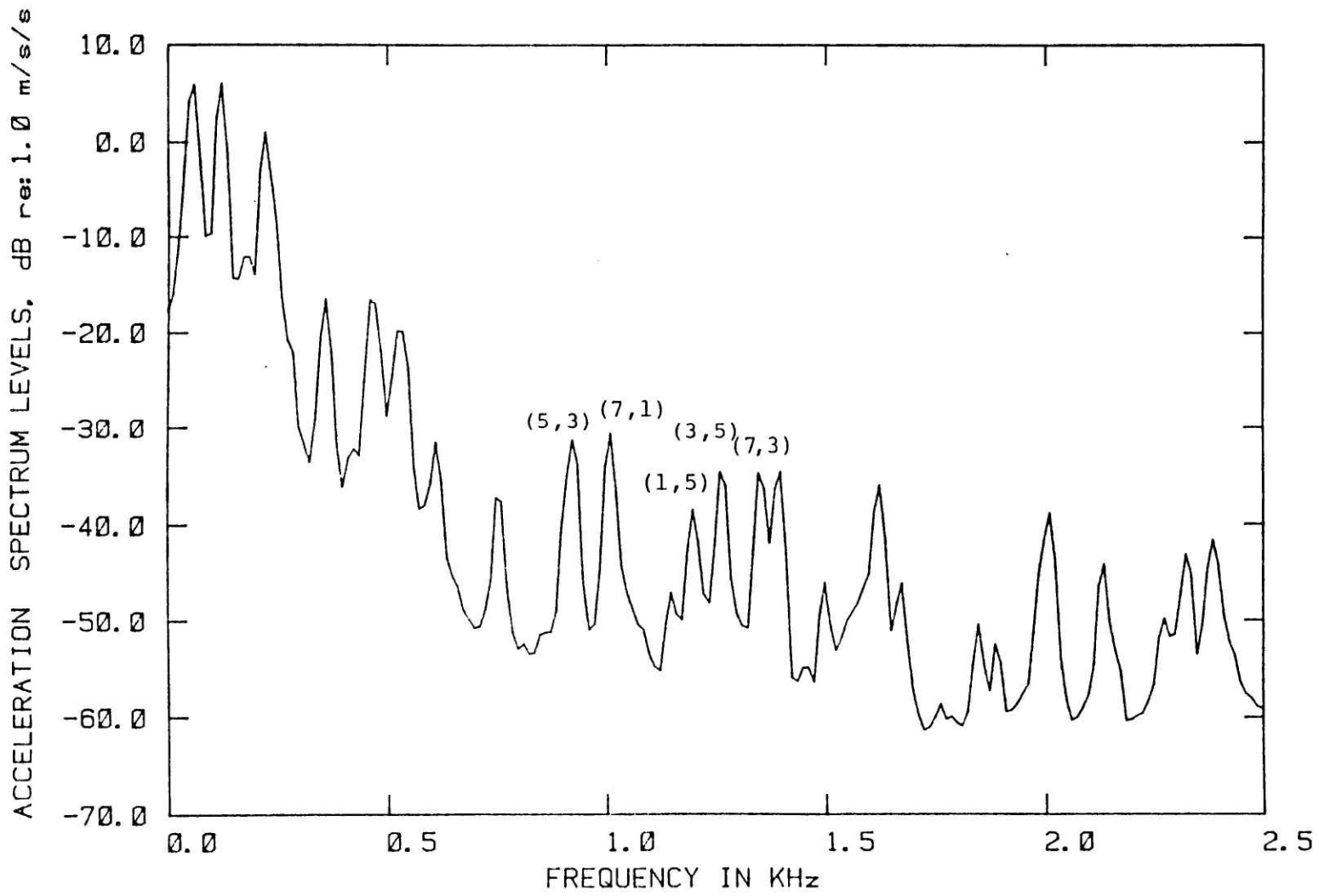
FIGURE 4.12   Measured Acceleration Spectrum of (odd,odd) Modes of
Jameson Plate @ 40 M/S.
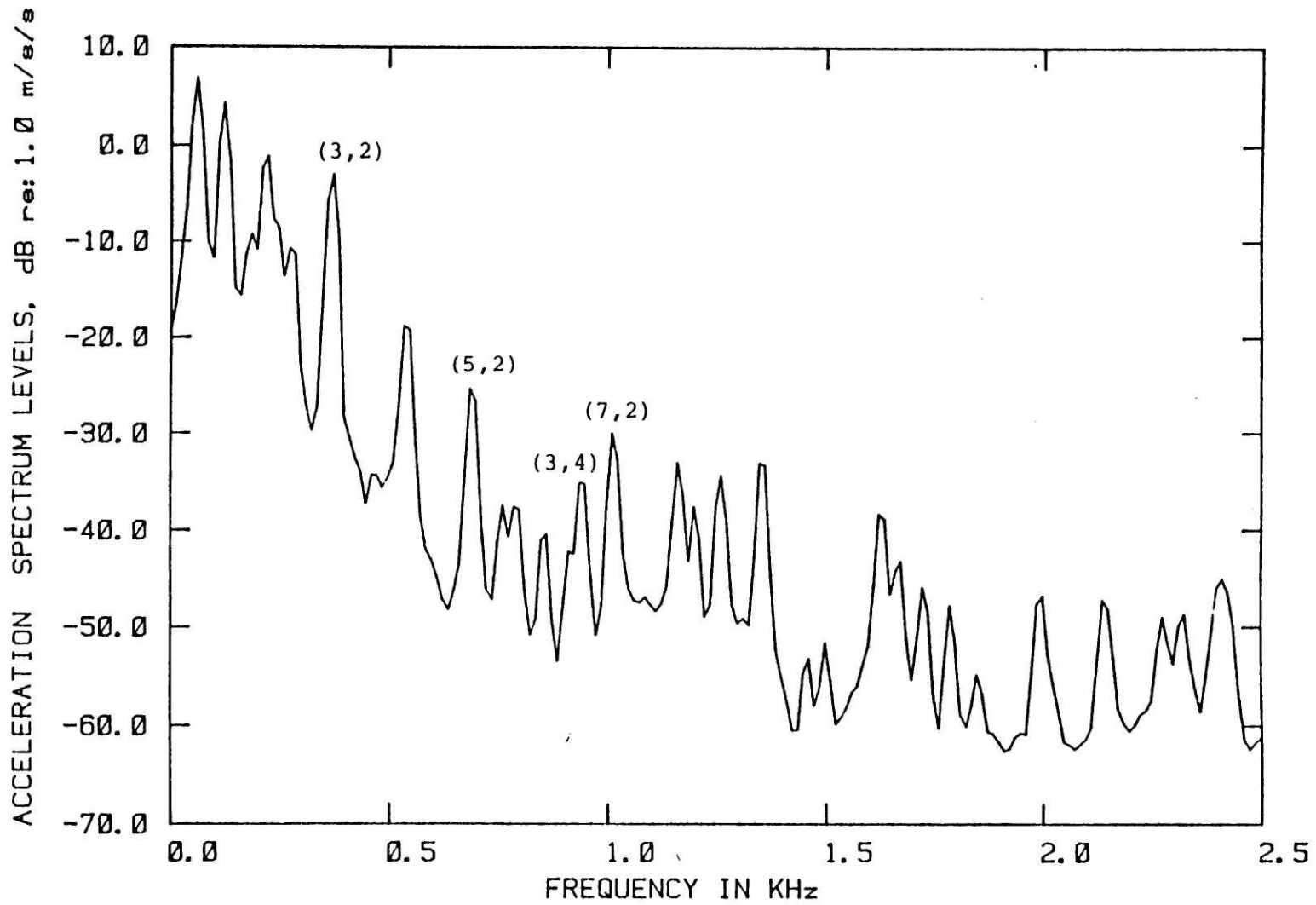
FIGURE 4.13   Measured Acceleration Spectrum of (odd,2) Modes of
Jameson Plate @ 40 M/S.
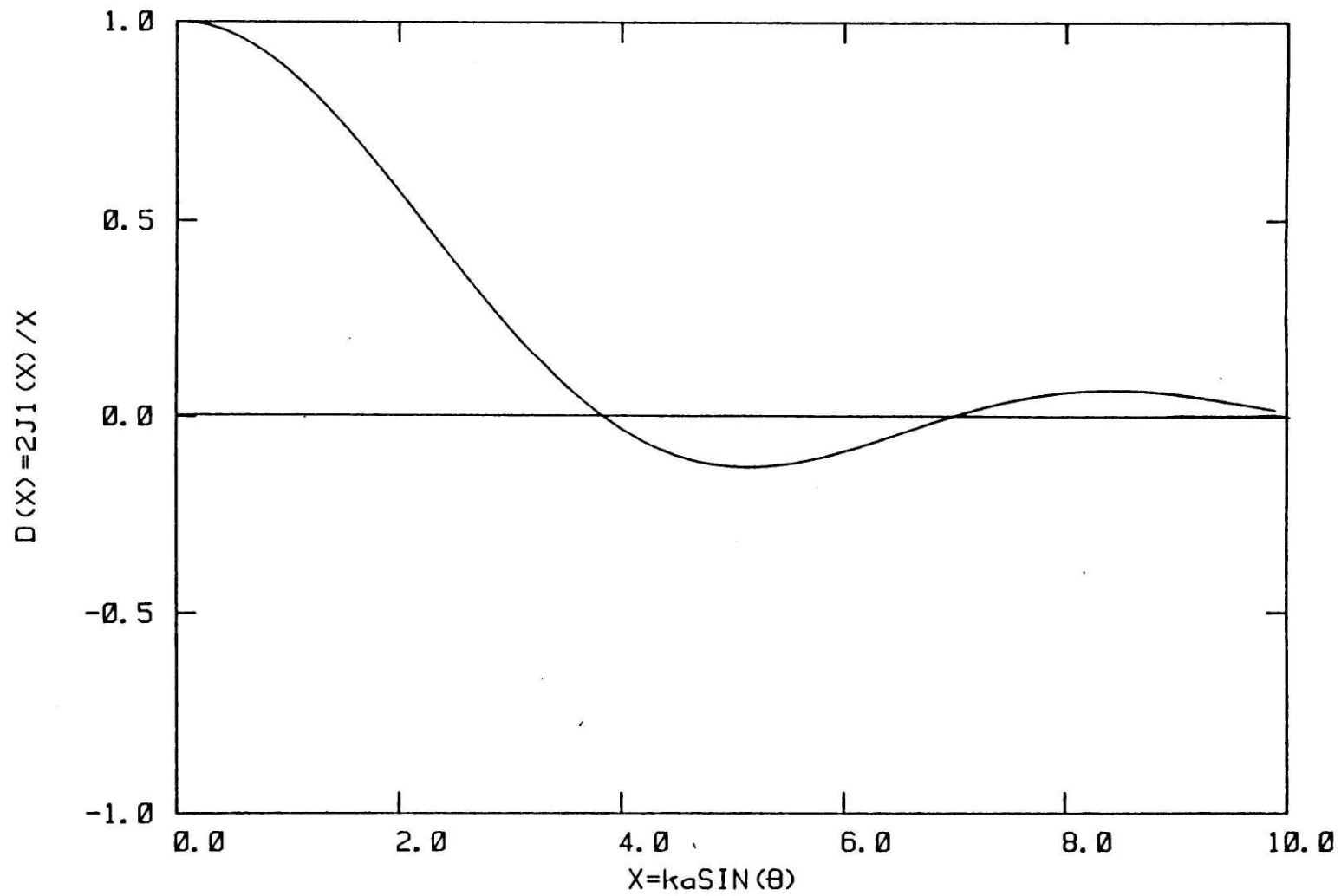
FIGURE 4.14   Directivity Pattern for Rigid Circular Piston.
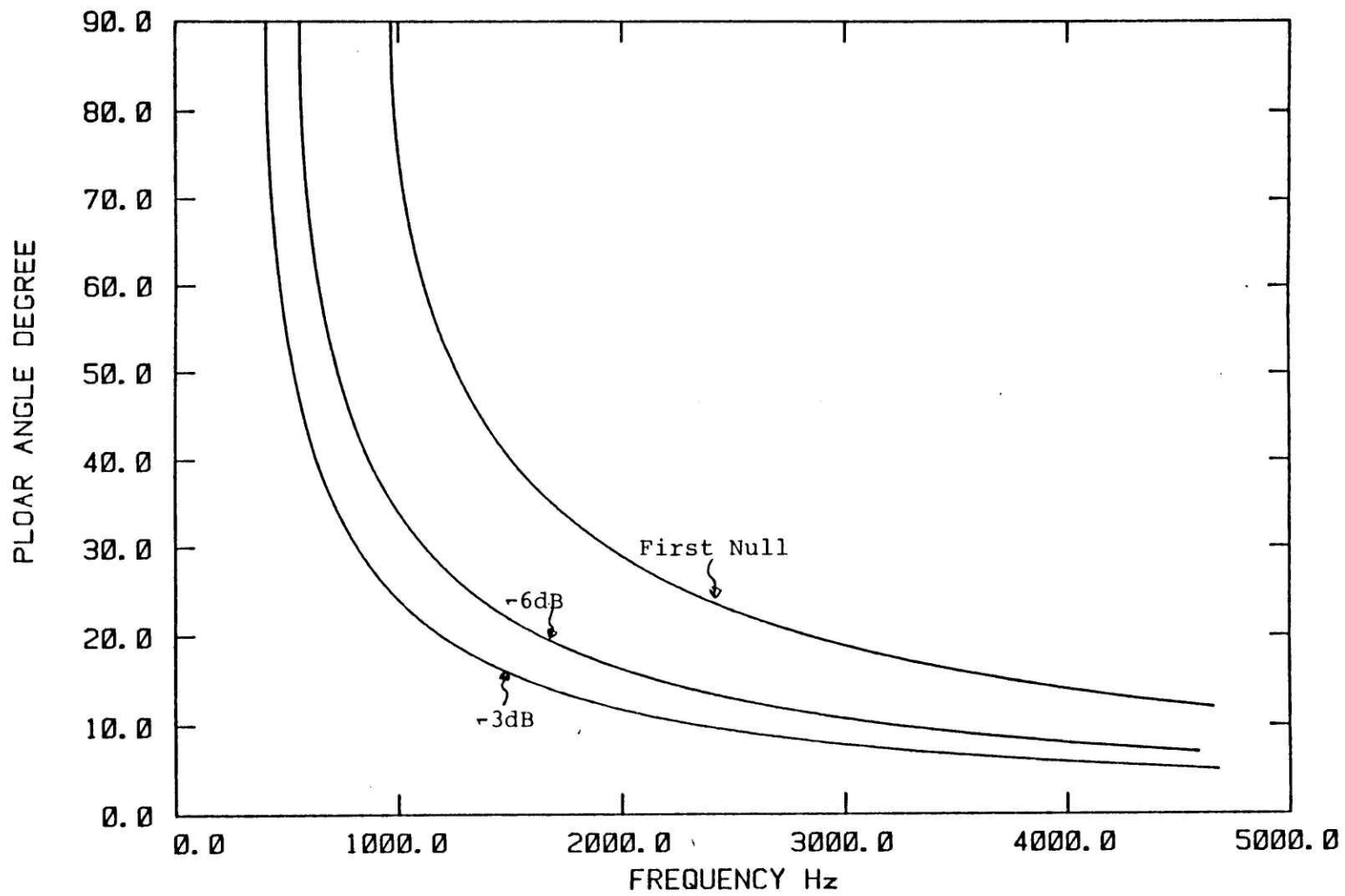
FIGURE 4.15 Directivity Beam Width @ -3dB, -6dB, and First Null.
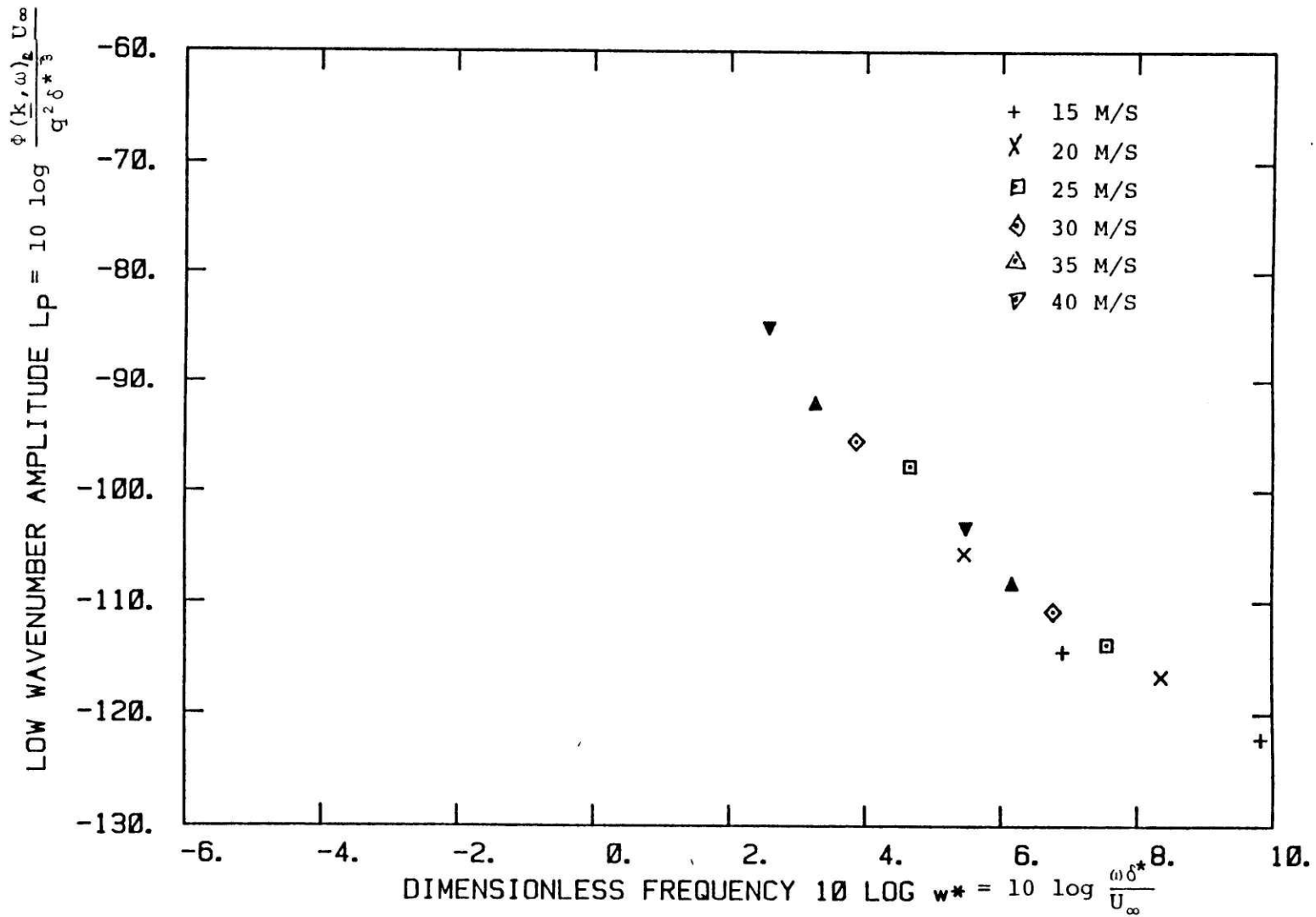
FIGURE 5.1 Low Wavenumber Results for Alternating Phase Uniform Shaded Array at Position 1.
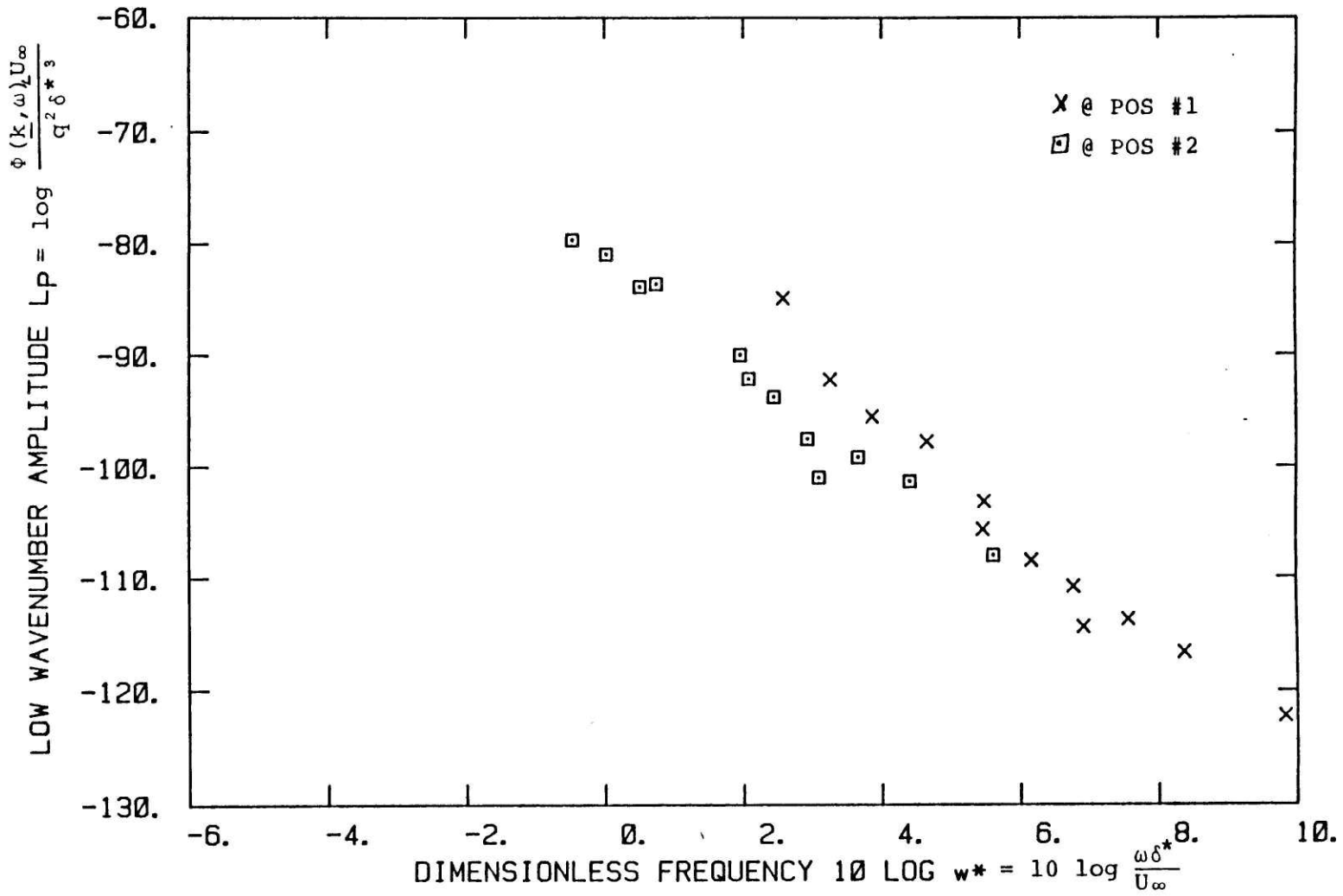
FIGURE 5.2   Comparison of Low Wavenumber Results for Alternating Phased
Uniform Shaded Array at Two Positions.

The y-axis is labeled: LOW WAVENUMBER AMPLITUDE $L_P = 10 \log \dfrac{\Phi(\underline{k},\omega) / U_\infty}{q^2 \delta^{*3}}$

The x-axis is labeled: DIMENSIONLESS FREQUENCY $10 \text{ LOG } w^* = \log \dfrac{\omega \delta^*}{U_\infty}$

Legend:
X Uniform
□ Chebychev
▲ Binomial
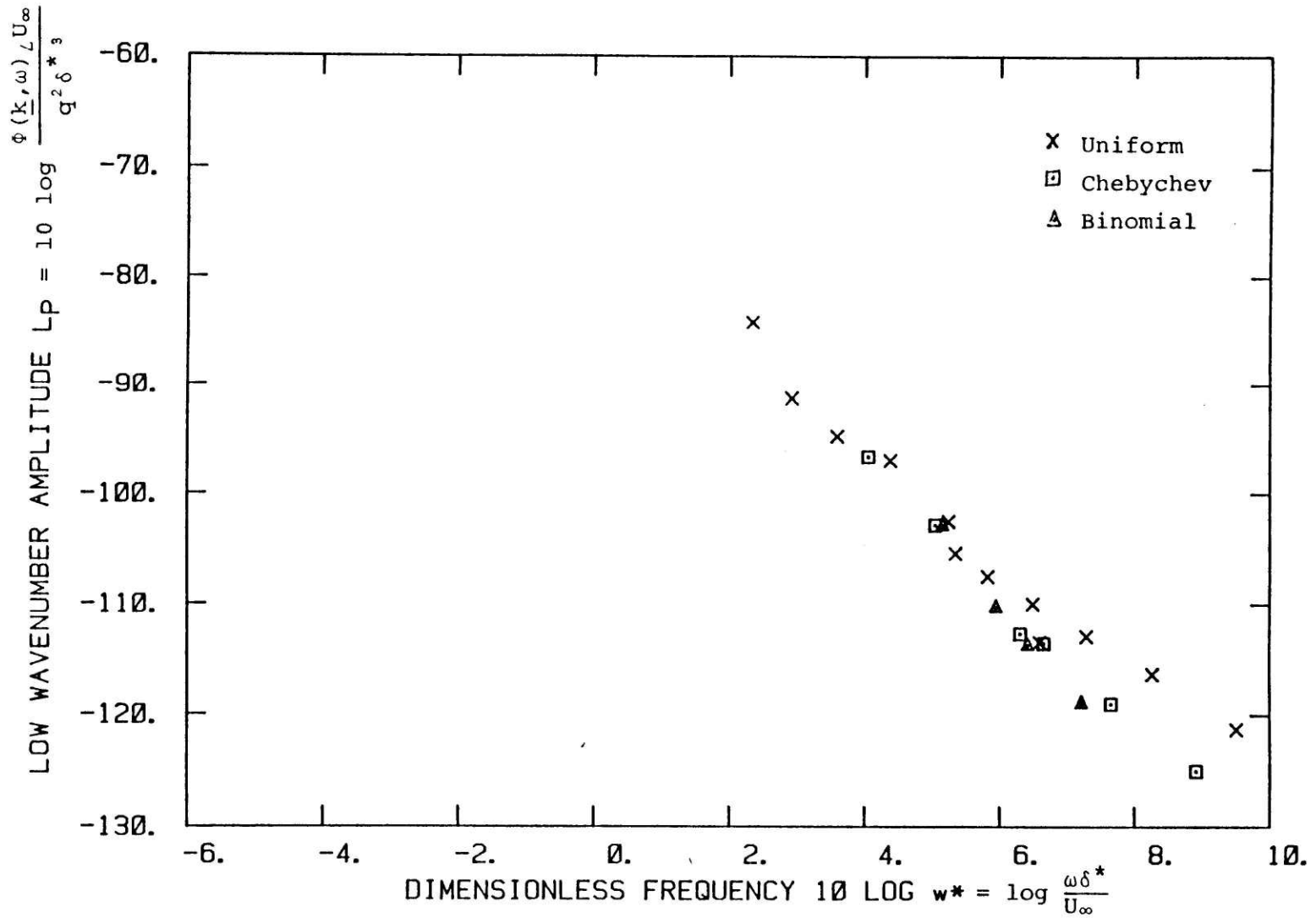
FIGURE 5.3 Comparison of Low Wavenumber Results for Uniform, Chebychev, Binomial Shading of Alternating Phase Array.
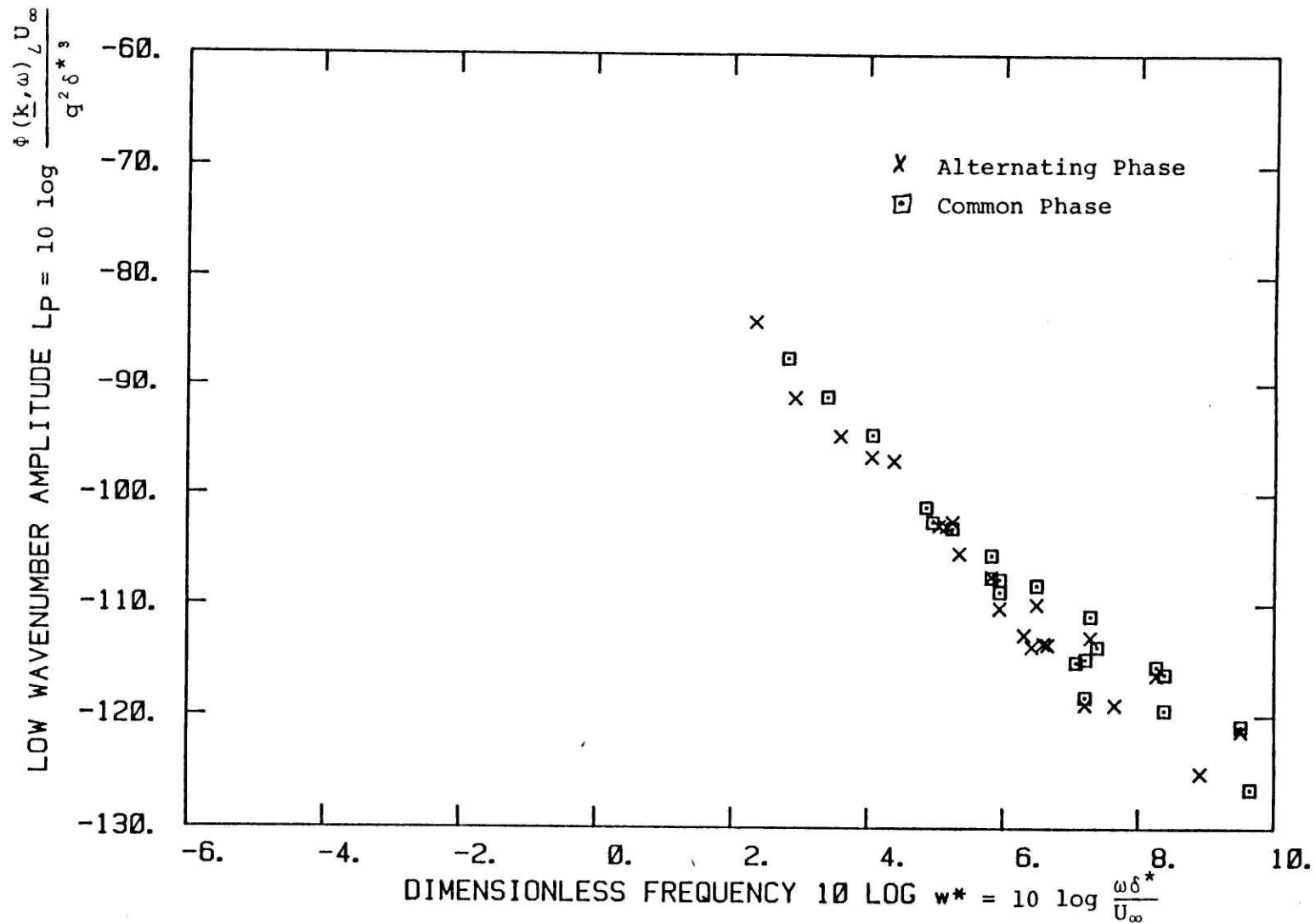
FIGURE 5.4   Comparison of Low Wavenumber Results for Alternating and
Common Phased Array (all shadings).
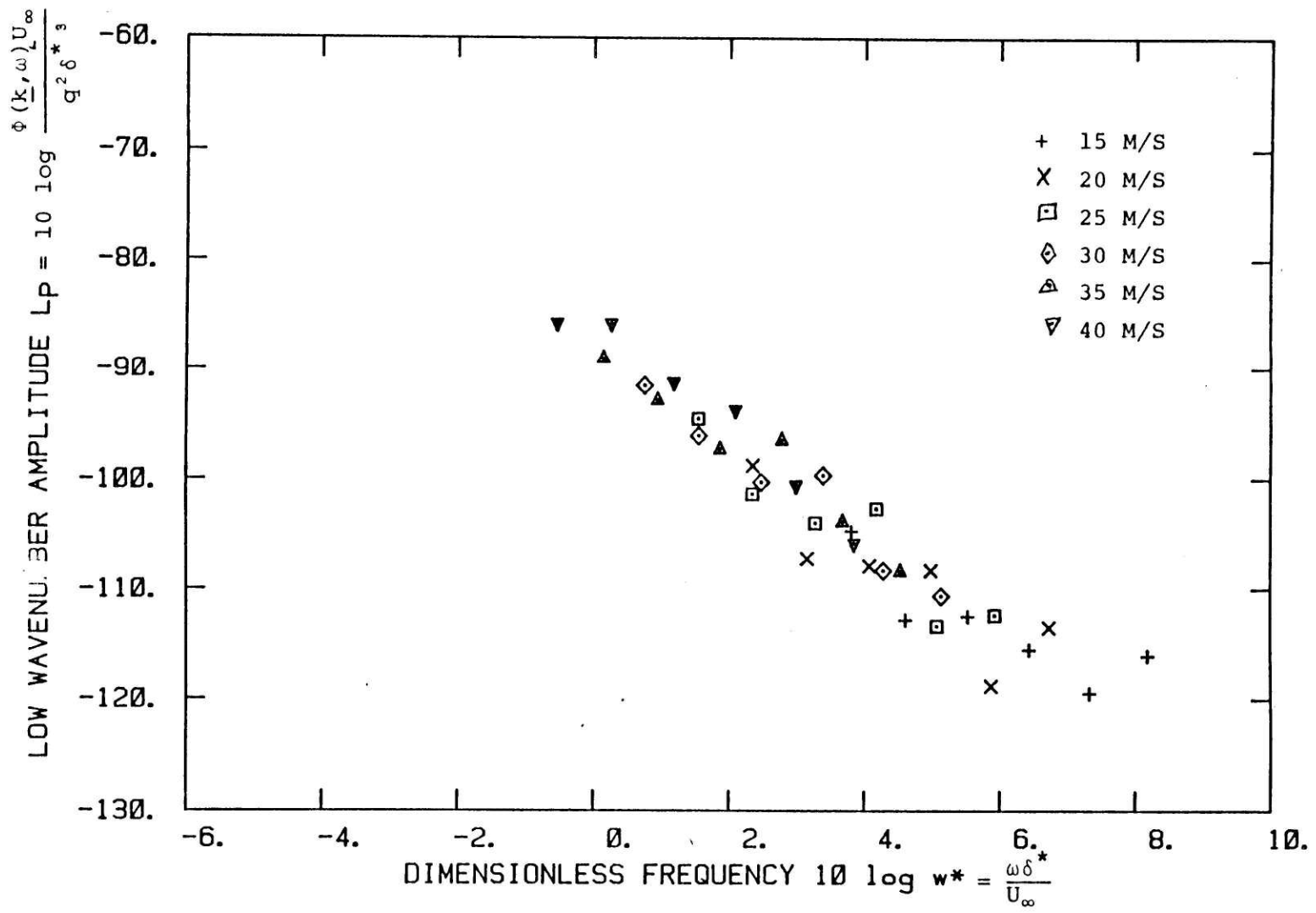
FIGURE 5.5 Low Wavenumber Results for Martin Plate @ Position #1.
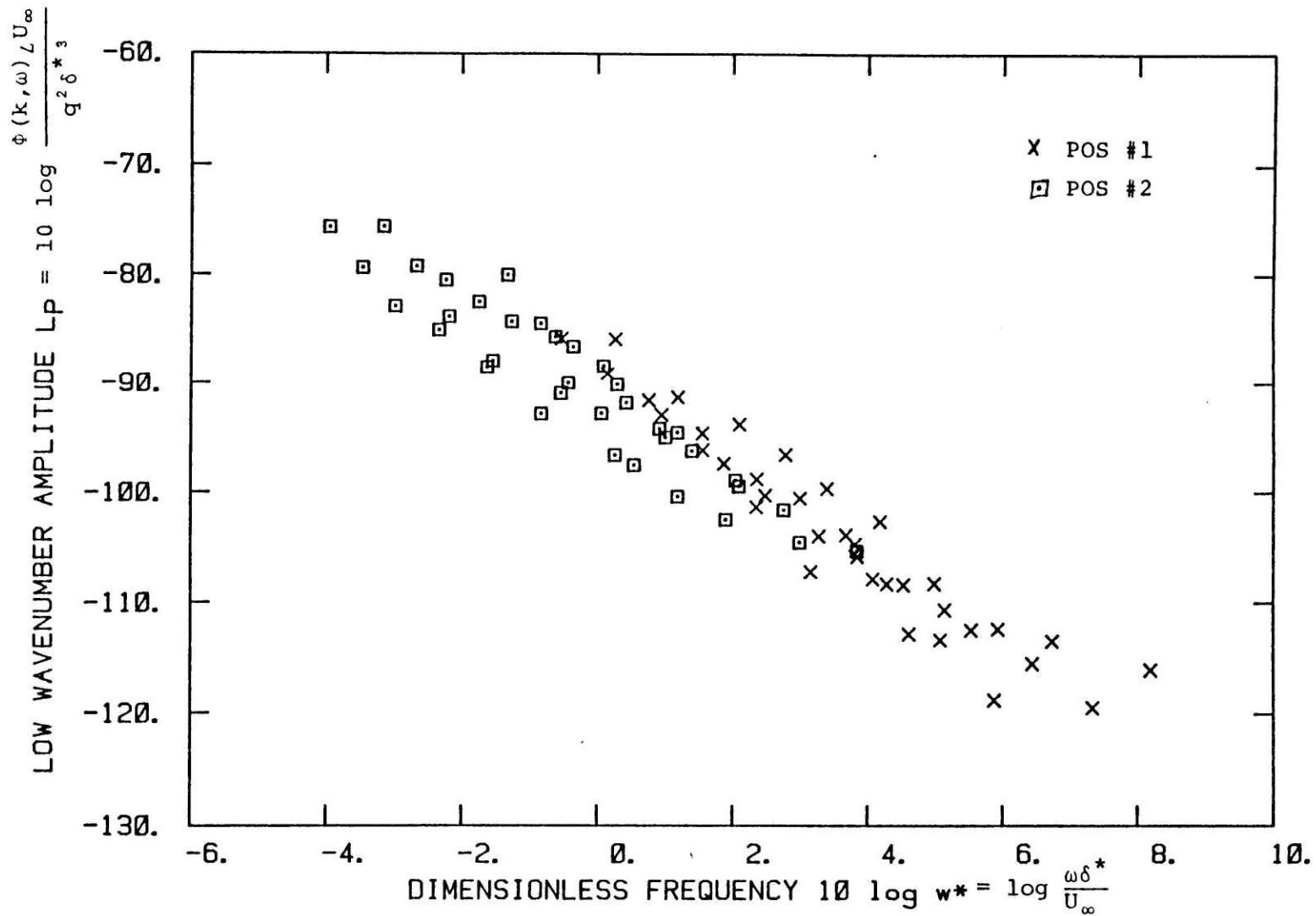
FIGURE 5.6   Comparison of Low Wavenumber Results for Martin Plate at
Two Different Locations.
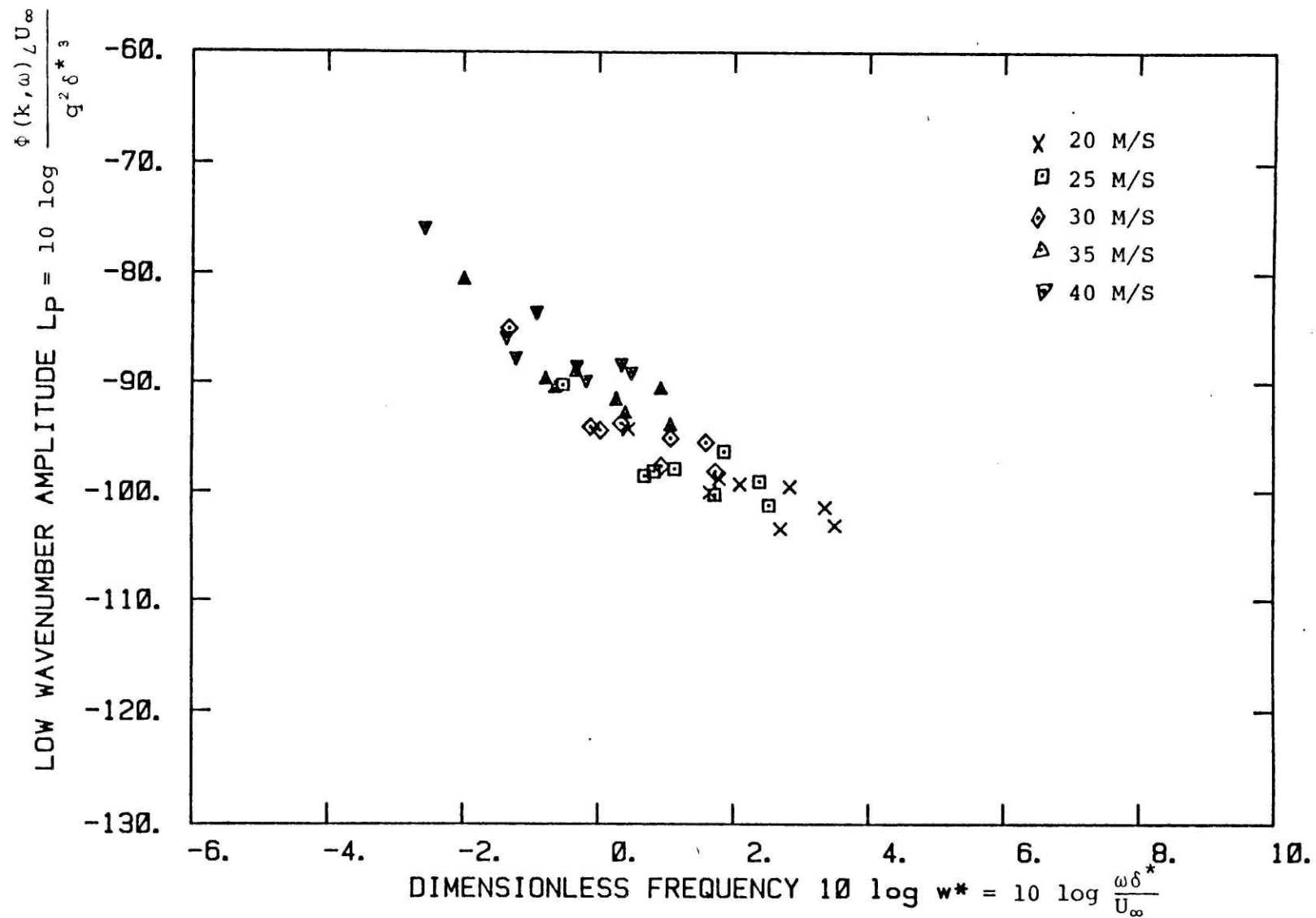
FIGURE 5.7   Low Wavenumber Results for Jameson Plate @ Position #1.
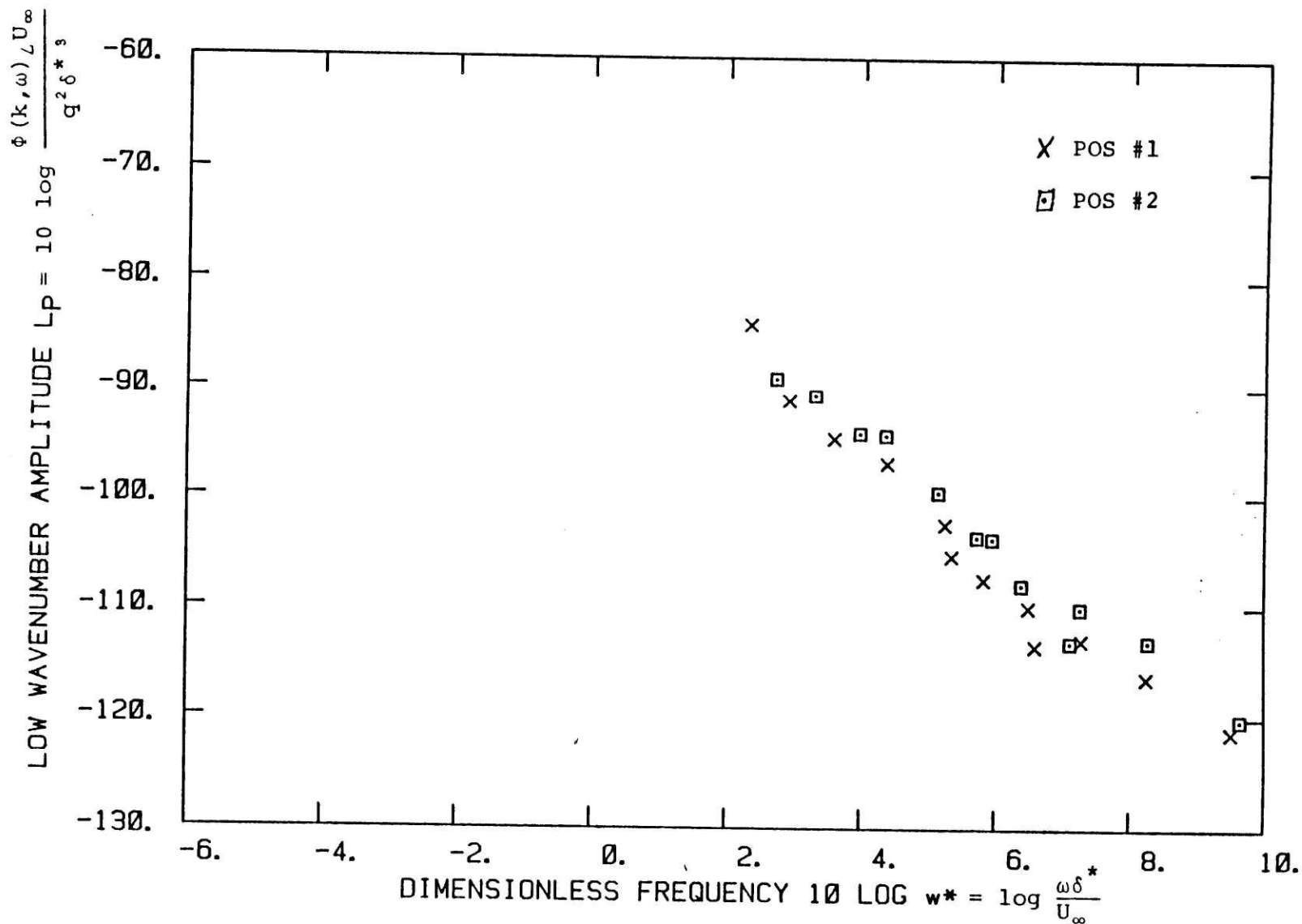
FIGURE 5.8 Comparison of Alternating Array Low Wavenumber Results
@ Two Position for $\delta^* = $ constant $= 0.2$ inches.
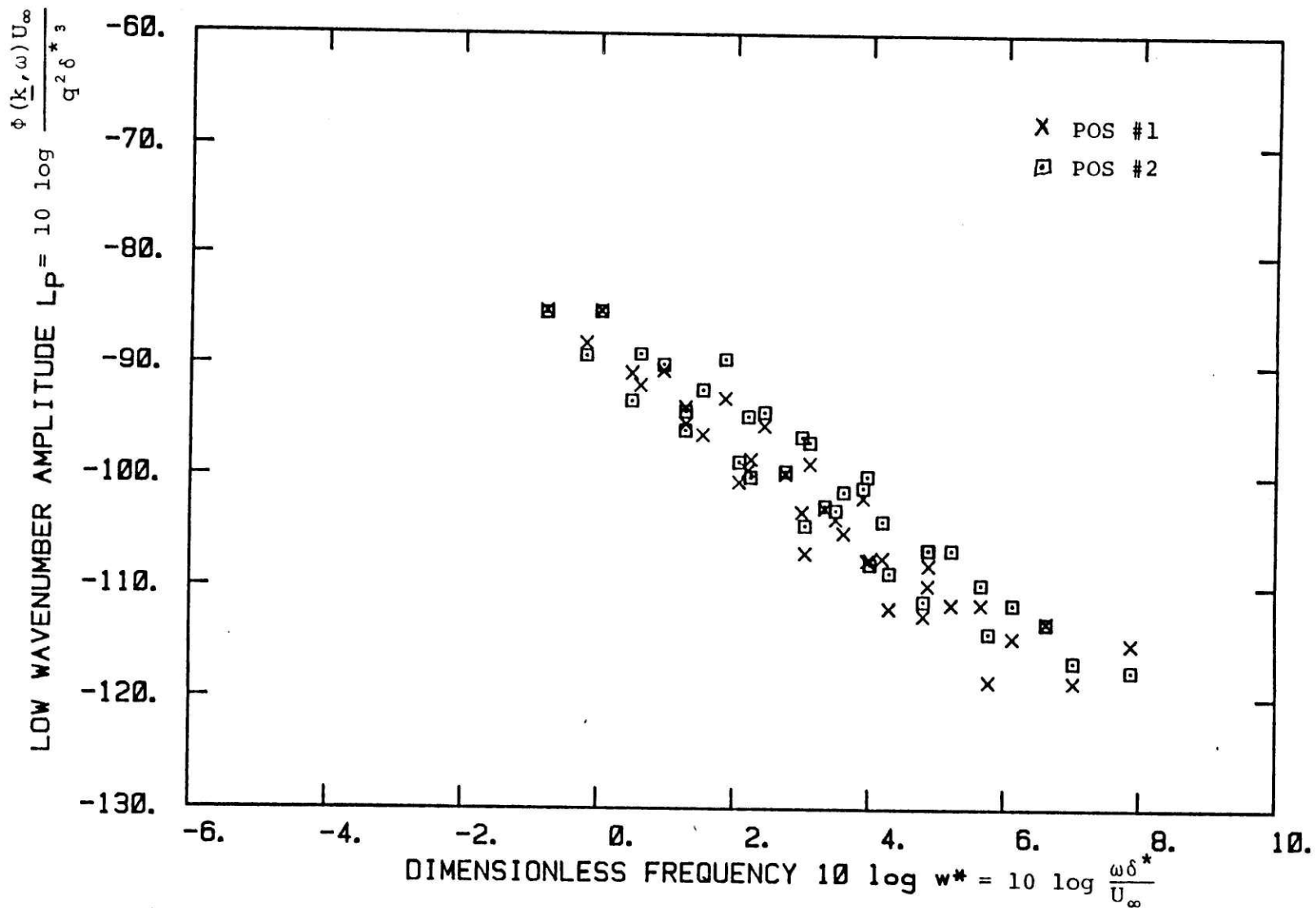
FIGURE 5.9   Comparison of Martin Plate Low Wavenumber Results at Two
Position With $\delta^* = $ constant $ = 0.2$ Inches.
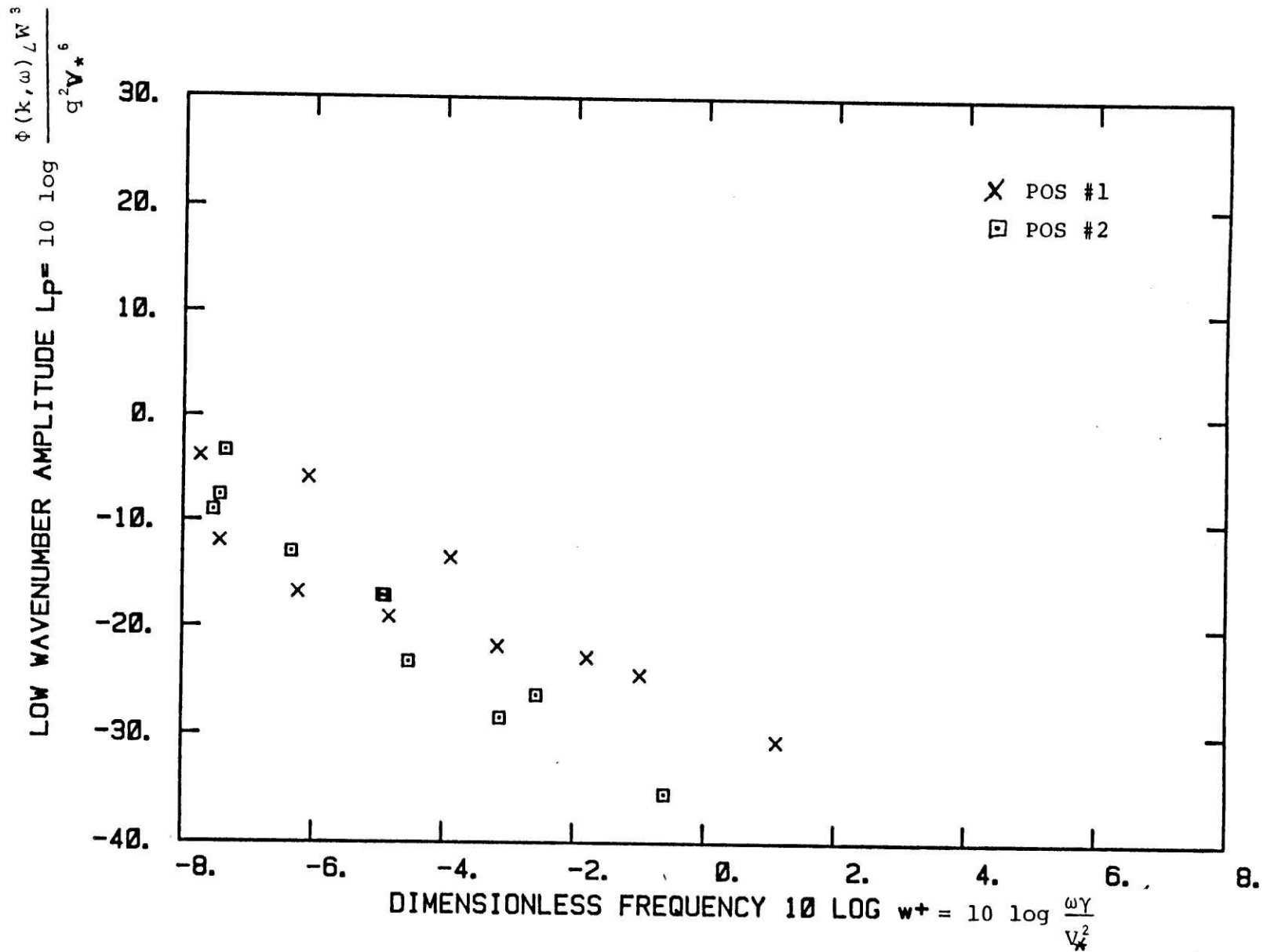
FIGURE 5.10   Alternating Phased Array Low Wavenumber Results at Two
Location Non-Dimensionalized on Inner Variables
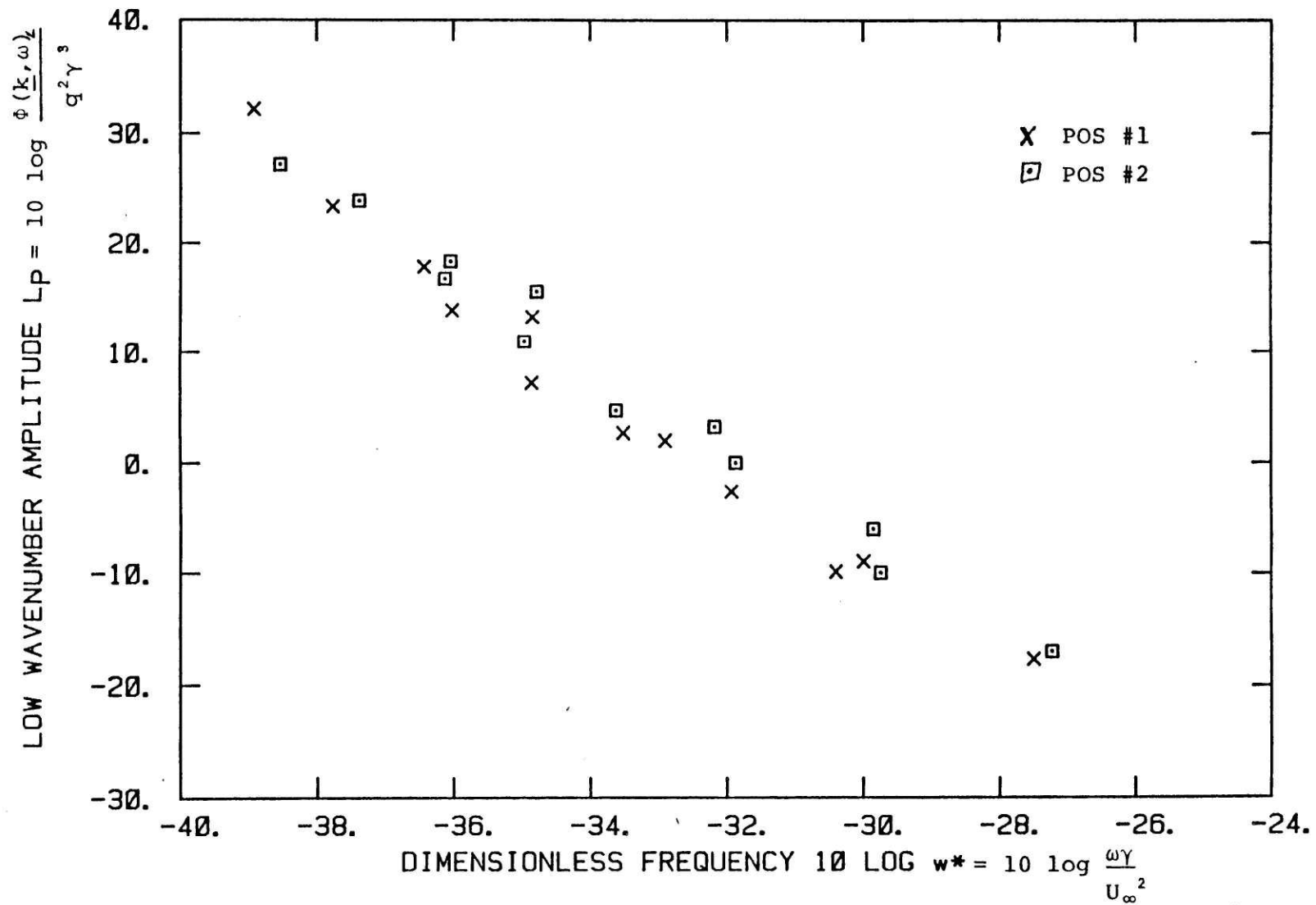
FIGURE 5.11   Alternating Phase Array Low Wavenumber Results at Two
Locations Non-Dimensionalized on Flow Variables
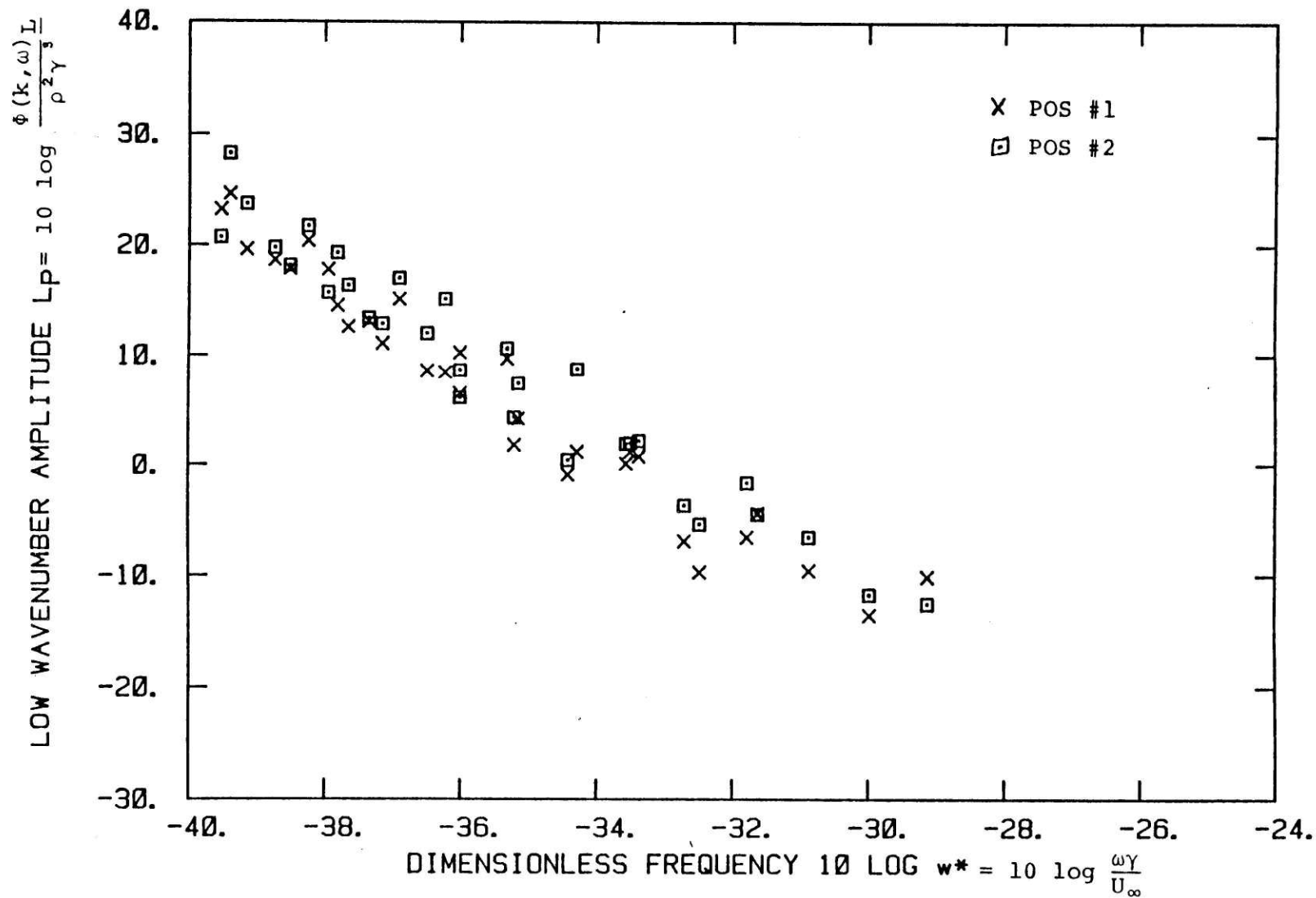
FIGURE 5.12   Martin Plate Low Wavenumber Results at Two Locations
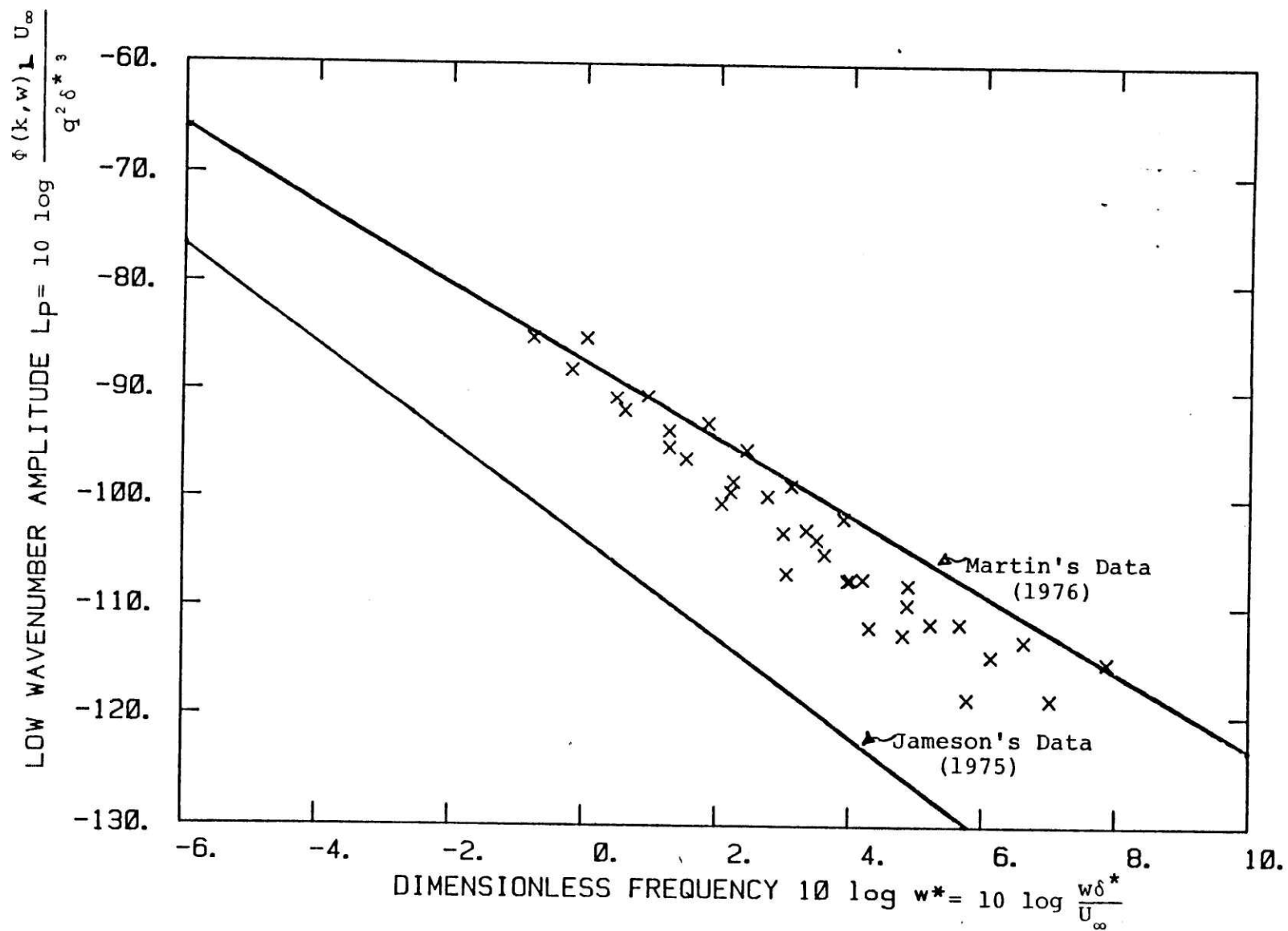Non-Dimensionalized on Flow Variables.

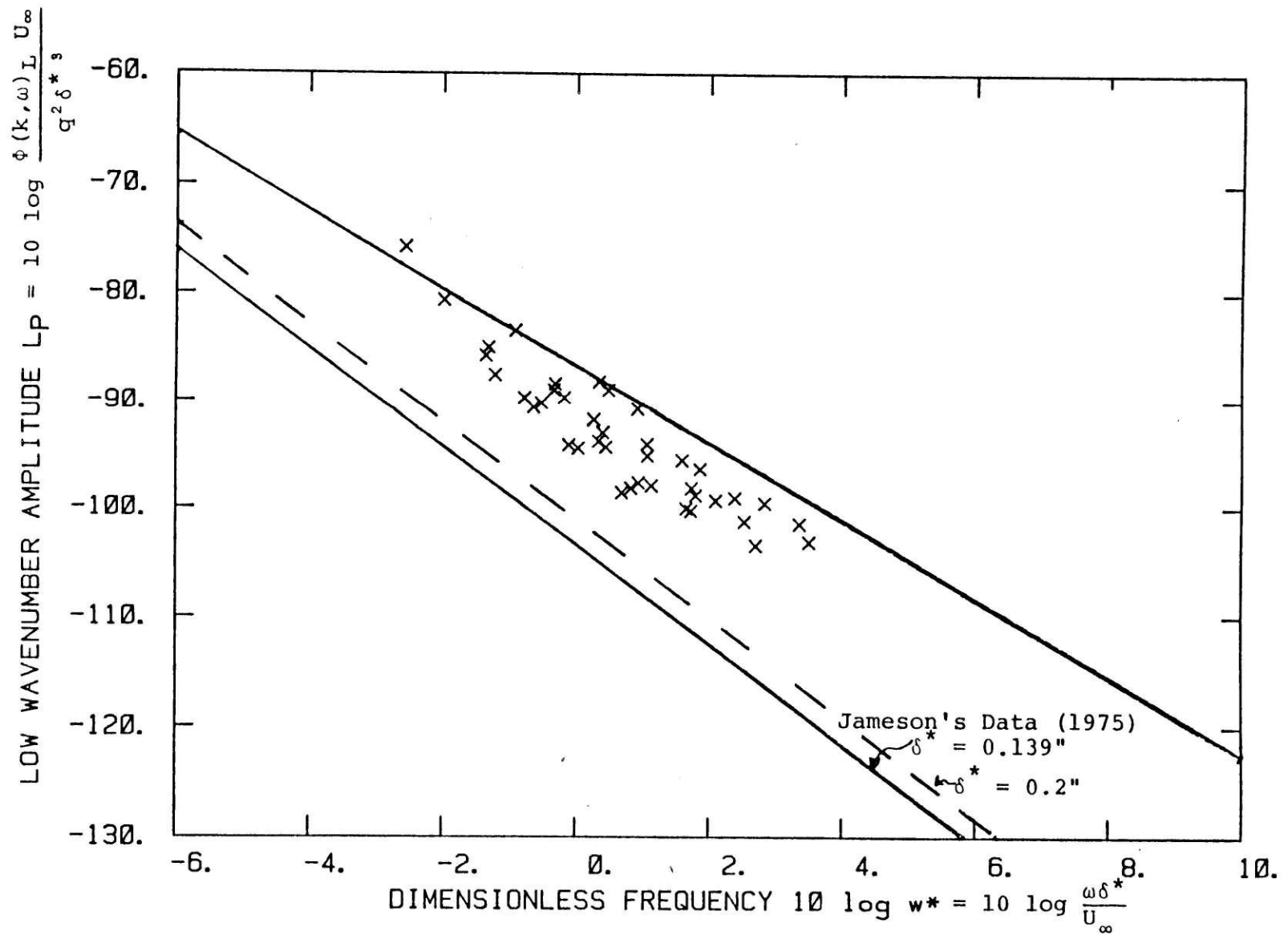FIGURE 5.13   Martin Plate Low Wavenumber Results Compared to Earlier Investigators.

FIGURE 5.14   Jameson Plate Low Wavenumber Results Compared With Earlier
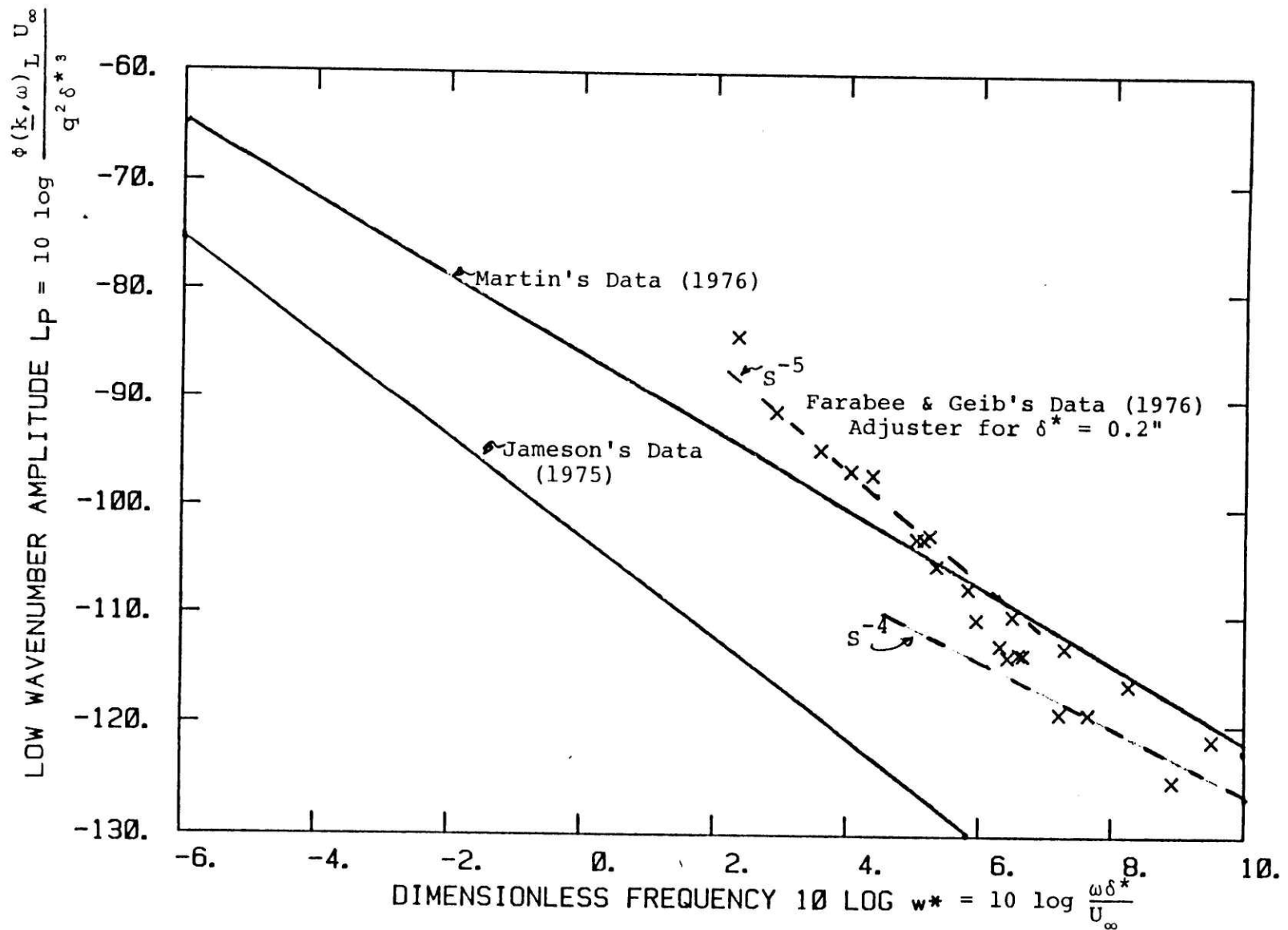Investigators.

FIGURE 5.15   Microphone Array Low Wavenumber Results Compared to
Earlier Investigators.